MEASUREMENT OF m_{top} VIA NEUTRINO WEIGHTING IN THE DILEPTON DECAY CHANNELS AT DØ

by

Jeffrey Willard Temple

A Dissertation Submitted to the Faculty of the

DEPARTMENT OF PHYSICS

In Partial Fulfillment of the Requirements
For the Degree of

DOCTOR OF PHILOSOPHY

In the Graduate College

THE UNIVERSITY OF ARIZONA

2006

THE UNIVERSITY OF ARIZONA
GRADUATE COLLEGE

As members of the Dissertation Committee, we certify that we have read the dissertation prepared by Jeffrey Willard Temple entitled "Measurement of m_{top} via Neutrino Weighting in the Dilepton Decay Channels at DØ" and recommend that it be accepted as fulfilling the dissertation requirement for the Degree of Doctor of Philosophy.

_____ Date: 11/10/06
Kenneth Johns

_____ Date: 11/10/06
Elliott Cheu

_____ Date: 11/10/06
Keith Dienes

_____ Date: 11/10/06
Ingrid Novodvorsky

_____ Date: 11/10/06
Ina Sarcevic

Final approval and acceptance of this dissertation is contingent upon the candidate's submission of the final copies of the dissertation to the Graduate College.

I hereby certify that I have read this dissertation prepared under my direction and recommend that it be accepted as fulfilling the dissertation requirement.

_____ Date: 11/10/06
Dissertation Director: Kenneth Johns

STATEMENT BY AUTHOR

This dissertation has been submitted in partial fulfillment of requirements for an advanced degree at The University of Arizona and is deposited in the University Library to be made available to borrowers under rules of the Library.

Brief quotations from this dissertation are allowable without special permission, provided that accurate acknowledgment of source is made. Requests for permission for extended quotation from or reproduction of this manuscript in whole or in part may be granted by the head of the major department or the Dean of the Graduate College when in his or her judgment the proposed use of the material is in the interests of scholarship. In all other instances, however, permission must be obtained from the author.

SIGNED: _____

Jeffrey Willard Temple

ACKNOWLEDGMENTS

First, I'd like to thank Ken Johns, who lured me to Fermilab with the words, "C'mon, you'll only need to be out there for a year," but was otherwise a helpful and extremely supportive advisor. Erich Varnes provided me with invaluable insights into the mechanisms of the neutrino weighting analysis, and deserves a much better football team than the Cleveland Browns.

I am indebted to Rob McCroskey for his efforts in training me in the Level 1 Muon system, his constant support and acceptance of panicked phone calls from the control room, and his insistence on weekly Portillo's visits. Rob set a ridiculously high standard for all the experts who followed him, and someday I'll get him back for that.

Thanks also go out to John Butler, Jason Kasper, Chris Leeman, Stefan Anderson, Joel Steinberg, and all those who helped build Level 1 Muon into its current robust state. The Arizona group at DØ – Pete Johnson, Noah Wallace, Pete Tamburello, and Jessica Levêque – always provided an entertaining work environment.

Level 1 Muon also benefited from the help of a multitude of experts from other subsystems. In particular, Dmitri Denisov, Tom Diehl, Markus Wobisch, Stefan Grünendahl, and Al Ito were always there to provide us with any support and assistance that we needed. Run coordinators Bill Lee and Taka Yasuda always responded without complaint to our requests for accesses and special runs. The electrical support group, including John Anderson, John Fogelsong, and Mike Cherry, worked above and beyond the call of duty in helping us to redesign and rebuild our power supplies. To Susan Burke, with whom I collaborated, commiserated, and shared countless controlled accesses, and who saved any number of the people mentioned above from grievous bodily harm, I want to say one word to you, just one word: "Jute."

My friends outside DØ, including Adam, Ashwin, Jason, Odysseas, Shilpa, Mark, Elizabeth, Dana, and Michelle, reminded me that there is a world beyond the laboratory. From what I hear of it, it seems scary. Finally, I'd like to thank my parents, who can finally stop asking me, "When are you going to graduate?" and go back to asking me, "When are you going to settle down, get married, and start giving us grandchildren?"

To everyone I've ever known in my whole life.
Except my little brother, Andy.

TABLE OF CONTENTS

LIST OF FIGURES **9**

LIST OF TABLES **13**

ABSTRACT **14**

CHAPTER 1. INTRODUCTION **15**

CHAPTER 2. THEORY **18**
- 2.1. The Standard Model 18
  - 2.1.1. Quantum Chromodynamics 19
  - 2.1.2. Electroweak Unification 20
- 2.2. Top Quark Production 22
- 2.3. Measurement of the Mass of the Top Quark 24
- 2.4. A Note on the Top Quark Mass 26

CHAPTER 3. EXPERIMENTAL APPARATUS **28**
- 3.1. Fermilab Accelerators 28
- 3.2. The DØ Detector 31
  - 3.2.1. Tracking 32
  - 3.2.2. Calorimeter 35
  - 3.2.3. Preshower Detectors 37
  - 3.2.4. Muon Detector 38
- 3.3. Triggering at DØ 41
- 3.4. Luminosity 42
- 3.5. Detector Operation 43

CHAPTER 4. EVENT RECONSTRUCTION **44**
- 4.1. Event Simulation 44
- 4.2. Event Reconstruction 45
  - 4.2.1. Central Tracks 46
  - 4.2.2. Primary Vertex 47
  - 4.2.3. Calorimeter Objects 48
  - 4.2.4. Muon Reconstruction 51
  - 4.2.5. Missing Transverse Energy 53
- 4.3. Resolutions and Monte Carlo Corrections 53

TABLE OF CONTENTS—*Continued*

CHAPTER 5. EVENT SELECTION **56**
5.1. Triggering on Dileptons 56
5.2. Common Event Selection Criteria 58
5.3. Channel-Dependent Selection Criteria 59
5.3.1. Dimuon Events 59
5.3.2. Dielectron Events 60
5.3.3. Electron-muon Events 62
5.4. Event Yields 63
5.4.1. Z/γ Decays 64
5.4.2. WW and WZ Decays 64
5.4.3. QCD Fakes 65

CHAPTER 6. MASS TEMPLATE GENERATION **69**
6.1. Neutrino Weighting 69
6.2. Monte Carlo Tests 72
6.2.1. Parton-level Tests 72
6.2.2. Reconstructed Particle Tests 73
6.3. Template Generation 74
6.3.1. Background Templates 75
6.3.2. Null Weight Vectors 75

CHAPTER 7. LIKELIHOOD FIT **90**
7.1. Principles of Likelihood Fits 90
7.2. Functional Form of the Likelihood 91
7.3. Optimization of the Likelihood Fit 94
7.3.1. Fit Functions 96
7.3.2. Fit Range 99
7.3.3. h Parameter 100

CHAPTER 8. RESULTS **107**
8.1. Likelihood Fit to Data 107
8.2. Systematic Uncertainties 109
8.2.1. Jet Energy Scale 109
8.2.2. Jet and Lepton Resolution 110
8.2.3. $t\bar{t}$ + Jet Events 111
8.2.4. Event Parton Distribution Functions 112
8.2.5. Template Statistics 113
8.2.6. Background Shape 113
8.2.7. Dielectron Trigger Efficiency 114
8.3. Final Result of Mass Measurement 115

TABLE OF CONTENTS—*Continued*

CHAPTER 9. CONCLUSION **120**

APPENDIX A. LEPTON TRIGGERS USED IN THE ANALYSIS **125**
A.1. Muon Triggers 125
A.2. Electron Triggers 126

APPENDIX B. ALGEBRAIC SOLUTION FOR NEUTRINO RAPIDITY **130**

APPENDIX C. LEVEL 1 MUON MONITORING TOOLS **134**
C.1. Overview of the Level 1 Muon Trigger 134
C.2. Level 1 Muon Monitoring 134
C.2.1. Real-Time Monitoring Tools 135
C.2.2. Long-Term Monitoring Tools 139
C.2.3. Diagnostic/Control Tools 159
C.3. Data Quality 163

REFERENCES **166**

LIST OF FIGURES

FIGURE 1.1. Owl shift (midnight - 8 AM) at the DØ particle physics laboratory. Note the lack of food, comfort, and sex. 15

FIGURE 2.1. Fundamental particles within the Standard Model. 19
FIGURE 2.2. Contributions to electron-electron scattering from selected (a) leading-order, (b) next-to-leading-order (NLO), and (c) next-to-next-to-leading order (NNLO) processes. Each vertex contributes a factor of $\sqrt{\alpha}$ to the scattering amplitude. 19
FIGURE 2.3. Higgs mass sensitivity to energy scale Λ. 22
FIGURE 2.4. Leading-order $t\bar{t}$ QCD production processes. 23
FIGURE 2.5. Dominant decay mode of the top quark 24
FIGURE 2.6. Dependence on the $t\bar{t}$ production cross section on m_{top}. The NNLO average is the average of the single-particle-inclusive (1PI) and pair-invariant-mass (PIM) results [12]. 25
FIGURE 2.7. Constraints on the Higgs mass from measurements of m_W and m_{top}. . 26

FIGURE 3.1. The Fermilab accelerator complex. 29
FIGURE 3.2. The DØ detector. 32
FIGURE 3.3. The barrel and disk assemblies within the SMT. 33
FIGURE 3.4. A ribbon of scintillating fiber in the CFT. Ribbons are attached to a curved backing that matches the curvature of the support cylinder. 34
FIGURE 3.5. A typical DØ calorimeter cell. 36
FIGURE 3.6. Schematic view of a portion of the DØ calorimeter. Towers are formed along pseudo-projective rays, which are labeled by their rapidities. . . 37
FIGURE 3.7. The DØ muon detector. 39
FIGURE 3.8. Position of the luminosity counters (LM) around the beam pipe. The silicon tracker and endcap calorimeter positions are also shown. 43

FIGURE 5.1. Contour cut on $\not\!\!E_T$-$\Delta\phi(\not\!\!E_T,\mu)$ for (a) $t\bar{t}$ signal and (b) Z/γ and WW events. The dark solid line shows the contour cut. 67
FIGURE 5.2. Efficiency vs. electron likelihood for $t\bar{t}\rightarrow e\mu$ signal and QCD fake events. 68

FIGURE 6.1. A $t\bar{t}\rightarrow$ dilepton decay. 70
FIGURE 6.2. Parton-level neutrino rapidity distributions for Monte Carlo $t\bar{t}$ samples with various values of m_{top}. Gaussian fits to each distribution are also displayed. 77
FIGURE 6.3. Dependence of the width of parton-level neutrino rapidity distributions on m_{top}. The solid line indicates the parameterization of this dependence. 78

LIST OF FIGURES—*Continued*

FIGURE 6.4. Event weight distributions for two $t\bar{t}$ events with Monte Carlo-generated top quark mass of 175 GeV. 78
FIGURE 6.5. Sums of event weight distributions from Monte Carlo $t\bar{t} \to \mu\mu$ decays, using parton-level information. Distributions are shown for top masses of 140 GeV, 175 GeV, and 200 GeV. This dashed vertical lines indicate the input top mass used in each sample. 79
FIGURE 6.6. Peaks from sums of parton-level event weight distributions versus top quark mass. The dashed line indicates perfect agreement between the event weight peak and input top quark mass. 80
FIGURE 6.7. Sums of event weight distributions from Monte Carlo $t\bar{t} \to \mu\mu$ decays, using particle-level information. Distributions are shown for top masses of 140 GeV, 175 GeV, and 200 GeV. 81
FIGURE 6.8. Peaks from sums of reconstructed particle-level event weight distributions versus top quark mass. The dashed line indicates perfect agreement between the event weight peak and input top quark mass. 82
FIGURE 6.9. Event weight distributions for a 175 GeV Monte Carlo $t\bar{t}$ event with various amounts of detector smearing. 83
FIGURE 6.10. Peaks from sums of reconstructed particle-level event weight distributions versus top quark mass, with 150 smears over detector resolutions applied to each event. The dashed line indicates perfect agreement between the event weight peak and input top quark mass. 84
FIGURE 6.11. Normalized sums of event weight distributions from Monte Carlo $t\bar{t} \to \mu\mu$ decays using particle-level information. Particles in each event are smeared 150 times. Distributions are shown for top masses of 140 GeV, 175 GeV, and 200 GeV. 85
FIGURE 6.12. Average RMS versus top mass for Monte Carlo $t\bar{t}$ samples. 86
FIGURE 6.13. A 175-GeV event weight distribution, before and after rebinning into 25-GeV bins. 86
FIGURE 6.14. Sums of smeared event weight distributions for dominant background processes in the dilepton decay channels. 87
FIGURE 6.15. Event weight distributions for the 15 $e\mu$ events seen in data. 88
FIGURE 6.16. Event weight distributions for the 5 ee events seen in data. 89
FIGURE 6.17. Event weight distribution for the 1 $\mu\mu$ event with non-zero weight seen in data. 89

FIGURE 7.1. Quadratic and cubic fits to an ensemble of 15 ee events. Note that the cubic fit reaches a maximum before reaching the (maximum+0.5) point. 98
FIGURE 7.2. Fraction of dilepton ensembles with good estimates of fit uncertainties from quadratic and cubic fits. 99

LIST OF FIGURES—*Continued*

FIGURE 7.3. Fits in the range (a) ± 5 GeV and (b)± 100 GeV around the minimum for an ensemble of 15 $e\mu$ events at m_{top} = 175 GeV. In Figure (a) the red line indicates the extension of the black fit parabola beyond the ± 5 GeV fit range. 101
FIGURE 7.4. Pull distributions for 1,000 ensembles of 21 dilepton events at (a) 150 GeV, (b) 175 GeV, and (c) 200 GeV. 103
FIGURE 7.5. (a) Linear fit slope, (b) fit offset, and (c) pull RMS vs. fit range and h. 104
FIGURE 7.6. Pull distributions for (a) 120 GeV and (b) 230 GeV input top quark masses. The peaks at ± 1 indicate events in which the likelihood fit minimum is outside the allowed range of 70-280 GeV. 105
FIGURE 7.7. Widths of pull distributions versus m_{top} 106
FIGURE 7.8. Linear fit of -ln$L$ minima to m_{top}. 106

FIGURE 8.1. -ln (Likelihood) minima versus mass for data events in the (a) $e\mu$, (b) ee, and (c) $\mu\mu$ channels. 108
FIGURE 8.2. -ln (Likelihood) minima versus mass in data for the combined dilepton channels. 116
FIGURE 8.3. Distributions of fit minima from 1000 Monte Carlo ensemble tests in the (a) $e\mu$ and (b) ee channels at $m_{top} = 175$ GeV. The arrows indicate the minima observed from data. 117
FIGURE 8.4. Distribution of statistical uncertainties from 1000 Monte Carlo tests on combined dilepton ensembles at $m_{top} = 175$ GeV. The arrows indicates the uncertainty observed from data. 118
FIGURE 8.5. Likelihood minima versus top quark mass for unsmeared events, and for events in which jet energies have been shifted by $\pm 4.4\%$. 118
FIGURE 8.6. Likelihood minima vs. m_{top} using standard, PMCS, and dummy background templates. 119

FIGURE 9.1. World average of m_{top}, from measurements at DØ and CDF. 122
FIGURE 9.2. Recorded luminosity at DØ versus time 124

FIGURE B.1. Top decay with a lepton final product. 131

FIGURE C.1. The Level 1 Muon Trigger system. 135
FIGURE C.2. Level 1 Muon power supply monitor. 136
FIGURE C.3. Trigger Examine plots. Central triggers are in blue, north triggers are in red, and south triggers are in green. 138
FIGURE C.4. Level 1 Muon scintillator, wire, and BOT triggers. 141
FIGURE C.5. Status figures for (a) good distributions, (b) minor alerts, (c) major alerts, and (d) unknown distributions. 143

LIST OF FIGURES—*Continued*

FIGURE C.6. Level 1 Muon *l1muo_analyze* plots. The plots in the upper right, upper left, and lower left mimic those produced by the Trigger Examine tool. The lower left plot shows triggers for each of the p_T thresholds in each octant of the Level 1 Muon trigger. 144
FIGURE C.7. Fractional differences between hardware MTM Triggers and triggers simulated from front end readout. 145
FIGURE C.8. Comparison between hardware MTM Triggers and triggers simulated from Level 1 Muon octant counters. 147
FIGURE C.9. Differences between the simulated CTT TTK(1,10) trigger and the Level 1 Muon hardware TTK(1,10) trigger. 148
FIGURE C.10. Result of consistency check on CTT-based triggers under normal running conditions. 149
FIGURE C.11. Results of consistency check with bad Level 1 Muon firmware. 150
FIGURE C.12. Simulator and hardware excesses for the *mu1ptxalxx* trigger. 152
FIGURE C.13. Simulator and hardware excesses for the *mu1ptxaxlx* trigger. 153
FIGURE C.14. Plots of trigger rates versus luminosity for the *mu1ptxatxx*, *mu1ptxatlx*, and *mu1ptxattx* Level 1 Muon triggers. 155
FIGURE C.15. *mu1ptxatxx* efficiency calculations using (a) Run IIa and (b) Run IIb algorithms. 157
FIGURE C.16. mu1ptxatxx efficiency (a) versus η and (b) versus ϕ. 158
FIGURE C.17. Efficiency versus time for the mu1ptxatxx trigger. 160
FIGURE C.18. Status of all register monitors in the MTCS crate. The green color indicates that all registers are reading back their normal values. 160
FIGURE C.19. GUI used to enable/disable CTT inputs to Level 1 Muon. 162
FIGURE C.20. GUI used to set Level 1 Muon MTM triggers. 164
FIGURE C.21. Map between trigger names and MTM trigger numbers. 165

LIST OF TABLES

TABLE 2.1. Branching ratios for W decay modes. 25

TABLE 4.1. Average muon reconstruction efficiencies 52
TABLE 4.2. Jet energy resolution parameters from data 54
TABLE 4.3. Electron smearing constants in the central (CC) and endcap (EC) calorimeter 54
TABLE 4.4. Jet energy resolution parameters from Monte Carlo 55
TABLE 4.5. Muon Monte Carlo Resolutions 55

TABLE 5.1. Average dilepton trigger efficiencies 58
TABLE 5.2. Total recorded luminosity versus trigger list version 58
TABLE 5.3. Dimuon event selection effficiences 61
TABLE 5.4. Dielectron Event Selection Effficiences 62
TABLE 5.5. Electron-Muon Event Selection Effficiences 63
TABLE 5.6. Expected Yields in Dilepton Channels 66

TABLE 6.1. Expected Yields in Dilepton Channels, including Template Generation Efficiency 76

TABLE 7.1. Likelihood uncertainties for ensemble tests using 10 sub-templates . . 97
TABLE 7.2. Likelihood variances for sub-templates, averaged over all mass points. . 97

TABLE 8.1. Likelihood fit minima for smeared jet and muon samples at $m_{top} =$ 175 GeV. 111
TABLE 8.2. Likelihood fit minima for $t\bar{t}$ and $t\bar{t}$ + 1 jet samples at $m_{top} = 175$ GeV. . 112
TABLE 8.3. Likelihood fitter minima for various PDF samples for $e\mu$ events at $m_{top} =$ 175 GeV. 113
TABLE 8.4. Summary of systematic errors. 116

TABLE A.1. Dimuon trigger requirements for each trigger list version 128
TABLE A.2. Dielectron trigger requirements for each trigger list version 128
TABLE A.3. Electron-muon trigger requirements for each trigger list version 129

ABSTRACT

A measurement of the top quark mass from dilepton decay channels is presented, using approximately 360 pb^{-1} of data colleced by the DØ experiment at Fermilab. The mass is measured from a total of 21 candidate dilepton events, using the neutrino weighting scheme. The measured mass is found to be 175.6$\pm$10.7 (stat.)$\pm$6.0(syst.) GeV. This result is in good agreement with the current world average of the top quark mass.

CHAPTER 1
INTRODUCTION

The history of particle physics mirrors the history of human development. Man has always wondered about what makes up the world around him. From the curiosity of the earliest cavemen to the ancient Greeks' conception of indivisible particles to ...

Hold it.

All of that is a lie, or at least a myth. The idea that the search for fundamental particles represents something, well, fundamental about mankind is a bit of fantasy, told to make the progress of science seem like an inexorable march rather than a drunkard's walk. Until relatively recently, it has not been evolutionarily advantageous for man's curiosity to extend much past the search for food, comfortable shelter, and sex – three quantities that tend to get sacrificed in the search for fundamental particles (see Figure 1.1).

FIGURE 1.1. Owl shift (midnight - 8 AM) at the DØ particle physics laboratory. Note the lack of food, comfort, and sex.

For all the efforts of earlier scientists, the search for fundamental particles as we know them today did not begin in earnest until 1897, with the discovery of the electron by J.J. Thomson. Scientists at Thomson's laboratory immediately heralded the importance of their discovery by declaring the electron to be useless and raising toasts to its lack of utility.

The electron has, of course, proven to be far from useless. On a practical level, it has led to revolutions in computing, communications, and a host of other technologies. Its discovery also paved the way to further explorations of the sub-atomic world. These searches led to a host of newly-discovered particles, with properties so outside common experience that they can only be described as odd (in parity), or strange (in quantum state), or, occasionally, even charming.[1]

As these particles were being found, a theoretical framework was being developed to categorize each discovery and to explain the behavior of each new particle. Theory and experiment built upon one another, growing ever larger and more advanced in their search for the fundamental. Experimental apparatuses have grown from desktop-size bubble chambers to miles-long particle accelerators. Theory has advanced from quantum theory to the Standard Model of particle physics.

This thesis describes efforts made to measure the mass of the heaviest known constituent of the Standard Model, the top quark. The top quark is the most ephemeral of particles, lasting for only a millionth of a millionth of a millionth of a millionth of a second before decaying away. From one viewpoint, this represents a degree of uselessness that would surely have warmed the hearts of Thomson's colleagues. From another viewpoint, though, the top quark is of tremendous value. The properties that may be measured during its brief existence can confirm the predictions of the Standard Model, or point to as-yet-undiscovered physics.

Chapter 2 of this thesis describes the top quark's place within the Standard Model, as well as its uses in probing for new physics. Chapter 3 provides an overview of the only machine currently capable of producing top quarks, the Fermilab Tevatron, and describes

[1] Hey, don't blame me – *I* didn't come up with these names!

the equipment used to detect their existence. Chapters 4 and 5 explain how collisions containing top quark decay products are identified and selected in the experimental data, while Chapter 6 outlines how the mass of the top quark is reconstructed from the properties of its decay particles. A description of the statistical procedures used to find the top quark mass most consistent with observed data is provided in Chapter 7. The result of the mass measurement is revealed in Chapter 8, and the implications of this result are discussed in Chapter 9.

CHAPTER 2
THEORY

By nearly any measure, the Standard Model is a spectacularly successful physical theory. It describes interactions of three of the four known fundamental forces: the strong nuclear force, the weak nuclear force, and electromagnetism. (The fourth force, gravity, falls outside the purview of the Standard Model.) Standard Model calculations of particle properties have shown exceptional agreement with experimental results. The theory has also predicted a number of new fundamental particles whose existence has since been confirmed by experiment [1] [2] [3]. The heaviest such particle, the top quark, was discovered at Fermilab in 1995 [4] [5]. This chapter provides an overview for the mechanism of top quark production in hadron collisions within the Standard Model, as well as a discussion on the importance of the top quark mass within the theory.

2.1 The Standard Model

According to the Standard Model, all matter is made up of quarks and leptons. There are three generations of each, with each quark generation containing a quark with charge $+\frac{2}{3}e$ and a quark with charge $-\frac{1}{3}e$. Each lepton generation contains a charged lepton and an associated uncharged neutrino. Forces between these particles are transmitted via intermediate gauge bosons (Figure 2.1).

The Standard Model combines two theories: quantum chromodynamics (QCD), which describes the strong force, and the electroweak (EW) theory, which unifies electromagnetism with the weak force. Both QCD and EW are local gauge theories, meaning that their Lagrangians are invariant under position-dependent phase translations. Calculations in each are performed by perturbatively expanding in orders of the interaction strength (de-

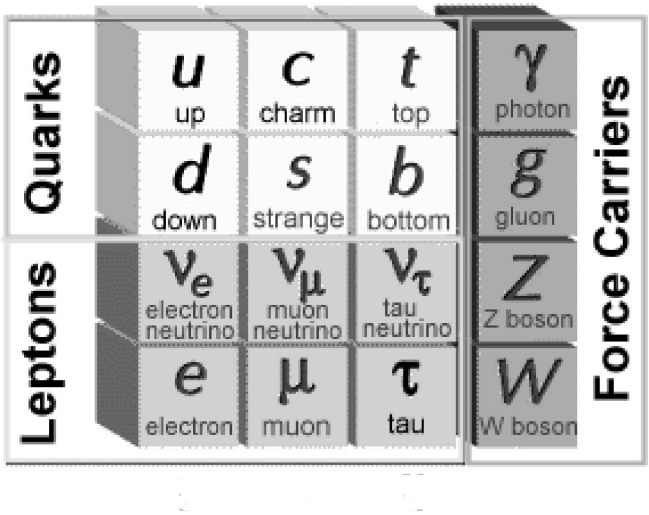

FIGURE 2.1. Fundamental particles within the Standard Model.

fined by a coupling constant, α). In this way, interactions are modeled by summing over individual sub-processes in increasing order of α, as shown in Figure 2.2. Sub-processes such as loop diagrams can introduce divergences into these sums. However, in both theories such divergences can be circumvented through the use of renormalization procedures.

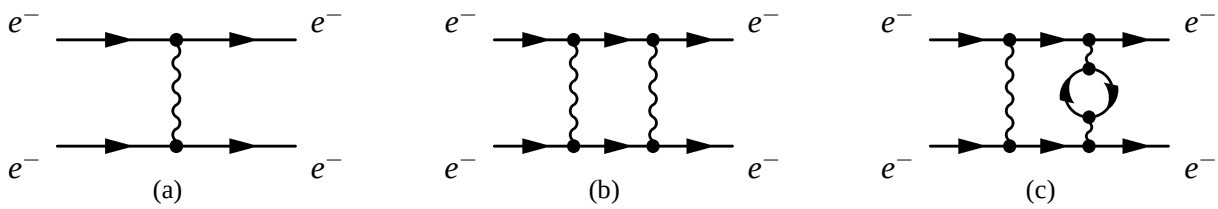

FIGURE 2.2. Contributions to electron-electron scattering from selected (a) leading-order, (b) next-to-leading-order (NLO), and (c) next-to-next-to-leading order (NNLO) processes. Each vertex contributes a factor of $\sqrt{\alpha}$ to the scattering amplitude.

2.1.1 Quantum Chromodynamics

Quantum Chromodynamics is described by an $SU(3)_c$ field, generated by the *color charge*. Each quark carries such a charge, and interactions between quarks are mediated by eight

massless gauge bosons, called gluons. The gluons couple not only to the quarks, but to themselves as well. This causes the coupling constant of the strong interaction to decrease as the momentum transfer μ increases [7]:

$$\alpha_s = \frac{4\pi}{(11 - \frac{2n_f}{3})\ln(\frac{\mu^2}{\Lambda_{QCD}^2})}. \tag{2.1}$$

In the above equation, n_f refers to the number of quarks with masses less than μ, while Λ_{QCD} is a free parameter that must be determined experimentally. Present data [8] sets the value of Λ_{QCD} at a few hundred MeV.

Equation 2.1 illustrates the principle of "asymptotic freedom" – as the energy scale of the interaction increases (or conversely, as the length scale decreases), the coupling constant vanishes. Thus, quarks within a tightly confined space (such as a nucleus) behave as free particles. If one attempts to separate a quark from such confinement, though, the coupling increases in strength, to the point where it becomes energetically more favorable to create a new quark-antiquark pair from the vacuum than to isolate a single quark. This results in hadronization of the quarks.

Equation 2.1 also provides an estimate of the perturbative region of QCD. In order for the perturbative approach to be valid, the coupling constant α_s must be much less that unity. This implies that the energy scale of the interaction must be much greater than Λ_{QCD}. Energies on the order of a few hundred GeV are needed to produce top quarks, indicating that experimental top quark production can be used as a precision test of perturbative QCD calculations.

2.1.2 Electroweak Unification

The electroweak interaction is described by an $SU(2)_L \otimes U(1)_Y$ gauge group, generated by four massless gauge bosons. A doublet of complex scalar Higgs field may also be added to the electroweak Lagrangian. Choosing a particular minimum of the Higgs field spontaneously breaks the symmetry of the Lagrangian, and perturbatively expanding about

this minimum produces additional Goldstone bosons. Exploiting the local gauge invariance of the Higgs field causes the Goldstone bosons to be absorbed (or "eaten") by the gauge bosons, yielding four physical particles: three massive vector bosons and one massless boson. The massive bosons $W^{\pm}$ and Z are identified as the carriers of the weak force, while the massless particle is the familiar photon, the elecromagnetic mediator. This procedure also introduces a new massive particle, the Higgs boson. This is currently the only particle in the Standard Model bestiary that has not yet been observed experimentally.

The existence of the massive bosons was predicted by the electroweak theory years before their discovery. The theory also predicted the relationship between the bosons' masses:

$$\frac{m_W^2}{m_Z^2} = 1 - \sin^2\theta_W, \tag{2.2}$$

where θ_W is the weak mixing angle and is a measure of the respective coupling strengths between the SU(2) and U(1) groups. As with Λ_{QCD}, $\sin^2\theta_W$ is a free parameter, and is measured experimentally to be 0.223 [9]. The discovery of the W and Z bosons at CERN in 1983, and the subsequent measurement of their masses as m_W=80.403$\pm$0.029 GeV and m_Z=91.18$\pm$0.002 GeV [10], in exact conformation with predicted values, remains one of the great triumphs of the Standard Model.

For all the successes of the Standard Model, the theory is not without its limitations. The degree of weak mixing between quark states, described by the Cabibbo-Kobayashi-Maskawa (CKM) matrix, is not predicted by the theory, and the mixing parameters within the matrix must be measured experimentally. The masses of the fundamental fermions must likewise be determined empirically.

The mass of the Higgs boson presents a larger problem. In order to fulfill its role within the Standard Model, the Higgs must be relatively light, with a mass no more than 1 TeV or so. However, the theory also predicts that couplings to the Higgs at an arbitrary energy scale Λ, as shown in Figure 2.3, should introduce a radiative correction to the bare Higgs mass

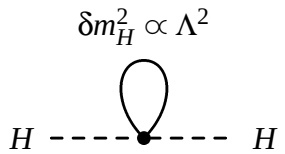

FIGURE 2.3. Higgs mass sensitivity to energy scale Λ.

that is proportional to Λ^2. At Grand Unification scales, this causes the so-called "hierarchy problem", as any massive particles associated with new physics cause the mass of the Higgs to diverge. Furthermore, a fundamental Higgs must have a self-coupling that goes to zero at some finite energy, a condition that eliminates the symmetry-breaking property of the particle.

The exact nature of the Higgs can thus provide confirmation of the Standard Model or point to new physics. Earnest attempts are being made to detect the Higgs directly [11]. In the absence of direct observation, constraints on the Higgs mass can be made indirectly, through the measurement of the mass of the top quark.

2.2 Top Quark Production

Top quarks are produced predominantly in $t\bar{t}$ pairs at the Tevatron, via QCD interactions between the partons within colliding protons and antiprotons. The dominant production processes come from $q\bar{q}$ annihilation and gluon-gluon fusion, as shown in Figure 2.4. At the Tevatron's center-of-mass energy of 2 TeV, perturbative QCD may be used to calculate the production cross sections for these processes. The $t\bar{t}$ cross section is found to be on the order of a few picobarns, with roughly 85% of the $t\bar{t}$ pairs coming from $q\bar{q}$ annihilation [12]. This compares to an overall inelastic $p\bar{p}$ cross section of ~ 50 mb, so that nearly ten billion collisions are needed to create a single $t\bar{t}$ pair.

The decay of the top quark is governed by weak interaction and the V_{tb} term in the CKM matrix. The magnitude of this term has been measured directly from observations of top

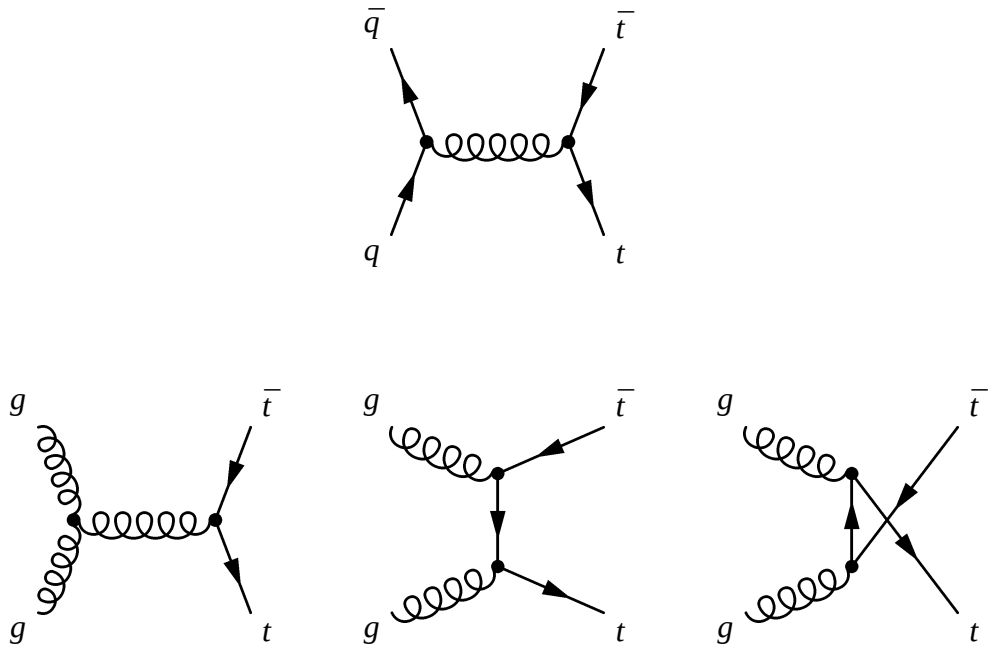

FIGURE 2.4. Leading-order $t\bar{t}$ QCD production processes.

quark decay, but the uncertainty on this measurement is large [13]. However, limits on the magnitude can also be inferred from decays of lighter quarks by combining the unitarity of the CKM matrix with the assumption that there are only three generations of quarks. This assumption leads to a constraint that [14]

$$0.9991 < |V_{tb}| < 0.9994. \tag{2.3}$$

Such a constraint indicates that the top quark decays almost exclusively to a b quark and a W boson, as shown in Figure 2.5. If the masses of the W boson and the b quark are neglected, a tree-level calculation of the top quark decay width yields:

$$\Gamma(t \to W_b) = \frac{G_F}{8\pi\sqrt{2}} m_{top}^3, \tag{2.4}$$

where G_F is the Fermi coupling constant. For a top quark mass of 175 GeV, the decay width is approximately 1.8 GeV. Of course the masses of the W boson and the b quark are not negligible; including them reduces the decay width to 1.4 GeV [15]. This width is

larger than Λ_{QCD}, indicating that the top quark lifetime is less than the QCD timescale, so that the top quark decays before it hadronizes.

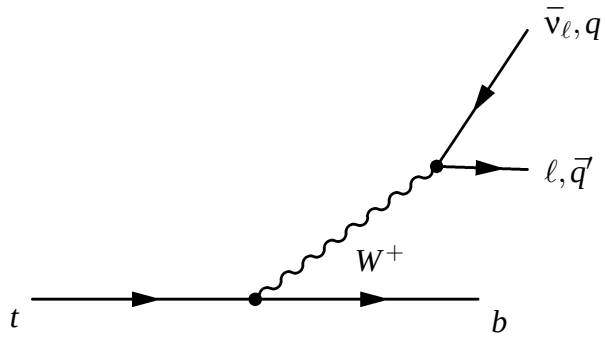

FIGURE 2.5. Dominant decay mode of the top quark

The b quark does hadronize before it decays, producing a high-momentum particle "jet". The W boson may decay either hadronically or leptonically. Table 2.1 shows that the $t\bar{t}$ decay modes are categorized according to the decays of the W bosons in the event.

This analysis makes use of "dilepton" decays of $t\bar{t}$ pairs; that is, decays in which each W boson decays to either an electron or a muon. (Decays to tau leptons are not considered, as taus are not easily identifiable with the DØ detector.) Such events contain two high-momentum jets from the b quarks, two high-momentum leptons, and a significant imbalance in the total measured momentum due to the undetected neutrinos. The $t\bar{t}$ branching ratio for these processes is only $\approx 5\%$, but this low ratio is offset by the fact that the likelihood of background processes producing such an event signature is also small.

2.3 Measurement of the Mass of the Top Quark

As mentioned above, the $t\bar{t}$ production cross section at the Tevatron is on the order of a few picobarns. As Figure 2.6 shows, the exact value of the cross section predicted by the Standard Model is dependent on the mass of the top quark. Thus, a precision measurement

TABLE 2.1. Branching ratios for W decay modes.

	$W \to e\bar{\nu}_e$	$W \to \mu\bar{\nu}_\mu$	$W \to \tau\bar{\nu}_\tau$	$W \to qq'$
$W \to e\bar{\nu}_e$	1/81	1/81	1/81	2/27
$W \to \mu\bar{\nu}_\mu$	1/81	1/81	1/81	2/27
$W \to \tau\bar{\nu}_\tau$	1/81	1/81	1/81	2/27
$W \to qq'$	2/27	2/27	2/27	4/9

of the top quark mass can be combined with a cross section measurement to provide a test of Standard Model predictions.

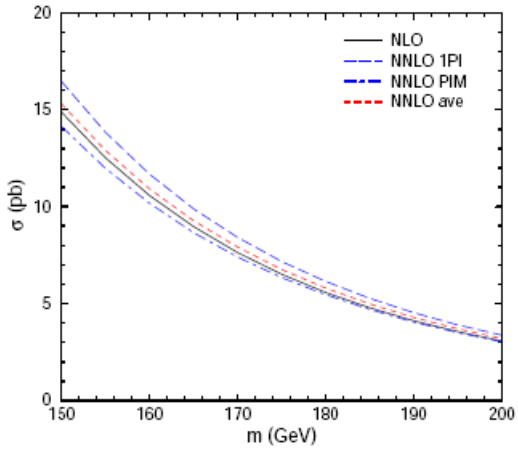

FIGURE 2.6. Dependence on the $t\bar{t}$ production cross section on m_{top}. The NNLO average is the average of the single-particle-inclusive (1PI) and pair-invariant-mass (PIM) results [12].

A measurement of the top quark mass also may be used to constrain the allowed mass for a Standard Model Higgs. This is accomplished by considering the effect of radiative corrections on the mass of the W boson. At lowest order, the W mass is given as:

$$m_W = \frac{\sqrt{\frac{\pi\alpha}{\sqrt{2}G_F}}}{\sin\theta_W} \equiv \frac{A}{\sin\theta_W}, \tag{2.5}$$

where α is the fine structure constant. Couplings of the W to the top quark and Higgs boson lead to the introduction of a corrective term Δr in the W mass:

$$m_W = \frac{A}{\sin\theta_W \sqrt{1-\Delta r}}. \tag{2.6}$$

In the above equation, Δr contains a term proportional to m_{top}^2 and a term with a logarithmic dependence on the Higgs mass: $\Delta r_{Higgs} \propto ln(\frac{m_H}{m_Z})$. Thus, precision measurements on both m_{top} and m_W can provide a constraint on the Higgs mass (Figure 2.7).

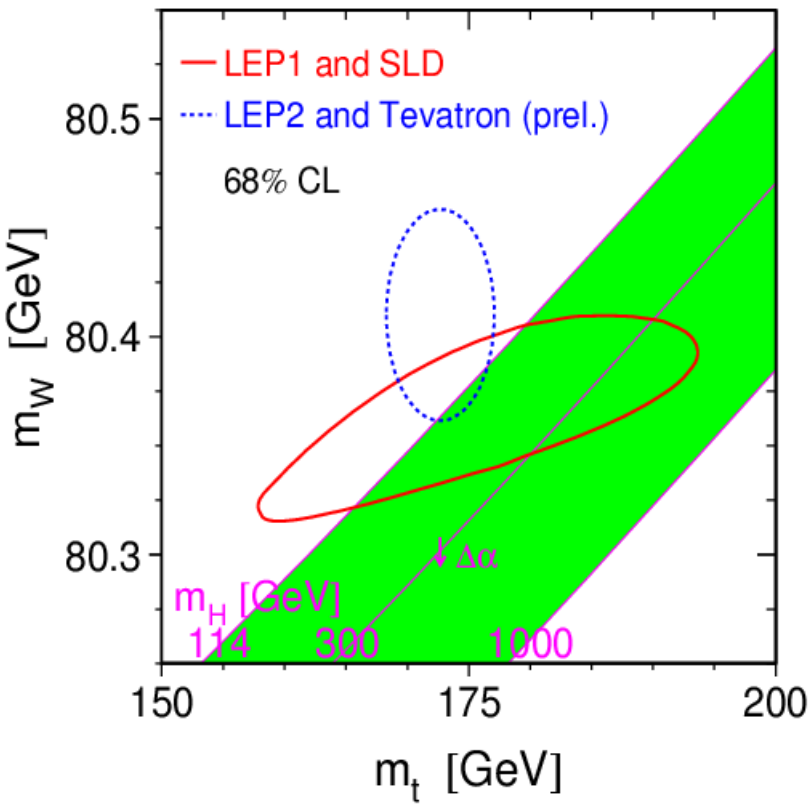

FIGURE 2.7. Constraints on the Higgs mass from measurements of m_W and m_{top}.

2.4 A Note on the Top Quark Mass

Because quarks are not observed as free particles, the term "quark mass" does not have a unique definition. Different computational methods may result in different definitions of

quark mass. The “pole mass” is defined as the pole of the quark propagator in perturbative QCD. Attempts to treat QCD non-perturbatively lead to the definition of an HQET (Heavy Quark Effective Theory) quark mass, which introduces differences of the order α_s^2 to the pole mass [16]. Still other model-dependent definitions ($m_{top}^{\overline{MS}}$, m_{top}^{GP}, etc.) also exist. Throughout this dissertation, all discussions of quark mass refer to the pole mass.

CHAPTER 3
EXPERIMENTAL APPARATUS

Top quark pairs are produced at Fermilab from collisions between protons and antiprotons in the Tevatron accelerator. The Fermilab Tevatron is the world's largest proton-antiproton ($p\bar{p}$) collider, a kilometer-radius synchrotron that collides particles at a center-of-mass energy of 1.96 TeV. Two detectors (CDF and DØ) are placed at intersecting regions in the Tevatron where these collisions take place. These detectors must be capable of identifying quark jets, electrons, and muons produced in top quark decays, and must also detect the presence of any neutrinos within the decays. This analysis makes use of data collected by the DØ detector, a multi-purpose detector consisting of a central tracker (for measuring the momentum of produced particles), a calorimeter (for identifying and measuring the energy of jets and electrons), and a muon spectrometer. The Tevatron accelerators are discussed more fully in [17]. A detailed description of the DØ detector appears in [18].

3.1 Fermilab Accelerators

Protons to be used in the Tevatron are collected from from a source of 18 keV H^- ions. These protons are increased in energy through a series of five accelerators, ending in the Tevatron at an energy of 980 GeV (Figure 3.1). Protons are also collided with a nickel target to create antiprotons, which are in turn gathered and stored for later use in accumulator and recycler rings. The anti-protons are also accelerated to 980 GeV in the Tevatron.

Charged particles may be accelerated by the application of external electric fields. Perhaps the simplest method of acceleration is to place the particles within a constant electric field, produced by two electrodes at different potential. This is achieved at Fermilab with a Cockcroft-Walton pre-accelerator, an electrostatic accelerator that increases the energy of

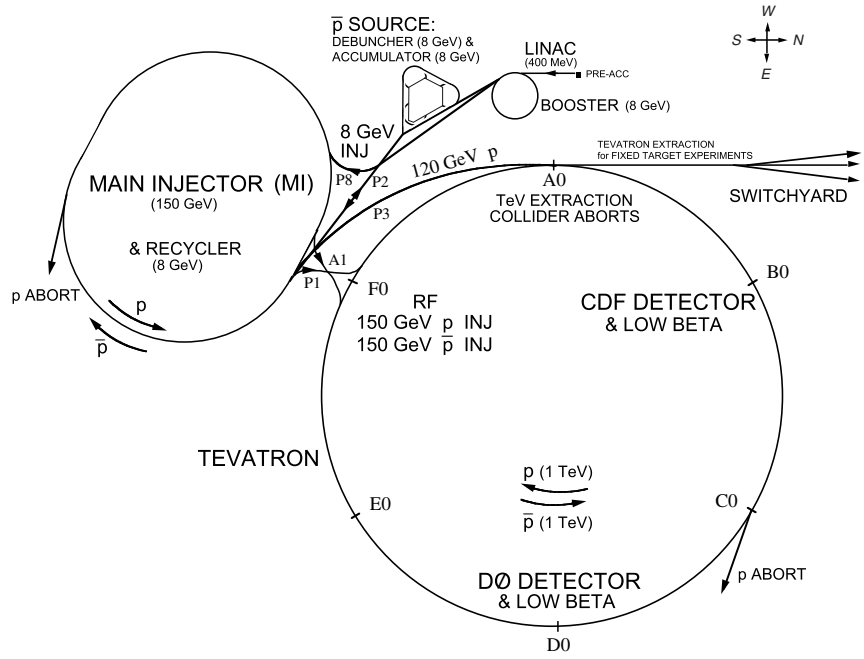

FIGURE 3.1. The Fermilab accelerator complex.

the H^- ions from 18 keV to 750 keV.

Electrostatic accelerators can only be used for a limited energy range, as very large energy differences lead to sparking between the electrodes. Acceleration to higher energies require the use of alternating radiofrequency (RF) fields. A charged particle exposed to an RF field will experience no net acceleration, as the accelerating and decelerating phases of the field will cancel one another. However, the acceleration may be made non-zero by shielding the particle within conductive material during the decelerating phases of the RF field. This is done at Fermilab in the Linac, a 146 meter-long linear accelerator containing an alternating series of RF cavities and conducting tubes. The Linac accelerates H^- ions from 750 keV to 400 MeV.

Linear accelerators also have their limits, as space constraints limit the length of the accelerators. To accelerate protons to 980 GeV with Linac fields would require an accelerator dozens of kilometers long! Such an arrangement would be both cost- and space-prohibitive, so circular synchrotron accelerators are used instead for further acceleration.

A synchrotron uses dipole electromagnets to steer charged particles in a circular path of fixed radius while increasing their energy. This requires a more complex design than that used for the Linac, as both the magnetic field and the accelerating potential on a particle must continually increase in order to accelerate the particle while keeping it at a fixed radius while it accelerates. Additionally, because a given electromagnet can produce only a limited range of fields, acceleration within a synchrotron cannot continue indefinitely.

A set of three synchrotrons is used to accelerate protons to their final energy of 980 GeV. The first of these is the Booster, which accepts the 400 MeV H^- ions from the Linac. In their passage from the Linac to the Booster, the ions are stripped of their electrons, leaving only protons behind. The Booster groups the protons into "bunches" and accelerates them to 8 GeV. The protons then pass to the Main Injector, which merges all protons into a single bunch and accelerates them to 150 GeV. From there, the protons are injected into the Tevatron.

The Main Injector is also used in the production of antiprotons. Protons in the Main Injector are accelerated to 120 GeV and are then transported to a nickel target. The target consists of 10 cm-diameter nickel disks separated by copper cooling disks. Protons colliding with the nickel targets produce 8 GeV antiprotons at the rate of one to two antiprotons per 100,000 collisions. These antiprotons are gathered with a lithium collection lens, and are separated from other produced particles by means of a pulsed dipole field. The antiprotons are sent to the Debuncher ring, which applies stochastic cooling to reduce the momentum spread of the particles. They are then passed to the Accumulator ring for storage.

The efficiency for gathering new antiprotons decreases as the number of antiprotons within the Accumulator increases [19]. During antiproton production, bunches of antiprotons are periodically sent to the Recycler, a separate antiproton storage ring located directly below the Main Injector. This allows the Accumulator to maximize its antiproton collection rate. The Recycler may also be used to gather unused antiprotons at the end of a set of $p\bar{p}$ collisions for later use. Antiprotons from either the Recycler or the Accumulator may

be accelerated by the Main Injector and passed to the Tevatron.

The Tevatron makes use of superconducting niobium/titanium magnets to provide a much stronger magnetic field than is available to either the Booster or Main Injector, allowing for acceleration to much higher energies. Bunches from the Main Injector are coalesced into a single bunch, and are passed into the Tevatron. When the Tevatron contains 36 bunches of protons, this procedure is repeated for the antiprotons, producing a 36×36 store of proton and antiproton bunches.

Particle bunches are accelerated in the Tevatron from 150 GeV to 980 GeV. Protons and antiprotons cycle through the Tevatron in helical orbits within a shared beam pipe. A set of twenty-four electrostatic separators, spaced throughout the Tevatron, keeps the particles from colliding outside of the DØ and CDF detectors. Collisions are initiated at those regions by means of focusing magnets, called low-beta quads, which tighten the diameter of the proton and antiproton beams to 40 μm. The proton and antiproton beams cross one another at each detector every 396 ns.

3.2 The DØ Detector

As described in Chapter 2, $t\bar{t}$ decays can produce jets, electrons, muons, and neutrinos. The DØ detectors consists of three subsystems that allow it to identify these particles: a central tracking system that produces precision vertex and momentum measurements, a liquid argon/uranium calorimeter that measures jet and electron energies, and a muon spectrometer. Locations within the detector are described by a right-handed coordinate system, as shown in Figure 3.2, with the $+y$ axis pointing upward and the $+z$ axis pointing in the direction of travel of the proton beam. Particles within the detector are also described by the radial distance to the beamline r, as well as by the azimuthal angle ϕ and the polar angle θ. The polar angle is more commonly described by the pseudorapidity η, defined as $\eta = -\ln[tan(\theta/2)]$.

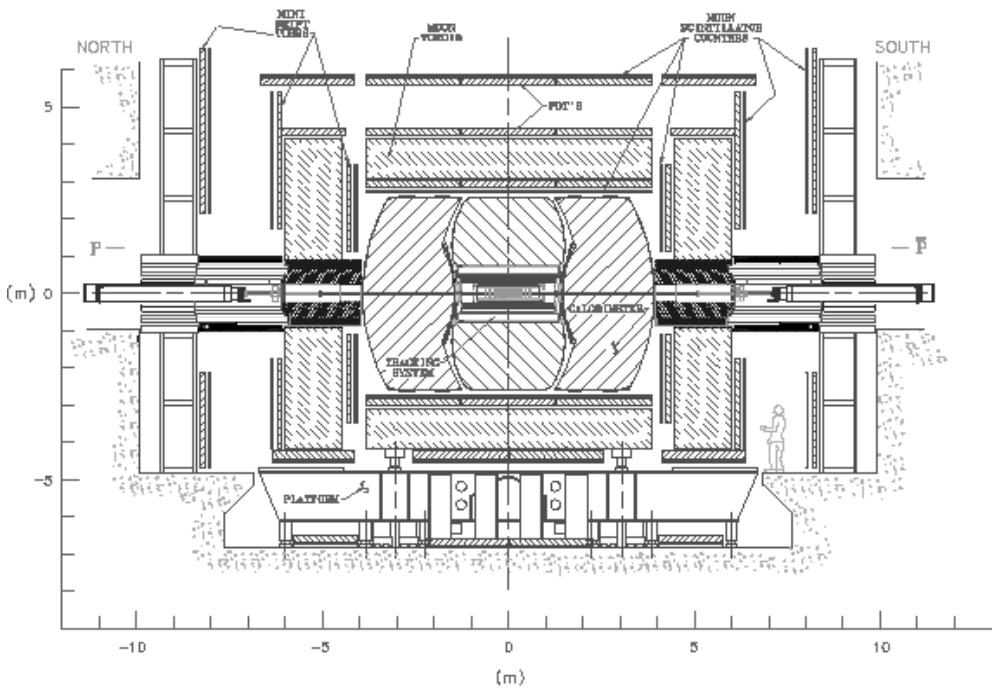

FIGURE 3.2. The DØ detector.

3.2.1 Tracking

The central tracker consists of the Silicon Microstrip Tracker (SMT) and a surrounding Central Fiber Tracker (CFT) contained within a solenoid magnet. The solenoid is wrapped with two layers of superconducting Cu:NbTi multifilament, and provides a field of 2 T. Together, the SMT and CFT provide precision measurements of the momentum of charged particles, and can locate the primary collision vertex with a resolution of 35 μm along the z axis. High-momentum jets from b quarks may also be tagged, with an impact parameter resolution of under 15 μm in the $r-\phi$ plane at η =0.

Silicon Microstrip Detector The SMT consists of six sets of alternating barrel and disk detectors, capped at the ends by additional groups of disk detectors (Figure 3.3). This arrangement allows for the Tevatron's long interaction region ($\sigma = 25$ *cm*) and provides detector surfaces perpendicular to particle paths for a wide range of particle η. The barrel detectors measure trajectories in the $r-\phi$ plane, while the disk detectors provide measure-

ments in both $r-\phi$ and $r-z$. Together, the disks and barrels contain a total of 792,576 readout channels.

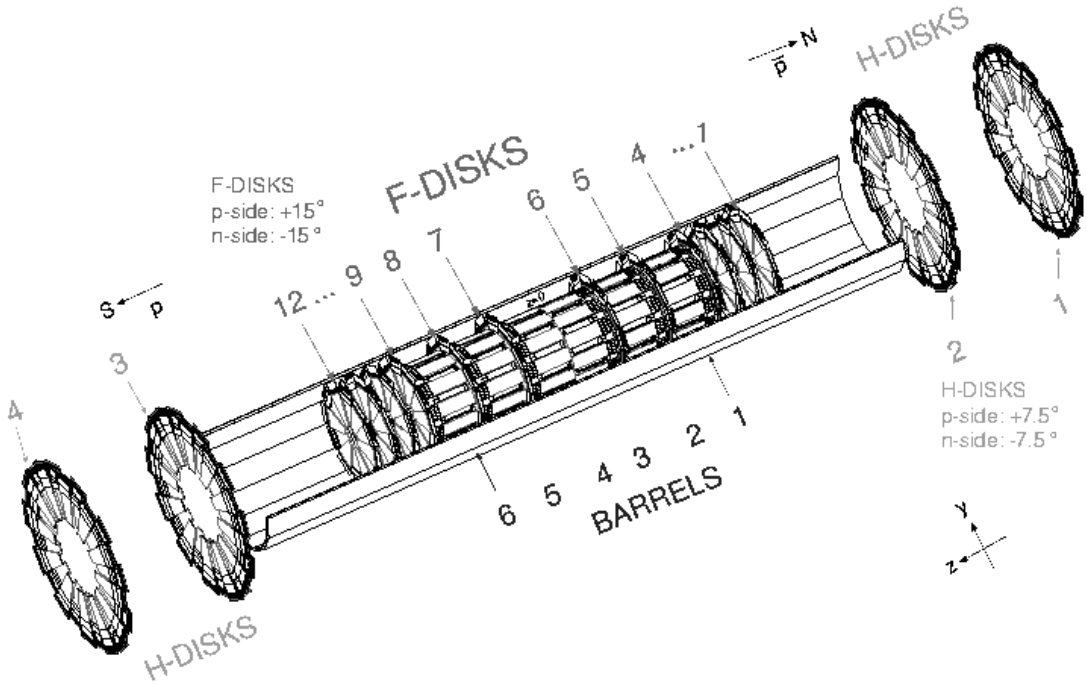

FIGURE 3.3. The barrel and disk assemblies within the SMT.

Each barrel contains four layers of silicon arranged radially, with radii ranging from 2.6 cm to 10.5 cm. The first and third layers of silicon in the innermost four barrels are made of 90° stereo sensors of double-sided, double-metal silicon. The outer two barrels use single-sided silicon aligned along the beam axis in their first and third layers. The second and fourth layers of silicon in all barrels contain strips of double-sided sensors. The p-side strips in these layers are arranged axially, while the n-side strips are arranged at a 2° stereo angle.

At the end of each barrel is an "F-disk" detector, a set of 12 trapezoidal wedge detectors. Three additional F-disks sit outside the outermost barrel-disk assembly, and are capped by two large-diameter "H-disks". The F-disks are made of double-sided silicon, with the p-side and n- side aligned to provide a 30° stereo angle. The H-disks consist of 24 wedges of back-to-back single-sided silicon, with an effective stereo angle of 15°. The barrel/F-disk

assemblies provide coverage in the range $|\eta| < 1.5$, while the H-disks extend that coverage to $|\eta| = 3.0$.

Central Fiber Tracker The CFT is made up of eight concentric cylinders of scintillating fibers, ranging in radius from 20 cm to 52 cm. The two inner cylinders are 1.66 m long, while the remaining cylinders are 2.52 m long, providing full coverage out to $|\eta| = 1.6$. Each scintillating fiber is 835 μm in diameter, and is arranged on a cylinder in ribbons of fiber doublets, as in Figure 3.4. The ribbons contain two layers of 128 fibers each, and are arranged so that the second layer is offset from the first by half a fiber diameter. The eight CFT cylinders contain two ribbons apiece, one aligned along the z axis, and one aligned at an stereo angle of $\pm 3^\circ$. (The stereo angle ribbons are alternated, so that all odd-numbered cylinders use $+3^\circ$ ribbons, while all even-numbered cylinders use -3° ribbons.) The fiber doublets provide for an inherent CFT position resolution of about 100 μm.

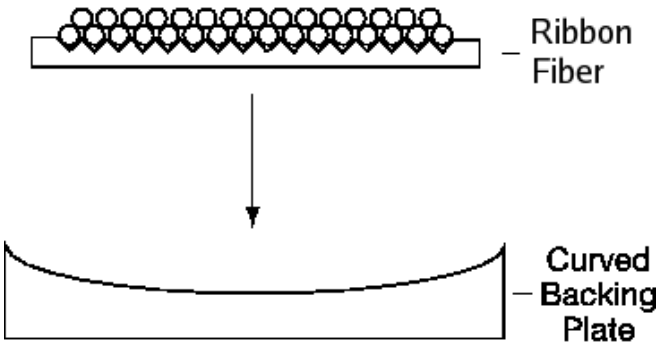

FIGURE 3.4. A ribbon of scintillating fiber in the CFT. Ribbons are attached to a curved backing that matches the curvature of the support cylinder.

The passage of charged particles through the scintillating fibers cause the fibers to emit light. This light is reflected through waveguides to the Visible Light Photon Counters (VLPCs). VLPCs are high-gain, fast-response silicon avalanche photodetectors that can detect a single photon The VLPCs accept a total of 76,800 signal channels, from approximately 200 km of scintillating fiber. Signals from the VLPCs are amplified by Analog Front Boards (AFEs), and those signals are used for readout and triggering purposes.

Tracks found in the CFT are segmented into eighty 4.5° sectors in ϕ. These tracks can then be matched with information from other detectors.

3.2.2 Calorimeter

The DØ calorimeter measures the energies of all particles passing through it, with the exception of neutrinos (which pass through the calorimeter undetected) and muons (which leave only a minimally-ionizing particle signature). The innermost section of the calorimeter is the electromagnetic calorimeter (EMC), which measures electron and photon energies. This is surrounded by the fine hadronic (FHC) and coarse hadronic (CHC) calorimeters, which measure the energies of all other particles.

The EMC works on the principle that a collision between an incident particle and a heavy absorber will induce a shower of particles, from which the energy of the incident particle may be deduced. High-energy electrons radiate energy primarily through bremsstrahlung, while high-energy photons dissipate energy through pair production. Thus, a single high-energy electron may produce a bremsstrahlung photon, which then produces an electron-positron pair of its own, and so on. The size of the resulting shower of electrons and photons may then be used as a measure of the energy of the original particle.

The hadronic calorimeters work similarly, with showers produced by the collisions of hadrons with absorber nuclei. Such showers are more intricate than those in the EMC, given the complexity and number of nuclear reactions that may take place. Furthermore, some reactions may produce muons or neutrinos undetectable by the calorimeter, necessarily worsening its response. Nonetheless, the principle behind the hadronic calorimeters is the same as for the EMC.

A typical DØ calorimeter cell is shown in Figure 3.5. A grounded heavy absorber is used to initiate a particle shower. In the EMC, 3-4 mm of depleted uranium is used as the absorber. Six millimeters of uranium/niobium alloy are used in the FHC, while the CHC uses 46.5 mm of copper or stainless steel. A signal circuit board is covered with a resistive

coating and is charged to a potential of 2 kV. The 2-3 mm gap between the absorber and signal board is filled with liquid argon, which samples the ionizing particles produced by the shower. This charge is collected by the signal board. Several such boards at the same η and ϕ combine to form a single readout cell.

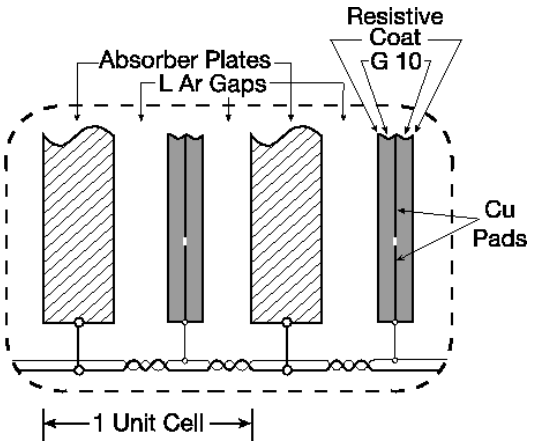

FIGURE 3.5. A typical DØ calorimeter cell.

The DØ calorimeter is divided into three sections: a central calorimeter (CC) that provides energy measurements out to $|\eta| < 1.0$ and two end cap calorimeters (EC) that provide measurements in the region $1.4 < |\eta| < 4.0$. The calorimeter cells in each region are arranged in pseudo-projective towers, as shown in Figure 3.6, with the center of each cell in a given tower lying along the same line to the interaction point. The tower size is generally set as $\Delta\eta = 0.1$, $\Delta\phi = 0.1$. Cells are segmented twice as finely in η and ϕ in the third layer of the central EMC, where electromagnetic showering is at its maximum. Additionally, cells at large $|\eta|$ have increased $\Delta\eta$ and $\Delta\phi$. The calorimeter is more fully described in [20].

There are four layers of readout cells in the central and endcap EMCs. The CC also contains three layers of fine hadronic modules and a single coarse hadronic module. The EC calorimeter is divided into inner, middle, and outer portions. The inner and middle portions are made up of four layers of fine hadronic modules and one coarse hadronic module, while the outer portion contains only a coarse hadronic module.

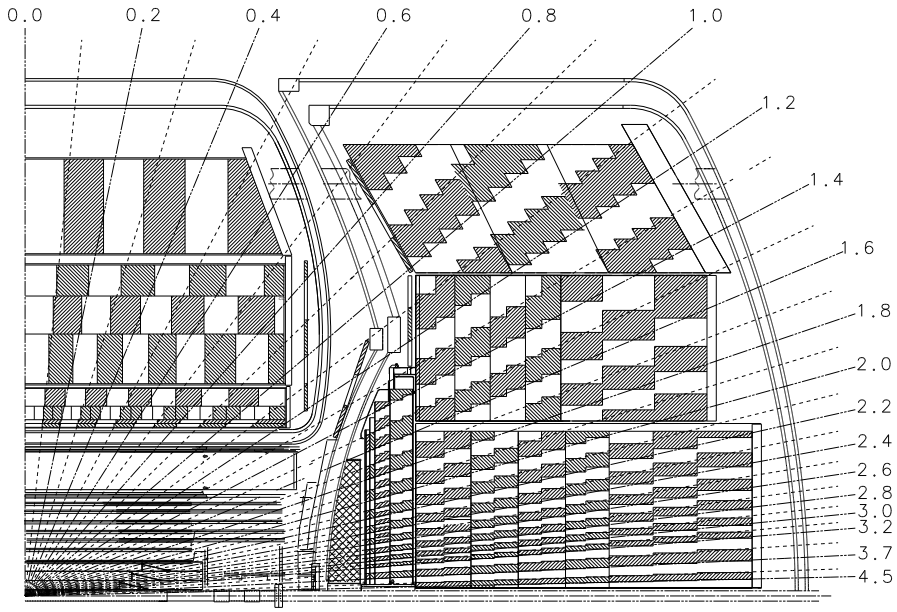

FIGURE 3.6. Schematic view of a portion of the DØ calorimeter. Towers are formed along pseudo-projective rays, which are labeled by their rapidities.

The calorimeter resolution is $\approx$ 5-7 % for electrons with energies above 20 GeV. The hadronic resolution is worse, and is approximately 30% for 20 GeV jets. These resolutions are discussed in more detail in Chapter 4.3.

3.2.3 Preshower Detectors

Preshower detectors between the solenoid and the calorimeter improve the matching between central tracks and calorimeter showers and augment the particle identification abilities of the detectors. The Central Preshower Detector (CPS) surrounds most of the CFT, extending over the region $|\eta| < 1.3$. The CPS is made up of three layers of scintillation counters, with the first layer aligned axially and the second (third) layer aligned at a stereo angle of $+23.8^\circ$ (-24.0°). This aids in distinguishing charged particles from photons, as CPS hits from charged particles will have a matching track from the CFT, while hits from photons will have no such track.

Forward Preshower Detectors (FPS) are mounted on the endcaps of the calorimeter,

in the region $1.5 < |\eta| < 2.5$. Each detector contains a double layer of scintillator strips (the "MIP layer") aligned along the z axis, followed by a stainless steel absorber and a second set of double-layered scintillator (the "shower layer"). These detectors allow heavy particles to be distinguished from electrons and photons. Heavy particles are not likely to shower in the absorber, and will produce only minimum-ionizing particle (MIP) signatures in each set of scintillators. Electrons will create a similar signature in the MIP layer, but will shower in the absorber, leading to a large cluster of energy in the shower layer. Photons leave no signal in the MIP layer, but create a shower signal in the shower layer.

3.2.4 Muon Detector

The bremsstrahlung radiation cross section for a charged particle is roughly proportional to the inverse square of the mass of that particle [21]. Thus, a muon, with a mass 200 times that of an electron, will experience far less bremsstrahlung than the electron in the calorimeter. The muon leaves only an MIP signature within the calorimeter, insufficient for measuring its energy.

Instead, the muon is detected with three layers of scintillators and drift tubes lying outside the calorimeter (Figure 3.7). These layers are labeled "A", "B", and "C" in order of increasing distance from the interaction point. The scintillators provide precision timing measurements for the muon, while the drift tubes measure its position. A 1.8 T toroidal field between the first and second layers of muon detectors allows for a measurement of muon momentum. Hits in the muon detectors may also be matched with tracks from the central tracker to provide a more precise momentum measurement.

Scintillation Counters There are two layers of scintillator counters in the region $|\eta| < 1$. The $A\phi$ counters lie within the toroid, and the *cosmic cap* (CMSC) and bottom counters triggers lie outside the toroid. Each scintillation counter is made of Bicron 404A scintillator connected to a photomultiplier tube. The Aϕ counters are segmented in 4.5° in ϕ, to match the segmentation of the CFT sectors. Each counter spans 33.25 inches in z, which allows for

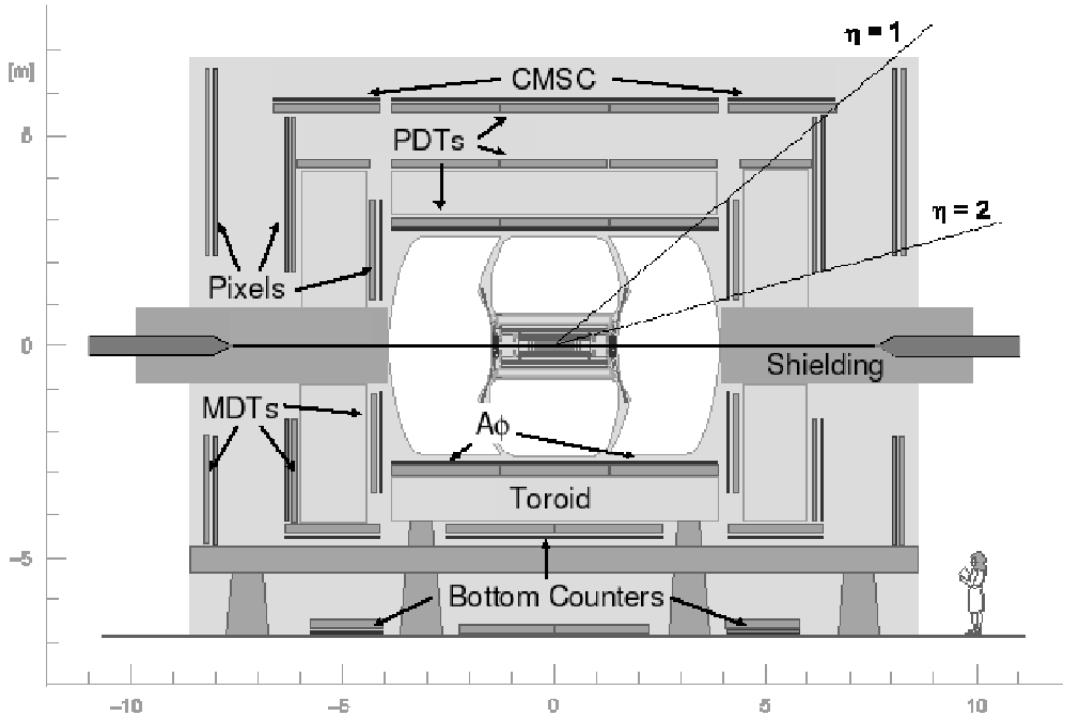

FIGURE 3.7. The DØ muon detector.

matching of the scintillator counters with the central drift tubes described in the following section. The CMSC counters cover the region $-\pi/4 < \phi < 5\pi/4$, and are arranged to provide maximum resolution in the η direction. The bottom counters occupy the remaining space in ϕ, and are oriented with their narrow dimensions in ϕ in order to better match with tracks from the CFT. Because much of the space in the bottom region is taken up by detector supports, the coverage of the bottom counters is incomplete. The central muon system is described in more detail in [22].

In the forward region of the muon system ($1 < |\eta| < 2$), there are three layers of scintillation counters ("pixels"). The pixels are arranged in a set of 12 concentric rings, segmented in η by 0.12 (0.07) for the inner nine (outer three) rings. As with the central counters, the pixels are made of Bicron 404A scintillator, and are segmented in 4.5° increments in ϕ.

The A-layer of the pixels is within the toroid, while the B- and C- layers lie outside the toroid.

Shielding placed around the beam pipe significantly decreases backgrounds seen in the forward muon system from interactions of proton and antiproton fragments with the Tevatron's low beta quad magnets. The shielding consists of 40-50 cm of iron to absorb hadronic and electromagnetic radiation, an additional 15 cm of polyethylene to absorb neutrons, and a final 5 cm of lead to block gamma rays. The three layers of shielding combine to reduce the occupancy of muon detectors by a factor of 50-100 from their unshielded rates [22]. This reduction allows both the forward and central scintillator systems to be used for triggering on muons. The scintillators also provide precision timing measurements for reconstructing muons offline, with a timing resolution of about 2 ns.

Drift Tubes The central region is covered by a total of 94 proportional drift tubes (PDTs) arranged in three layers. As is the case with the central scintillators, drift tube coverage in the central bottom region is limited by support structures for the detector. However, nearly 90% of the central region is covered by two layers of PDTs, and roughly 55% is covered by three layers.

Each PDT chamber is made up of decks of individual 10.1 cm x 5.5 cm cells, with 24 cells per layer [1]. A-layer PDTs contain four decks of cells, and are placed within the toroid so as to overlap the Aϕ counters. B- and C-layer counters contain three decks each. A gas mixture of 84% argon, 8% methane, and 8% CF_4 is used within the drift tubes, and provides a maximum drift time of 500 ns. This is longer than the 396-ns spacing between collisions, and so PDT hits must be confirmed by scintillation counter hits when triggering on or reconstructing muons. Muon positions can be measured within each PDT cell with an uncertainty of roughly 1 mm.

The forward region makes use of smaller mini drift tubes (MDTs) comprised of 1 cm^2 cells. Each MDT contains eight such cells. Planes of four (for the A-layer) or three (for

[1] The highest-$|\eta|$ B-layer PDTs are an exception to this rule, with only 21 cells per layer.

the B- and C- layers) MDTs are mounted along the field lines of the toroid. The MDTs use a separate gas system from the PDTs, a 9:1 $CF_4 - CH_4$ mixture that provides a maximum drift time of 60 ns. The hit position resolution from the MDTs is approximately 0.7 mm, and the momentum resolution from hits only in the muon system (that is, without matches to central tracks) is about 20% for muons below 40 GeV.

3.3 Triggering at DØ

Proton-antiproton collisions occur every 396 ns at DØ, a rate of over 2.5 MHz. DØ's data acquisition (DAQ) system is only capable of writing approximately 50 Hz to tape. Three levels of triggering are used to filter events and to reduce the event rate to meet the DAQ specifications.

The first level ("Level 1") is a set of hardware-based triggers from each of the detector subsystems. The tracker, calorimeter, and muon systems each have their own Level 1 triggers that search for objects consistent with detector signatures of elementary particles. The combined Level 1 triggers provide a trigger event rate of 1.6 kHz. Prescales may be applied to individual Level 1 triggers, so that only a fraction of triggered events are selected for further processing.

Events that pass Level 1 triggers are passed to the "Level 2" hardware trigger system. The Level 2 system is a software-based digital signal processing trigger system. It consists of preprocessors that generate triggers from data from individual detector subsystems, much as the Level 1 system does [23]. Level 2 also has a global processor that forms event-wide triggers based on the combined data from all subsystems. Level 2 reduces the trigger rate by a factor of two, and passes remaining events to the "Level 3" trigger.

Level 3 is a fully programmable software trigger that provides limited event reconstruction [24]. The trigger is made up of approximately 100 "farm nodes". An event that passes a Level 2 trigger is sent to one of these nodes, which unpacks the raw data from the event and reconstructs physics objects from the data. Filters are applied that may impose re-

quirements on individual objects, such as a minimum momentum for muons or jets. Filters may also be applied to non-physics objects, such as the scalar or vector sums of transverse energy within the calorimeter. (The scalar sum tests for large numbers of energetic decay particles, while a non-zero vector sum indicates the production of an undetected neutrino within the event.) Events that meet the trigger filter conditions are written to tape at a rate of 50 Hz.

3.4 Luminosity

The triggers select only a small sample of events from inelastic $p\bar{p}$ collisions. In order to make an accurate determination of the production rate for any particular process, the overall rate of $p\bar{p}$ collisions must also be known. This rate is measured via the luminosity $\mathcal{L}$, defined as

$$\mathcal{L} = \frac{\bar{N}}{T\sigma_{\mathrm{p}\bar{\mathrm{p}}}}, \tag{3.1}$$

where $\bar{N}$ is the average number of inelastic collisions per crossing, $T = 396$ ns is the time between beam crossings, and $\sigma_{\mathrm{p}\bar{\mathrm{p}}} = 46.0 \pm 2.6$ mb is the cross section for inelastic $p\bar{p}$ collisions [25].

DØ contains a dedicated luminosity measurement system, made up of two groups of twenty-four scintillators arrayed along the z axis between the beam line and the Forward Preshower Detector, as shown in Figure 3.8. Particles from $p\bar{p}$ collisions create hits in each group of scintillators in coincidence. These coincidences provide for a counter that fires on any beam crossing with a $p\bar{p}$ collision. However, since the counter does not reflect the number $\bar{N}$ of $p\bar{p}$ collisions per crossing, simply counting the coincidence rate produces an underestimate of luminosity when $\bar{N} > 1$.

Instead, the luminosity is determined by counting the fraction f_{null} of beam crossings in which the counter coincidence does not fire. The number of collisions per crossing is assumed to follow Poisson statistics, so that $\bar{N} = -\ln(f_{\mathrm{null}})$. Thus, the instantaneous

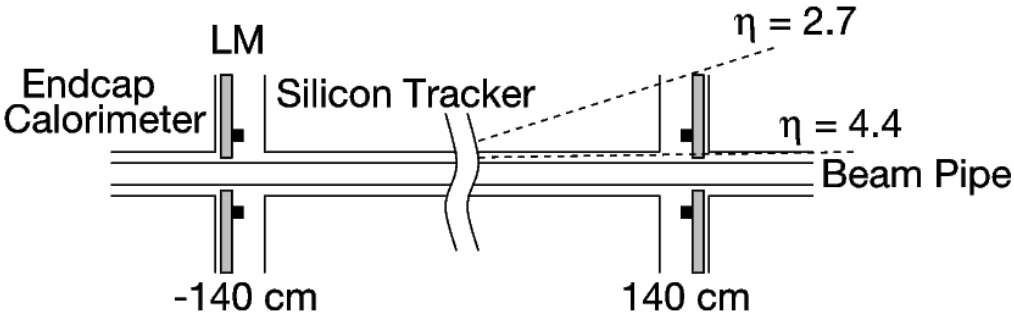

FIGURE 3.8. Position of the luminosity counters (LM) around the beam pipe. The silicon tracker and endcap calorimeter positions are also shown.

luminosity may be estimated as:

$$\mathcal{L} = \frac{-\ln(f_{\text{null}})}{T\sigma_{\text{p}\bar{\text{p}}}}. \tag{3.2}$$

3.5 Detector Operation

A "store" is defined as any period in which there are particles circulating in the Tevatron. As of October 2006, typical instantaneous luminosities at DØ at the start of a store were approximately $15 - 20 \times 10^{31}$ cm^{-2}s^{-1}. Stores are typically kept for 24 hours or so, or until the instantaneous luminosity drops to 2×10^{31} cm^{-2}s^{-1}. Data is collected during stores in sets of "runs". Runs generally last for 2-4 hours, or until 500,000 events have been collected. Breaks are made between runs in order to match trigger prescale settings with the current store luminosity.

The integrated luminosity for a store is found by summing the measured instantaneous luminosities over the store's duration. During periods of stable data-taking, a few pb^{-1} of data are recorded to tape each day. At the end of a store, any remaining beam in the Tevatron is dumped or recycled, and the process for creating a new store begins. The data used in this thesis corresponds to an integrated luminosity of approximately 360 pb^{-}1.

CHAPTER 4
EVENT RECONSTRUCTION

Data from the DØ detector are recorded in the form of digitized pulse height and time information. Event reconstruction programs use this information to form collections of detector hits, times, and energy deposits in each detector subsystem. Identification algorithms are applied to the reconstructed data to associate these hits with the paths traveled by electrons, hadronic jets, and muons. These algorithms reconstruct the trajectories of the particles, and allow for measurement of their four-momenta.

The reconstruction algorithms are applied not just to events from data, but to simulated collision events as well. Event simulators use Monte Carlo statistical techniques to emulate the probabilistic quantum mechanical nature of the particle interactions. This analysis relies heavily on templates generated from such simulations, as discussed in Chapter 6. Thus, it is important that results obtained from data and results from Monte Carlo agree. This chapter outlines the Monte Carlo generators for simulated events, discusses the reconstruction routines applied to real and simulated data, and describes corrections made to bring Monte Carlo results into agreement with data.

4.1 Event Simulation

Parton-parton interactions are simulated with the ALPGEN event simulator [26]. ALPGEN is a Monte Carlo simulator designed to model processes that produce multijet final states. It calculates exact matrix elements for leading-order QCD and electroweak interactions. ALPGEN is used to model decays from $t\bar{t}$ signal events as well as many of the background processes used in this analysis, including Z and WW decays. Parton distribution functions within ALPGEN are modeled with CTEQ5L leading-order parameterizations [27].

Jet fragmentation and radiation within the event is simulated with PYTHIA [28]. Fragmentation is implemented via the Lund string fragmentation model. Extra jets are generated from initial-state and final-state radiation of gluons.

Events generated with ALPGEN and PYTHIA are processed with the DØGSTAR detector simulator [29]. DØGSTAR, or the DØ GEANT Simulator of the Total Apparatus Response, is a wrapper of the GEANT code developed at CERN, and models the energy deposition in the active regions of the detector [30]. A separate detector model, the Parameterised Monte Carlo Simulator (PMCS), is also available. PMCS uses a parameterised approach to simulate the detector response. It is significantly faster than DØGSTAR, but does not provide a complete detector simulation [31].

The detector hits output from DØGSTAR or PMCS are digitized with DØSIM [32]. In addition to this digitization, DØSIM:

- combines simulated events with so-called "minimum bias" events triggered by hits in the luminosity counters;
- adds calorimeter noise and pile-up;
- adds noise and inefficiencies from the central tracking and muon systems.

The resulting output of the Monte Carlo simulations has the same format as the data, and the same reconstruction routines are applied to both. These routines are described in the next section.

4.2 Event Reconstruction

Event reconstruction is performed with the "d0reco" package [33]. Reconstruction begins with the formation of tracks from hits within the central tracker. Electrons and jets are reconstructed from energy clusters within the calorimeter, and may be matched with central tracks to more precisely measure their momentum. Muons are reconstructed from hits within the muon detector, and may likewise be matched to central tracks. The total energy

in the transverse plane (H_T) and the total missing transverse energy ($\not{E}_T$) are then computed by summing the energies of all reconstructed particles.

4.2.1 Central Tracks

Hits within the central tracker are recontructed into particle trajectories, or *tracks*. Two complementary techniques are used to identify track candidates. The first method applies a road-finding algorithm to search for sets of three hits in close proximity in either the SMT or the CFT. The second method forms track stubs from all combinations of two hits within the tracker. A Hough transform is applied to map each stub into (ρ, ϕ_0) space, where ρ is the curvature of the stub (assuming that the stub originated at the geographic center of the detector) and ϕ_0 is the azimuthal angle of the stub at its distance-of-closest-approach (DCA) to the detector center [34]. In a uniform magnetic field with no absorbing material, all stubs from the same trajectory would have identical (ρ, ϕ_0) coordinates. In practice, track candidates are identified from peaks in histogrammed (ρ, ϕ_0) space. A second Hough transform into (z_0, dz/dr) space, where z_0 is the z-coordinate of the stub at its DCA, may also be applied to SMT-based stubs.

Candidate stubs from either track-finding method are passed into a Kalman fitter which searches for additional hits consistent with the original stub [35]. The expected trajectory for each stub is calculated, taking into account the central magnetic field as well as effects from energy loss and multiple interactions within the tracker [36]. A search is then performed for hits near the expected trajectory at each layer of the tracker. Hits that greatly increase the χ^2 of the track are rejected. After the stub is propagated through all detector surfaces, a filter is applied to remove poorly-fit tracks. Tracks with a large χ^2 and tracks with a large number of missed hits are removed from the candidate track list. Tracks that share at least four hits with another track are also removed.

4.2.2 Primary Vertex

Tracks are used to identify the *primary vertex*, the initial $p\bar{p}$ collision point. The primary vertex is initially assumed to be located at the geometric center of the detector. A new vertex V is formed by minimizing the χ^2 from reconstructed all tracks a consistent with the primary vertex hypothesis:

$$\chi^2(V) = \sum_a \frac{(DCA_a^{r\phi})^2}{(\sigma_a^{r\phi})^2} + \sum_a \frac{(DCA_a^z)^2}{(\sigma_a^z)^2}, \tag{4.1}$$

where $DCA_a^{r\phi}$ and DCA_a^z are the distances-of-closest-approach of track a to the detector center along the $r-\phi$ planes and z axis, respectively, and $\sigma_a^{r\phi}$ and σ_a^z are the respective uncertainties in those quantities. Tracks with p_T $\leq$0.5 GeV or with DCA $\geq$ 100σ_{DCA} are not included in this minimization. For tracks with no z information, only the $r-\phi$ contribution to the overall χ^2 is computed. Tracks providing the largest contributions to the χ^2 are removed one by one until the overall χ^2 is less than 10.

Once a preliminary vertex has been found, the χ^2 minimization is repeated, with tighter constraints on the tracks. All tracks with a DCA$\geq$ 3 σ_{DCA} from the new vertex position are excluded from the χ^2 fit. The final vertex is then calculated from the remaining tracks. In the case where more than one vertex is found, the p_T distributions of tracks associated with each vertex are used to define a probability that each track originated at the particular vertex. The vertex with the largest weighted product of track probabilities is identified as the primary vertex [37].

The efficiency of the vertex-finding algorithm is measured by using $Z \rightarrow \mu\mu$ events in data and comparing the calculated primary vertex with the reconstructed dimuon vertex. The vertex is assumed to be correctly identified if the longitudinal distance $\Delta z_{vtx-dimuon} between the prim$ Results from data show that the vertex reconstruction efficiency is 97% for primary vertices within 40 cm of the detector origin [37]. Monte Carlo studies on $t\bar{t}$ events give a vertex resolution of approximately 20 μm in the x and y directions, with slightly worse resolution in the z-direction.

4.2.3 Calorimeter Objects

Both electrons and jets are reconstructed from energy deposited in calorimeter cells. Each cell is assigned a three-momentum with magnitude equal to the measured energy in the cell and direction defined by the vector from the primary vertex to the cell center. Cells are grouped into pseudo-projective towers as described in Chapter 3; each tower measures 0.1×0.1 in $\eta-\phi$ space.

An individual cell is excluded from the tower if the energy deposited within it is less than $2.5\sigma_{cell}$, where σ_{cell} is the mean width due to noise in the cell. A cell is also removed if its energy is less that $4\sigma_{cell}$ and if no neighboring cells have energy greater than $4\sigma_{cell}$. A noise-killing routine removes isolated "hot" cells from the tower, and the four-momenta of the remaining cells are summed to form the tower four-momentum. Any tower with p_T >0.5 GeV is then used as a seed for a pre-clustering algorithm.

Pre-clusters are created from towers with the so-called "Simple Cone Algorithm", which searches for energy in cells within a fixed radius R in $\eta-\phi$ from the tower axis [38]. Pre-clusters are formed from all neighboring towers within R=0.3 of the seed tower. Pre-clusters with p_T >1 GeV are passed to the jet and electron clustering routines.

Jet Reconstruction Jet clustering is performed with a second cone algorithm, in which all cells in a cone of R=0.5 from the initial pre-cluster are combined to form a "proto-jet" [39]. If the separation ΔR between the pre-cluster and proto-jet is small enough (ΔR <0.001), then the proto-jet is taken as a jet candidate. Otherwise, the proto-jet is treated as a new pre-cluster, and the cone algorithm is repeated. Proto-jets with energies less than 8 GeV are rejected from the list of jet candidates.

Jets which share cells may be either merged together or split apart, depending on the amount of energy shared. If the sum of the shared p_T is greater than 50% of the p_T of a single jet, then the two jets are merged into one. Otherwise, the shared cells are split between the jets, with each cell attached to the jet closest to it in $\eta-\phi$ space. Midpoints between jets are also treated as pre-clusters in order to remove sensitivity to soft radiation.

Jet Energy Scale (JES) corrections are made to account for noise and inefficiencies within the calorimeter that may cause the reconstructed jet energy to differ from the original particle energy. Noise from the calorimeter electronics and uranium plates can create an offset $\mathcal{O}$ between the original and reconstructed energies, as can residual energy from previous collisions. Energy loss in uninstrumented portions of the detector and the inefficiencies in the calorimeter response to jets compared to electrons require that an additional correction $\mathcal{R}_{cal}$ be made to the measured energy. A final correction term $\mathcal{R}_{cone}$ accounts for energy from the jet that falls outside the reconstruction cone [40].

The original particle energy is calculated as:

$$E^{particle} = \frac{E^{measured} - \mathcal{O}}{\mathcal{R}_{cal}\mathcal{R}_{cone}}. \tag{4.2}$$

The offset $\mathcal{O}$ is measured from data events collected with minimum-bias triggers. The calorimeter response $\mathcal{R}_{cal}$ is measured from γ+jet data events by requiring that the jet E_T matches that of the photon. $\mathcal{R}_{cone}$ is calculated from jet profiles in γ+jet and dijet data events. The uncertainty in the calculation of jet energies is a significant source of systematic uncertainty in the measurement of the top quark mass, and is discussed in detail in Chapter 8.2.1.

Electron Reconstruction Electrons are identified with a clustering algorithm similar to that described above for jets. Electron clusters are formed from cells within R=0.2 of the initial pre-cluster. The EM fraction, f_{EM}, of each cluster is then calculated:

$$f_{EM} = \frac{E_{EM}}{E_{total}}, \tag{4.3}$$

where E_{total} is the total energy within the cluster and E_{EM} is the energy within the EM cells in the cluster. Clusters with an EM fraction of at least 90% and with a tranverse energy of 1.5 GeV or more are categorized as “loose” electrons.

Electron candidates are also characterized by their isolation fraction, f_{iso}. This is a measure of the difference of the energy deposited in the EM calorimeter in a cone of radius

R=0.2 around an initial precluster and the energy collected in the entire calorimeter within a cone of radius R=0.4:

$$f_{iso} = \frac{E_{total}(R < 0.4) - E_{EM}(R < 0.2)}{E_{EM}(R < 0.2)}. \tag{4.4}$$

High-p_T electrons deposit most of their energy in a region narrower than the R=0.4 cone, and are expected to have a small isolation fraction. Cuts on this variable can thus serve to separate high-momentum electrons from signatures due to noise or jets.

Electrons also produce distinctive shower shapes within the calorimeter. A chi-square "H-matrix" function (χ^2_{Cal7}) is formed from comparisons of energy deposits in each layer of the calorimeter to average distributions from Monte Carlo electrons, as well as comparisons of total energy. Clusters with a χ^2_{Cal7} <50 and f_{iso} <0.15 that also meet the loose electron requirements are categorized as "medium" electrons.

An electron cluster may also be matched to a central track if the separation between the cluster and the track is less than 0.05 in both η and ϕ. An additional identification criterion is introduced through a 7-parameter likelihood variable. This variable separates real electrons from showers created by pions or photoconversions within the detector. The likelihood variable is formed from the following parameters:

- f_{EM}
- χ^2_{Cal}
- E_T/p_T
- $Prob(\chi^2_{spatial})$, the matching probability between the cluster and its central track
- the distance of closest approach in $\eta - \phi$ of the central track to the primary vertex
- the number of tracks in a narrow cone of R=0.05 around the cluster
- the total p_T of all tracks in a cone of R=0.4 around the cluster, excluding the matched central track.

The likelihood is tuned on data, using $Z \rightarrow ee$ decays for signal electrons and di-jet and γ+jet events for fake electrons from QCD multijet processes [41]. Medium electrons with a likelihood greater than 0.85 that are matched to a central track are classified as "tight" electrons.

The electron reconstruction efficiency is measured in data from $Z \rightarrow ee$ decays [42]. Events are selected with two high-p_T tracks with a combined invariant mass between 80 and 100 GeV. One track is required to be matched with a cluster with $f_{EM} > 0.9$, $f_{iso} > 0.15$, and energy of at least 20 GeV. The reconstruction efficiency is calculated by measuring the fraction of events in which the second track is also matched to an electron cluster. The electron reconstruction efficiency is found to be 96.0$\pm$0.4% in the central calorimeter and 93.5$\pm$1.2% in the endcap calorimeter [42].

4.2.4 Muon Reconstruction

Muon reconstruction begins with the formation of straight-line track segments from wire chamber hits in each layer of the muon systems. An attempt is then made to match segments with a confirming scintillator hit in the same muon layer. If confirmed segments exist both inside the toroid (from A-layer muon chambers) and outside the toroid (from B- or C-layer chambers), a local fit is tried between the two segments. A momentum measurement is made from successful fits via the bend angle between the A-layer segments and B-/C-layer segments.

Reconstructed muons are categorized by the variable "nseg", which describes the type of segments found in an event. A muon with an A-layer segment has |nseg|=1, a muon with a B-/C-layer segment has |nseg|=2, and a muon with both segments has |nseg|=3. If the muon segment is also matched to a central track, the nseg value is positive; otherwise, nseg is negative.

Muons are also classified as either "tight", "medium", or "loose", depending on the number of wire and scintillator hits in the muon segments. Tight muons require at least one

TABLE 4.1. Average muon reconstruction efficiencies

Muon Quality	Central Efficiency	Forward Efficiency
Loose	$89.7 \pm 0.3\%$	$92.3 \pm 0.4\%$
Medium	$77.4 \pm 0.3\%$	$85.9 \pm 0.5\%$
Tight	$59.9 \pm 0.5\%$	$81.6 \pm 0.5\%$

A-layer scintillator hit and two A-layer wire hits, as well as at least one scintillator hit and three wire hits in the B and C layers. The fit between the A-layer and B-/C-layer segments must also converge. A medium muon requires only two B-/C-layer wire hits, but also requires a match to a central track. A muon may also be classified as medium if it meets only the A-layer or B-/C-layer conditions and is located in octant 5 or 6, where muon detector coverage is reduced. Loose muons are formed by further relaxing the medium muon requirements, and generally require only one reconstructed segment [43].

The efficiency for identifying muons is measured using Z decays, in much the same way as for electrons. Candidate $Z \rightarrow \mu\mu$ events with two high-p_T tracks are selected from data. The first track is required to have a p_T >30 GeV and to be matched with a medium muon. The A-layer scintillator time of this muon is required to be less than 10 ns in order to reject cosmic ray muons. The second track is required to have at least eight CFT hits as well as a good central track χ^2. Both tracks must have a DCA less than 0.16 cm, and the two tracks must not be collinear. Efficiencies are then calculated from the fraction of events in which the second track matches a muon segment. A summary of average tight, medium, and loose efficiencies for the central and forward regions of the muon system is given in Table 4.1. The efficiency in the central region is systematically lower than the forward; this is primarily due to the incomplete detector coverage in central octants 5 and 6.

4.2.5 Missing Transverse Energy

Neutrinos are not detected directly within the detector, and instead manifest themselves as "missing" transverse energy $\not{E}_T$ – an imbalance in the total transverse momentum. This quantity is calculated from the vector sum of all energy clusters in the calorimeter. Unclustered cells are also included if they pass the energy selection cuts outlined in Section 4.2.3. The $\not{E}_T$ is adjusted for JES corrections made to jets within the event. It is also adjusted for the presence of any muon, first by removing the muon's minimum-ionizing calorimeter signature from the $\not{E}_T$ calculation, then by subtracting the muon's measured momentum.

4.3 Resolutions and Monte Carlo Corrections

The calorimeter resolution is measured in terms of particle energy:

$$\frac{\sigma_E}{E} = C \oplus \frac{S}{\sqrt{E}} \oplus \frac{N}{E}, \tag{4.5}$$

where C comes from calorimeter calibration errors, S is due to energy sampling, and N is a noise term. These terms are measured separately for jets and electrons. For electrons, the constant term is measured from $Z \to ee$ events, and found to be 0.0373 ± 0.0028 in the central calorimeter and 0.0203 ± 0.0059 in the end caps [44]. Since the calorimeter is unchanged from Run I, the sampling terms are taken to be the same as their Run I values – $0.15 \pm 0.01 GeV^{1/2}$ in the central calorimeter, and $0.21 \pm 0.01 GeV^{1/2}$ in the endcaps. The Run I noise term value of 0.29 ± 0.03 is also used. The overall electron resolution is thus dominated by by the calibration term. The jet resolution parameters are measured from imbalances in γ+jet and dijet events, and are given in Table 4.2 [45].

Calorimeter resolutions in Monte Carlo are seen to disagree with data resolutions. To correct for this disagreement, an additional smearing is performed on Monte Carlo jets and electrons. A scale factor and offset is applied to generated electron energies E_{gen}:

$$E_{new} = \alpha E_{gen} + \beta. \tag{4.6}$$

TABLE 4.2. Jet energy resolution parameters from data

	$\|\eta\| < 0.5$	$0.5 < \|\eta\| < 1.0$	$1.0 < \|\eta\| < 1.5$	$1.5 < \|\eta\| < 2.0$
C	5.045 ± 0.833	0.000 ± 21.77	2.236 ± 3.153	6.424 ± 0.680
S ($\mathrm{GeV}^{1/2}$)	0.753 ± 0.150	1.197 ± 0.048	0.924 ± 0.216	0.000 ± 7.094
N (GeV)	0.089 ± 0.007	0.087 ± 0.006	0.135 ± 0.011	0.097 ± 0.008

TABLE 4.3. Electron smearing constants in the central (CC) and endcap (EC) calorimeter

	α	β (GeV)
CC	1.0060 ± 0.0017	0.0953 ± 0.0793
EC	0.9991 ± 0.0036	0.7953 ± 0.2943

The scaled energy E_{new} is then smeared by a gaussian of unit width ($\zeta(1)$) multiplied by the calorimeter electron resolution:

$$E_{smear} = E_{new} + \sigma_{E_{new}} \zeta(1). \tag{4.7}$$

The constants α and β in Equation 4.6 are chosen so that the width of $Z \rightarrow ee$ peaks in data and Monte Carlo agree [44]. The measured values of these constants are given in Table 4.3.

Jet resolutions in Monte Carlo are also seen to differ from those in data (see Table 4.4). In the case where the data resolution is worse than the Monte Carlo resolution additional smearing is applied to Monte Carlo jets:

$$\sigma = \sqrt{\sigma_{data}^2 - \sigma_{MC}^2}. \tag{4.8}$$

A correction factor of 1.034 is applied to all jets to account for an observed shift in energy between data and Monte Carlo jets [46].

Muon resolution is parameterized in terms of curvature, $1/p_T$:

$$\sigma_{1/p_T} = A \oplus \frac{B}{p_T}. \tag{4.9}$$

TABLE 4.4. Jet energy resolution parameters from Monte Carlo

	$\|\eta\| < 0.5$	$0.5 < \|\eta\| < 1.0$	$1.0 < \|\eta\| < 1.5$	$1.5 < \|\eta\| < 2.0$
C	4.263 ± 0.585	4.607 ± 0.536	3.078 ± 1.693	4.828 ± 0.440
S ($GeV^{1/2}$)	0.658 ± 0.086	0.622 ± 0.098	0.816 ± 0.190	0.000 ± 0.595
N (GeV)	0.044 ± 0.005	0.058 ± 0.004	0.073 ± 0.013	0.074 ± 0.009

TABLE 4.5. Muon Monte Carlo Resolutions

Intrinsic resolution parameters		
	$\|\eta\| < 1.0$	$1.0 < \|\eta\| < 2.0$
A	0.00152	0.00226
B	0.0279	0.0479
Data-Monte Carlo correction parameters		
	$\|\eta\| < 1.0$	$1.0 < \|\eta\| < 2.0$
α	0.993590	0.973077
β	0.0236842	0.00365385

The resolution values A and B measured with Monte Carlo muons are listed in Table 4.5. An additional smearing is applied to Monte Carlo events to compensate for observed resolution differences from data:

$$\frac{1}{p_T^{new}} = \frac{1}{\alpha p_T} + \zeta(\beta), \tag{4.10}$$

where $\zeta(\beta)$ is a Gaussian of width β. The measured values of α and β are also given in Table 4.5.

CHAPTER 5
EVENT SELECTION

Candidate $t\bar{t}$ events are chosen from data collected between June 2002 and August 2004, a data set comprising nearly one trillion events. Events are reconstructed with d0reco versions p14.03-p14.06, and are passed on to the TopAnalyze package [47]. TopAnalyze groups reconstructed objects in each event according to the identification criteria described in the previous chapter, applies energy corrections, and re-formats the data for use within the ROOT analysis framework [48]. Events are grouped into "DIMU", "DIEM", and "EMU" subsamples (or "skims"), depending on the number and type of leptons in the events. Events in each decay channel are selected only if the appropriate dilepton trigger for that channel fired. Events must also contain the signature end products from $t\bar{t} \rightarrow$ dilepton decays: two high-p_T leptons, two high-p_T jets, and significant missing transverse energy. Channel-dependent topological cuts are applied to reduce backgrounds in each channel.

Event selection is designed to select top quark decays and to suppress background events that may mimic the top dilepton signature. Such backgrounds can come from physical processes with similar decay products or from events which "fake" such signatures due to instrumentation uncertainties. Physical background processes include WW and WZ production and $Z \rightarrow \tau\tau$ decays. Instrumental fakes arise from $Z \rightarrow \ell\ell$ decays in which the calorimeter records large amounts of $\not\!\!E_T$, and from QCD multijet events with mis-identified electrons or isolated muons. The event selection criteria used in each dilepton channel are outlined below. The optimization of these criteria is discussed more fully in [49] and [50].

5.1 Triggering on Dileptons

An event is considered for analysis only if it causes a dilepton trigger to fire. Level 1 muon triggers are formed based on the number of hits within the muon detectors, while Level 1

electron triggers fire if a calorimeter tower greater than some threshold is found. Level 2 and Level 3 triggers provide partial reconstruction of leptons, and may reject leptons with low energy or without a central track match.

As both the number of available triggers (or "trigger list") and the algorithms for forming individual triggers evolved over time, the conditions for triggering on a $t\bar{t}$ event are not fixed. In general, all muon events must pass a Level 1 muon "tight scintillator" trigger; that is, a trigger that requires scintillator hits both inside and outside the toroid. In the dimuon channel, two such tight triggers must be present, while in the electron-muon channel, this trigger must be paired with a Level 1 electron trigger. The Level 1 electron trigger requires an EM calorimeter tower above a certain threshold energy, where the value of the threshold is dependent upon the trigger list used to collect the event data. Level 2 muon triggers require at least one medium reconstructed muon, while Level 3 electron triggers require at least two reconstructed loose electrons. Additional Level 3 muon and Level 2 electron triggers are used in some trigger list versions. A full description of all triggers used in this analysis is given in Appendix A

Trigger efficiencies in each channel are computed using v01-04-04 of the top_trigger package [51]. Efficiencies are calculated based on efficiences of single-lepton triggers as measured on data. The efficiencies are generally measured with a "tag and probe" method on candidate Z decays; a full description of these calculations is provided in [51]. The overall trigger efficiency in each decay channel is calculated by weighting each trigger used in that channel by its contribution to the total recorded luminosity. The average efficiencies for the dilepton channels are given in Table 5.1 [49][50].

Luminosity is calculated with version v00-06-03 of the top_dq package, along with the fall2004-pass2-04 version of top_dq_data [52]. These packages also remove runs in which detector performance in compromised, as determined by various subdetector experts. Individual blocks of luminosity that have corrupted readout or are otherwise marked as "bad" by the luminosity group are also removed. Runs marked as bad by one subdetector may be usable by other subdetectors; thus the total luminosities for the three decays channels

TABLE 5.1. Average dilepton trigger efficiencies

Channel	Efficiency (%)
$\mu\mu$	92.5±0.4(stat.)
ee	94.0±0.4(stat.)
$e\mu$	90.1±0.2(stat.)

need not be identical. As shown in Table 5.2, though, the luminosities differ by less than 25 pb^{-1} between channels, with all channels recording at least 360 pb^{-1} of data.

TABLE 5.2. Total recorded luminosity versus trigger list version

Trigger List Version	$\int \mathcal{L}\, dt$ (pb^{-1})		
	$\mu\mu$	ee	$e\mu$
v8	22.02	20.08	18.25
v9	21.22	30.75	21.26
v10	7.99	15.48	15.46
v11	57.26	57.38	57.26
v12	209.83	217.41	209.82
v13	44.31	42.97	45.82
total	362.6	384.1	367.7

5.2 Common Event Selection Criteria

The three dilepton channels share a large number of event selection criteria. Each requires that an event is marked as "good" by the calorimeter experts, and must contain at least two jets with reconstructed p_T >20 GeV. Each jet must also satisfy the following conditions:

- $|\eta_{jet}| < 2.5$. This ensures that the jet is within the fiducial region of the calorimeter.
- $0.05 < f_{EM} < 0.95$, where f_{EM} is the fraction of the total jet energy found within the EM calorimeter. The cut at 95% reduces signals from electrons, while the cut at 5% removes jets created from noise in the hadronic calorimeter.

- $f_{CH} < 0.4$, where f_{CH} is the fraction of jet energy in the coarse hadronic layer of the calorimeter. Since jets are expected to deposit most of their energy in the inner layers of the calorimeter, cutting on this variable removes jets produced from noise in the outer layers

- "hot cell ratio"< 10. This is the ratio of the highest-energy cell to the cell with the next-highest energy. This cut removes jets formed from individual hot cells.

- $n_{tow}^{90} > 1$, where n_{tow}^{90} is the number of towers containing 90% of the total jet energy. Requiring this energy to be spread across at least two towers reduces noise from individual hot towers.

An event must also contain a "well-reconstructed" primary vertex, meaning that the vertex contains at least three tracks and is located longitudinally within the active region of the SMT ($|z_{PV}| < 60$ cm). Two leptons with $p_T > 15$ GeV must also be found within the event. Although the lepton flavor and quality can differ between channels, each lepton must have a reconstructed initial z-position within 1 cm of the primary vertex.

5.3 Channel-Dependent Selection Criteria

5.3.1 Dimuon Events

The dimuon decay channel requires two opposite-sign muons with $p_T > 15$ GeV. Events with a reconstructed tight electron are rejected, in order to keep the dimuon event selection orthogonal to that of the dielectron and electron-muon channels. Each muon must have medium quality and *nseg*=+3, with a track-match $\chi^2 < 4$. In order to distinguish muons produced in collisions from cosmic-ray muons, the times of the A-layer scintillator hits associated with each muon must be less than 10 ns from the time of the $p\bar{p}$ collision. Muons must also have a DCA to the primary vertex less than $3\sigma_{DCA}$. A dimuon trigger must also have fired in the event.

Muons produced via W decays are expected to be isolated from any jets in the event. Isolation is enforced through the use of the *Halo(0.1,0.4)* and *TrkCone(0.5)* variables. *Halo(0.1,0.4)* is defined as the total calorimeter energy in a hollow $\eta - \phi$ cone of inner radius $\Delta R = 0.1$ and outer radius $\Delta R = 0.4$ around the muon, while *TrkCone(0.5)* is the total p_T of all tracks in a cone $\Delta R = 0.5$ around the muon. The ratios of each of these two variables to the muon p_T, defined as *rat11* and *rattrk*, respectively, must both be less than 0.12 for the muon to be considered isolated.

High-p_T muon pairs are produced not just from $t\bar{t}$ decays, but Z decays as well. Opposite-signed muon pairs may be produced directly from Z's, or indirectly via $Z \rightarrow \tau\tau$ decays in which each τ decays to a muon. Background muons from the first process are reduced by assuming each event is a $Z \rightarrow \mu\mu$ decay, and then applying a χ^2 to the event based on the momentum of the muons. The formulation of this χ^2 is discussed in [53]. Events with $\chi^2 < 2$ are considered to be Z decays and are rejected from the analysis.

Backgrounds from muons produced either directly or indirectly from Z's are also reduced by applying a cut on the total $\not{E}_T$ in the event. This is applied as a contour cut, with the minimum required $\not{E}_T$ dependent on the angle $\Delta\phi$ between the leading muon and the $\not{E}_T$. The minimum $\not{E}_T$ requirement is 35 GeV. This value increases as the direction $\not{E}_T$ and the leading muon become more collinear (Figure 5.1). Since significant $\not{E}_T$ can appear in an event due to muons with severely misreconstructed momentum, events with a $\Delta\phi$ of more than 175° are rejected. A list of event selection efficiency for each of the cuts described above is given in Table 5.3. The total $t\bar{t}$ event selection efficiency is calculated from Monte Carlo samples, and is found to be $6.4 \pm 0.2\%$.

5.3.2 Dielectron Events

The dielectron decay channel selection requirements are similar to those in the dimuon channel. Two reconstructed tight 15 GeV electrons of opposite sign must be present in the event. A dielectron trigger must also have fired. $Z \rightarrow ee$ backgrounds are reduced

TABLE 5.3. Dimuon event selection effficiences

Cut	Efficiency
Two track-matched muons, oppositely-charged, with $p_T > 15$ GeV	0.301 ± 0.004
Veto on tight electrons	0.998 ± 0.001
Dimon Trigger Efficiency	0.925 ± 0.004
Two jets, with $p_T > 20$ GeV	0.731 ± 0.007
Good primary vertex within SMT active region	0.975 ± 0.002
Muons within 1 cm of primary vertex, with DCA $< 3\sigma_{DCA}$	0.829 ± 0.007
Both muons isolated; rattrk<0.12, rat11<0.12	0.754 ± 0.009
Z χ^2 fit < 2	0.806 ± 0.009
$\not{E}_T$ contour cut	0.636 ± 0.012
Total	0.064 ± 0.002

by applying a cut on the invariant mass M_{ee} of the two electrons. Events in which the dielectron invariant mass is near to the mass of the Z (80 GeV $\leq M_{ee} \leq$ 100 GeV) are rejected. A cut on $\not{E}_T$ is placed on surviving events to further reject backgrounds. Only events with $M_{ee} < 80 (> 100)$ GeV and $\not{E}_T > 40 (> 35)$ GeV are kept for analysis.

Jets and leptons from top events are expected to be distributed in a more spherically-symmetric manner than jets and leptons from background processes. Backgrounds can thus be reduced with a cut on *sphericity*, defined as:

$$\mathcal{S} = \frac{1}{2}(Q_1 + Q_2),$$

where Q_1 and Q_2 are the two leading eigenvalues of the momentum tensor formed by all jets and leptons in an event. Events with $\mathcal{S} \leq$0.15 are rejected. This cut is particularly effective in reducing Z$\rightarrow \tau\tau \rightarrow ee$ backgrounds.

A list of all selection cuts for the dielectron channel appears in Table 5.4, along with

the efficiency of each cut. The total efficiency for selecting $t\bar{t} \rightarrow ee$ events is measured in Monte Carlo to be 8.2±0.2%.

TABLE 5.4. Dielectron Event Selection Effficiences

Cut	Efficiency
Two track-matched electrons, oppositely-charged, with $p_T > 15$ GeV and likelihood > 0.85	0.219
Dielectron Trigger Efficiency	0.940
Two jets, with $p_T > 20$ GeV	0.695
Good primary vertex within SMT active region	0.975
Electrons within 1 cm of primary vertex,	1.000
M_{ee} cut	0.855
$\not{E}_T$ cut	0.762
$\mathcal{S} > 0.15$	0.936
Total	**0.082**

5.3.3 Electron-muon Events

Event selection in the electron-muon channel requires one medium muon and one tight electron. The electron-muon pair must be oppositely charged, and must cause at least one $e\mu$ trigger to fire. Muon bremsstrahlung background is reduced by requiring the electron not to share a track with any muons within the event. Events with two or more tight electrons are rejected in order to provide orthogonality with the dielectron channel.

Because the electron-muon channel is not contaminated by direct $Z \rightarrow \ell\ell$ decays, its selection criteria are somewhat looser than in the ee and $\mu\mu$ channels. The likelihood cut on the tight electron is reduced from 0.85 to 0.25. As will be shown in Section 5.4, this increases top selection efficiency while still providing an effective cut on QCD fake back-

grounds. Each event must contain at least 25 GeV of $\not\!\!E_T$. A cut is also placed on H_T^ℓ, the total transverse momentum of the leading lepton and two leading jets:

$$H_T^\ell = \sum p_T(\text{2 leading jets}) + p_T(\text{leading lepton}) > 140 \text{ GeV}.$$

The total efficiency of all electron-muon selection cuts on $t\bar{t}$ decays is found to be $10.8 \pm 0.2\%$. The efficiency of each cut is given in Table 5.5.

TABLE 5.5. Electron-Muon Event Selection Effficiences

Cut	Efficiency
One Tight track-matched electron, $p_T > 15$ GeV, likelihood>0.25, containing no muon track	0.494
One medium isolated muon, $p_T > 15$ GeV, with opposite charge of electron	0.469
Electron-Muon Trigger Efficiency	0.903
Two jets, with $p_T > 20$ GeV	0.699
Good primary vertex within SMT active region	0.960
Leptons within 1 cm of primary vertex	1.000
$\not\!\!E_T > 25$ GeV	0.892
$H_T^\ell > 140$ GeV	0.864
Total	**0.108**

5.4 Event Yields

The expected number of top events in each dilepton channel, $N_{top}^{\ell\ell}$, is given by:

$$N_{top}^{\ell\ell} = \varepsilon^{\ell\ell}\sigma_{top} \times BR(t\bar{t} \to \ell\ell) \times \int \mathcal{L}\, dt, \tag{5.1}$$

where $\varepsilon^{\ell\ell}$ is the selection efficiency for the channel, $BR(t\bar{t} \rightarrow \ell\ell)$ is the branching ratio for the channel, and σ_{top} is the Run I $t\bar{t}$ cross section. Background yields are calculated in a similar manner, by multiplying their cross sections by their selection efficiencies and the total integrated luminosity. In the case of backgrounds without known cross sections, yields are estimated directly from data.

5.4.1 Z/γ Decays

The dominant backgrounds in the $\mu\mu$ and ee channels come from $Z/\gamma \rightarrow \mu\mu$ and $Z/\gamma \rightarrow ee$ events, respectively. In principle, such decays should be eliminated by the $\not{E}_T$ cuts in those channels. However, noisy calorimeter cells or towers or muons with poorly reconstructed momentum can lead to substantial "fake" $\not{E}_T$ in an event. Such events are modeled in Monte Carlo with a sample of Alpgen $Z \rightarrow \ell\ell + 2$ jet decays. Yields for dileptons with masses in the range 75 GeV $< M_{\ell\ell} <$ 105 GeV are compared between Monte Carlo and data. A correction factor of 1.02 is applied to the Monte Carlo cross section to obtain agreement with data. The expected number of background events is then calculated by multiplying the Monte Carlo cross section by the fraction of Monte Carlo events that pass the $t\bar{t}$ selection cuts. Backgrounds from $Z/\gamma \rightarrow \tau\tau$ decays are estimated in a similar manner for all decay channels.

5.4.2 WW and WZ Decays

WW+2 jet and WZ+2 jet backgrounds are also estimated from Alpgen Monte Carlo samples. The cross sections in these samples come from leading-order theoretical calculations. Unfortunately, NLO calculations for these backgrounds do not exist. However, NLO calculations for WW and WZ decay cross sections (without extra jets) do exist. and are found to be 35% and 38% greater than the respective leading-order calculations. The two jet background yields are thus scaled up by these amounts. Systematic errors equal to these increases are assigned to each background.

5.4.3 QCD Fakes

Significant backgrounds are also produced from QCD events in which a jet fakes an electron signature. A fake muon signature may be produced by semileptonic heavy flavour decays in which the muon appears isolated from the heavy jet. No Monte Carlo exists that models such processes. The probability for an event to contain either a fake electron or a fake isolated muon must be estimated from data.

Fake muons in the dimuon channel are estimated from dimuon data in which the leading muon is required to be non-isolated. All other event selection cuts are applied as described in Section 5.3.1. The isolation efficiency is then measured on the second muon in order to estimate the muon fake rate, f_μ. The isolation efficiency on signal events, ε_{sig}, may be computed from $t\bar{t}$ Monte Carlo. The fake and signal isolation efficiencies are found to be $2.2 \pm 0.6\%$ and $86.8 \pm 0.5\%$, respectively. The fake background N_{fake} can then be calculated by measuring the number of events with one tight muon (N_{tl}) and the number of events with two tight muons (N_{tt}):

$$N_{tl} = N_{top+Z} + N_{fake} \tag{5.2}$$

$$N_{tt} = \varepsilon_{sig} N_{top+Z} + f_\mu N_{fake} \tag{5.3}$$

A total of 10 events are found in data for the N_{tl} sample, while two events contain two tight muons. This leads to a fake muon background yield of 0.13 ± 0.03 events.

The fake electron rate, f_e, is calculated from a sample of loose dielectrons in data. Events with $\not{E}_T < 15$ GeV and with 75 GeV$< M_{ee} <$105 GeV are excluded to remove W and Z backgrounds. Remaining electrons are assumed to be produced from QCD events. The fake rate is taken as the fraction of electrons that pass tight selection cuts, and is found to be $0.16 \pm 0.01\%$ in the central calorimeter, and $0.26 \pm 0.02\%$ in the end caps. The overall fake yield is determined in much the same way as for dimuon events, by comparing data events containing one tight and one loose electron with events containing two loose electrons. An estimated fake background of 0.09 ± 0.03 events is found from this procedure.

TABLE 5.6. Expected Yields in Dilepton Channels

Source	Channel		
	$e\mu$	ee	$\mu\mu$
$t\bar{t}$ signal	$9.80^{+1.14}_{-1.32}$	$3.48^{+}0.35_{-0.40}$	2.54 ± 0.07
$Z \to \tau\tau$	0.73 ± 0.16	$0.30^{+0.10}_{-0.14}$	0.07 ± 0.02
$Z \to ee$	-	0.45 ± 0.15	-
$Z \to \mu\mu$	-	-	0.95 ± 0.14
WW/WZ	0.74 ± 0.27	$0.20^{+0.11}_{-0.15}$	0.20 ± 0.03
QCD fakes	0.32 ± 0.29	0.09 ± 0.03	0.13 ± 0.03
Total Background	1.79 ± 0.43	$1.04^{+0.21}_{-0.26}$	1.35 ± 0.15
Observed Yield	**15**	**5**	**2**

Fake yields in the electron-muon channel are calculated in a similar manner to the dimuon and dielectron channels. Fake events can occur either from fake electrons or fake muons. The electron likelihood cut of 0.25 is sufficient to greatly reduce the fake electron background, as shown in Figure 5.2. The fake muon yield is found to be nearly negligible in this channel.

The expected signal and background yields for this analysis are shown in Table 5.6. The observed number of events in the dimuon, dielectron, and electron-muon channel are 2, 5, and 15, respectively.

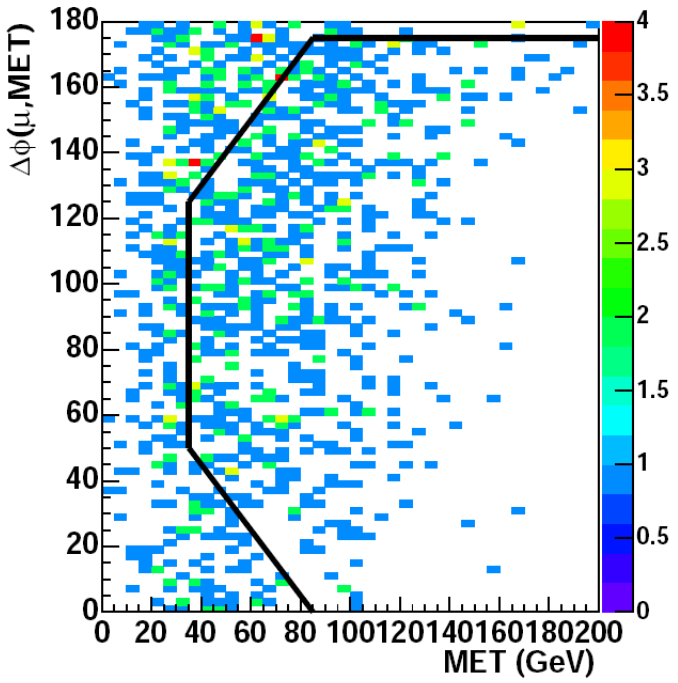

(a) $t\bar{t}$

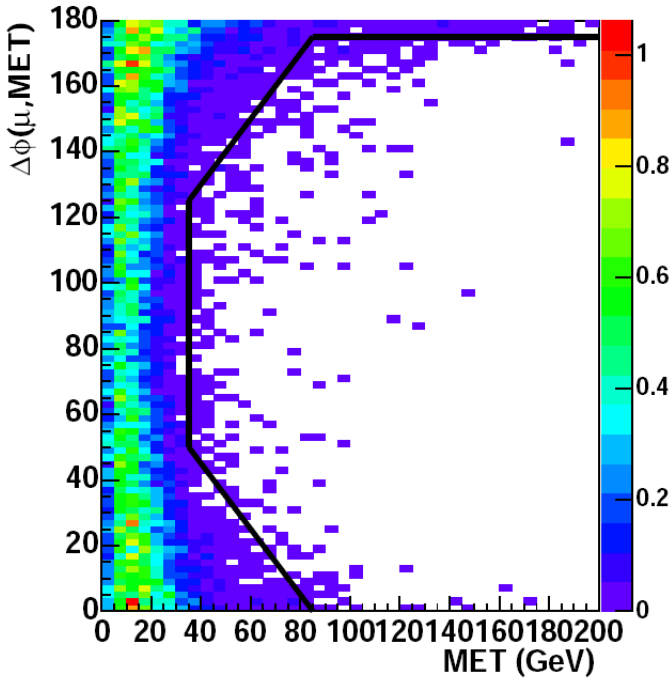

(b) Z/γ,WW

FIGURE 5.1. Contour cut on $\not{E}_T$-$\Delta\phi(\not{E}_T,\mu)$ for (a) $t\bar{t}$ signal and (b) Z/γ and WW events. The dark solid line shows the contour cut.

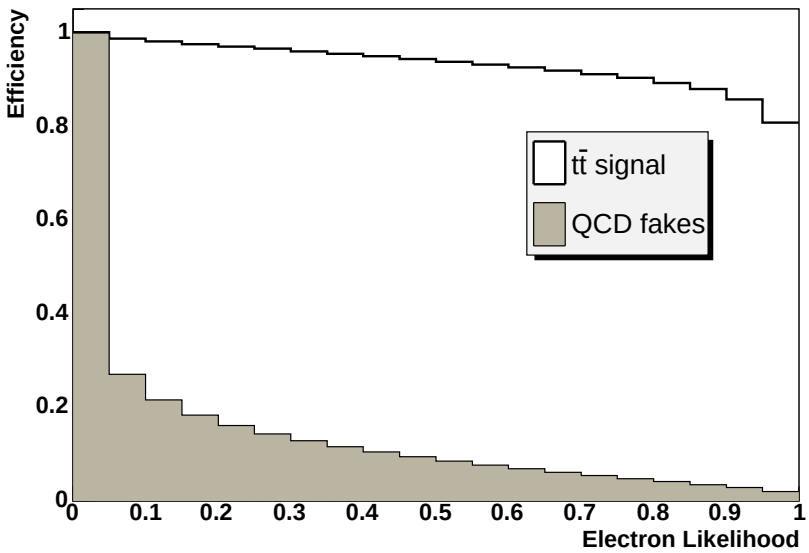

FIGURE 5.2. Efficiency vs. electron likelihood for $t\bar{t} \rightarrow e\mu$ signal and QCD fake events.

CHAPTER 6
MASS TEMPLATE GENERATION

Once candidate $t\bar{t}$ events have been selected, the mass of the top quark must be determined from the resulting decay products in the event. If the energy and momentum of all of the products were known, then the top mass could be reconstructed directly from these observables. Unfortunately, the presence of two neutrinos within the decay limits one's knowledge of the event kinematics. This chapter describes the so-called "neutrino weighting" method, a procedure developed during Run I [54] to evaluate the top mass in the absence of sufficient kinematic event constraints.

6.1 Neutrino Weighting

A schematic of a $t\bar{t} \rightarrow$ dilepton decay is shown in Figure 6.1. A total of six decay particles are produced from the $t\bar{t}$ pair, with each particle described by an energy-momentum four-vector. Thus, the decay is characterized by a set of 24 kinematic parameters. The masses of all the decay particles are known, leaving a total of 18 independent parameters in the event. Twelve of these parameters are measured directly from momentum of the reconstructed leading two jets and two charged leptons within the event. The neutrinos in the event are not measured directly. However, the vector sums of their momentum in the x and y directions are measured as $\not{E}_x$ and $\not{E}_y$. These values provide two additional kinematic constraints. Another two constraints are produced from energy conservation in the W decays:

$$m_{W^+}^2 = (E_{\bar{\ell}} + E_\nu)^2 - (\vec{p}_{\bar{\ell}} + \vec{p}_\nu)^2 \tag{6.1}$$

$$m_{W^-}^2 = (E_\ell + E_{\bar{\nu}})^2 - (\vec{p}_\ell + \vec{p}_{\bar{\nu}})^2. \tag{6.2}$$

A final constraint comes from requiring that the mass of the top and anti-top be equal.

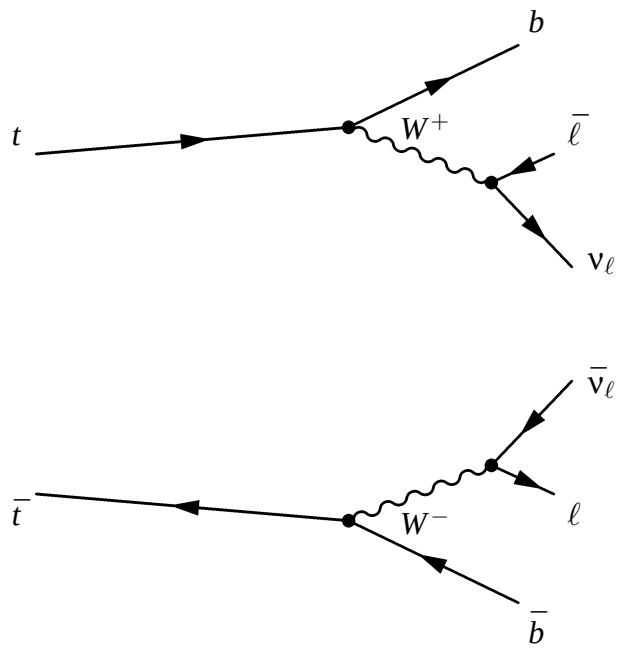

FIGURE 6.1. A $t\bar{t} \rightarrow$ dilepton decay.

Thus, event measurements yield a total of 17 constraints on the system, one short of the number needed to completely describe the kinematics of the system. An extra constraint is applied by simply assuming a value of the top mass. Additionally, the measured $\not{E}_x$ and $\not{E}_y$ are ignored, and a rapidity η_i is assumed for each neutrino i. This approach removes two constraints, but applies three more, making the system solvable. The solution for the momentum of each neutrino is quadratic, so that there can be up to four real solutions for eah choice of top mass and neutrino rapidities. These solutions are derived in Appendix B.

These solutions are derived by assuming the correct parentage for each of the b quarks within the event. However, in data events, it is not known which jet came from a top quark and which came from an anti-top. Thus, solutions are calculated for both of the permutations of b quark parentage, using the leading two jets in the event. This doubles the number of possible solutions per event.

Once solutions are found for an assumed m_{top}, they are assigned a weight $\tilde{w}$ based on how well the calculated neutrino momenta $\vec{p}_i$ agree with the observed MET (hence the

name “neutrino weighting”). The weight is defined as:

$$\tilde{w}(m_{top},\eta_1,\eta_2) = \sum_{solutions}\prod_{j=x,y} exp(-\frac{1}{2}\frac{(\not{E}_j - p_{1_j} - p_{2_j})^2}{\sigma^2_{\not{E}_j}}). \tag{6.3}$$

Here, $\sigma^2_{\not{E}_x}$ and $\sigma^2_{\not{E}_y}$ are the $\not{E}_x$ and $\not{E}_y$ resolutions as measured using $Z+2$ jets data, and are found to be:

$$\sigma^2_{\not{E}_x} = 6.85\text{ GeV} + 0.035 \times \sum E_T^{unclus} \tag{6.4}$$

$$\sigma^2_{\not{E}_y} = 7.43\text{ GeV} + 0.021 \times \sum E_T^{unclus}, \tag{6.5}$$

where $\sum E_T^{unclus}$ is the scalar sum of the unclustered calorimeter energy within an event [55].

It is unlikely that a single randomly chosen set of values of top quark mass and neutrino rapidities will produce a real solution to the kinematic equations discussed above. Thus, the solution method is repeated for a range of assumed top masses, starting at 80 GeV and increasing in 2 GeV increments to 330 GeV. At each mass point, solutions are attempted on multiple choices of neutrino rapidity pair values.

Monte Carlo parton-level studies show that rapidity distributions of neutrinos from top quarks are well described by a gaussian distribution, as shown in Figure 6.2. Furthermore, Figure 6.3 illustrates that the width of this distribution decreases slightly with increasing top mass. The width is parameterized by top mass according to:

$$\sigma_\nu(m_{top}) = 1.485 - (4.618 \times 10^{-3})m_{top} + (1.038 \times 10^{-5})m_{top}^2. \tag{6.6}$$

This dependence allows for judicious choices of neutrino rapidities for use in the neutrino weighting method. At each assumed value of m_{top}, a gaussian distribution $g(\eta')$ is defined, with width given by Equation 6.6. The gaussian is divided into ten sections of equal areas, and rapidities η at the points $\int_{-\infty}^{\eta} g(\eta')d\eta' = 0.05, 0.15, ...0.95$ are calculated. Solutions are attempted for each neutrino at each of these rapidity points. This produces a

solution for 100 rapidity pairs, arranged in a 10×10 grid in (η_1, η_2) rapidity space. Weights from each solution are added together, producing an overall weight w for a given top quark mass:

$$w(m_{top}) = \sum_{\eta_1} \sum_{\eta_2} \tilde{w}(m_{top}, \eta_1, \eta_2) \tag{6.7}$$

6.2 Monte Carlo Tests

If the rapidities of the neutrinos from a top decay were somehow known *a priori* and the momentum of each lepton and b quark were measured exactly, the neutrino weighting method guarantees that the event weight w would be non-zero at the mass of the top quark. However, the method cannot guarantee that no solutions exist for other mass values. An "incorrect" assumption about neutrino rapidity or jet/lepton combinations may still be kinematically consistent with a top decay. Additionally, finite detector resolutions and the hadronization of b quarks into jets prohibit measuring the parton momenta exactly. Such mismeasurements can dramatically change an event weight for a given m_{top}. These effects must be studied in Monte Carlo events in order to determine the usefulness of the neutrino weighting algorithm.

6.2.1 Parton-level Tests

Event weights are first calculated for events selected from Monte Carlo $t\bar{t}$ samples using parton-level information for all final-state particles. A total of nineteen Monte Carlo $t\bar{t}$ samples exist, with each sample corresponding to a different assumed top quark mass. Event weights are generated for top quark masses ranging in 5-GeV increments from 10 GeV to 210 GeV. Weights are also generated for assumed mass of 120, 130, 220, and 230 GeV.

In the parton-level tests, all b quarks used to generate weights are required to be identified with a top quark parent. All leptons and neutrinos must come from $t \to W$ decays. Missing transverse energy is calculated directly from the combined momentum of the neutrinos.

Weights are calculated for each of the nineteen Monte Carlo $t\bar{t}$ samples. Event weight distributions for individual events from a given sample tend to peak sharply near the assumed mass for the sample, as in Figure 6.4(a). This is not always the case, as some events contain peaks far from the assumed mass (see Figure 6.4(b)). However, Figures 6.5 and 6.6 illustrate that, when event weights are summed over a large number of events, the peak of the overall distribution nearly matches the input mass. These figures represent between 300 and 1300 events, depending on the Monte Carlo sample used.

6.2.2 Reconstructed Particle Tests

The parton-level tests show that event weights generated from parton-level information from a large number of Monte Carlo events can produce information about the mass of the top quarks used in the Monte Carlo. These tests are repeated using information from reconstructed particles from the Monte Carlo. Particles are reconstructed with the event generation and detector simulation packages described in Chapter 4.1 of this document. This reconstructed information mimics data recorded in the detector during actual collisions.

In these tests, the momenta of the b quarks are replaced by the momenta of the two largest reconstructed jets. Parton-level information about particle parentage is lost, so jets and leptons are no longer required to have been created from top quarks. Missing transverse energy is computed from energy in calorimeter cells and from reconstructed muons rather than from the neutrinos. These effects cause the loss of information about the top decay, and the event weight distributions broaden significantly compared to those in Figure 6.5, as Figure 6.7 demonstrates. The peaks in the distributions may also be significantly shifted from the input mass value, as shown in Figure 6.8.

The particle-level test assumes perfect reconstruction of all particles. However, as indicated in Chapter 4, the finite detector resolution creates uncertainties in the measurements of particle momenta. To compensate for this, the momentum of each jet and lepton is

randomly smeared according to its resolution. Such smearing can dramatically alter the shape of the event weight distribution for event, since smeared events may have solutions unavailable to unsmeared events, and vice versa. Events are thus repeatedly smeared until the shape of the event weight distribution stabilizes. This is shown in Figure 6.9. It is found that smearing each event 150 times is sufficient to produce a stable distribution shape. These smearings further broaden the width of the event weight distributions. Event weight distributions from smeared events also show greater disagreement between the distribution peaks and input top quark masses than was seen in either the parton-level or unsmeared particle-level tests (Figure 6.10).

6.3 Template Generation

As Figure 6.11 illustrates, the widths of the smeared event weight distributions are much larger than the 2-GeV increments used to generate the distributions. The root mean square (RMS) of the distributions ranges from approximately 30-45 GeV, with the width widening slightly with top mass (see Figure 6.12). Thus, the event weights may be coalesced into coarser mass bins without loss of information. A bin size of 25 GeV is arbitrarily chosen as a coarse binning that still remains smaller than the smallest observed RMS value.

Each event weight is rebinned from 125 2-GeV increments to 10 25-GeV increments, as in Figure 6.13. Each event weight is also normalized to unity, so that the event may be completely characterized by a nine-dimensional weight vector, $\vec{w}$. The components of $\vec{w}$ are the weights in each bin of the coarse histogram. The collection of weight vectors from all of the events in a mass sample are referred to as a *template*. Templates are generated for Monte Carlo top masses from 120 to 230 GeV. By comparing data events to templates for each mass, the mass of the top quark may be determined. The full details of this comparison are described in Chapter 7.

6.3.1 Background Templates

Templates from background processes are generated in the same manner as for top decays. The main difference between the two is that background templates tend to contain far fewer events than top templates, as event selection criteria were designed specifically to reduce backgrounds. The typical background template size is on the order of 50 events, while top templates contain 250-2500 events. This results in sums of event weight distributions that are much less uniform for background than for top events, as shown in Figure 6.14. The sample size of background templates is small enough that individual event peaks are visible in the distribution sums. This introduces an uncertainty to the shape of the background templates; the effect of this uncertainty will be explored in Chapter 8.

6.3.2 Null Weight Vectors

Even with multiple detector smearings per event, it is possible that an event may yield no real solution for any choice of top mass. Such events would produce a total event weight of zero, and thus create a non-normalizable weight vector. These events are ignored, and no weight vector is produced for them.

Instead, this effect is treated as a *de facto* additional selection cut. It is found that one out of every 500 or so $t\bar{t}$ events has no real solution, a selection efficiency of 99.8%. As one might expect, this effect is larger in background events, with an average of 4% of all background events failing to produce a solution. With these cuts applied, the expected yields described in Chapter 5 are revised to those shown in Table 6.1. Of the 22 events originally selected from data, 21 pass this new selection criterion. The remaining event (in the $\mu\mu$ decay channel) produces no solution consistent with a $t\bar{t}$ decay. Event weight distributions for these 21 events are shown in Figures 6.15 - 6.17.

TABLE 6.1. Expected Yields in Dilepton Channels, including Template Generation Efficiency

Source	Channel		
	$e\mu$	ee	$\mu\mu$
$t\bar{t}$ signal	9.79	3.48	2.53
$Z \to \tau\tau$	0.70 ± 0.16	$0.29^{+0.10}_{-0.13}$	0.07 ± 0.02
$Z \to ee$	-	0.43 ± 0.14	-
$Z \to \mu\mu$	-	-	0.91 ± 0.13
WW/WZ	0.71 ± 0.26	$0.19^{+0.11}_{-0.14}$	0.18 ± 0.03
QCD fakes	0.31 ± 0.28	0.09 ± 0.03	0.13 ± 0.03
Total Background	1.72 ± 0.41	$1.00^{+0.21}_{-0.24}$	1.29 ± 0.14
Observed Yield	**15**	**5**	**1**

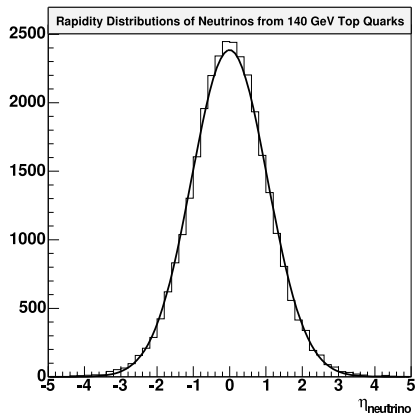

(a) m_{top} = 140 GeV

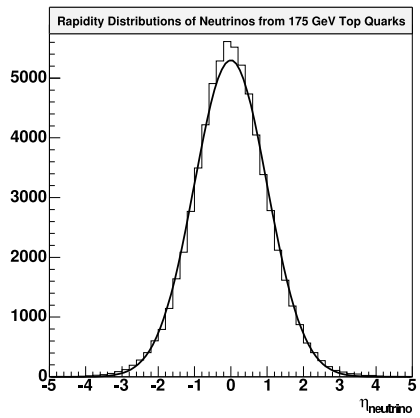

(b) m_{top} = 175 GeV

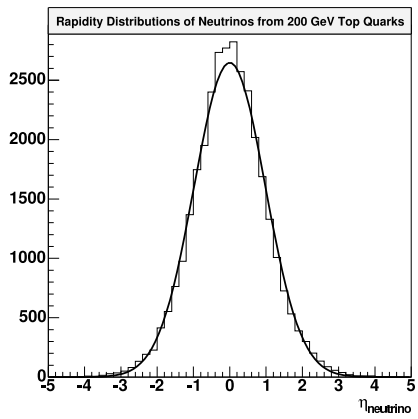

(c) m_{top} = 200 GeV

FIGURE 6.2. Parton-level neutrino rapidity distributions for Monte Carlo $t\bar{t}$ samples with various values of m_{top}. Gaussian fits to each distribution are also displayed.

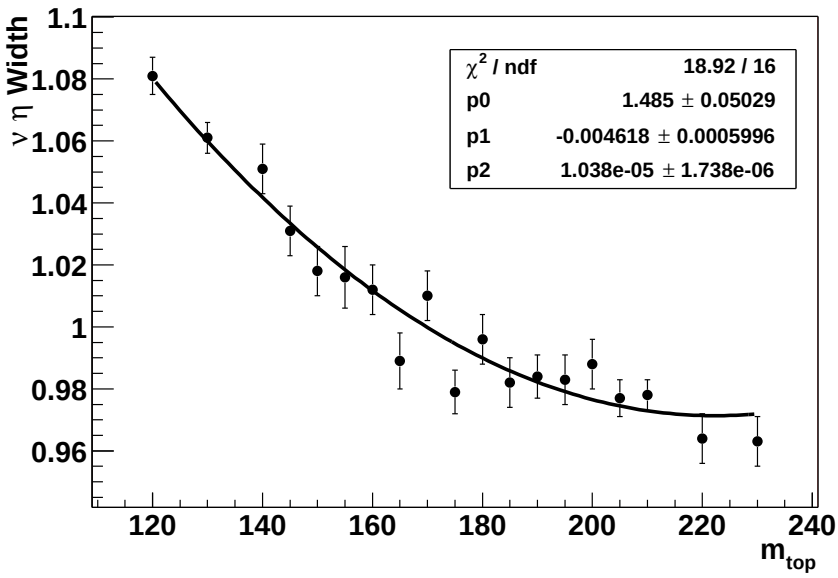

FIGURE 6.3. Dependence of the width of parton-level neutrino rapidity distributions on m_{top}. The solid line indicates the parameterization of this dependence.

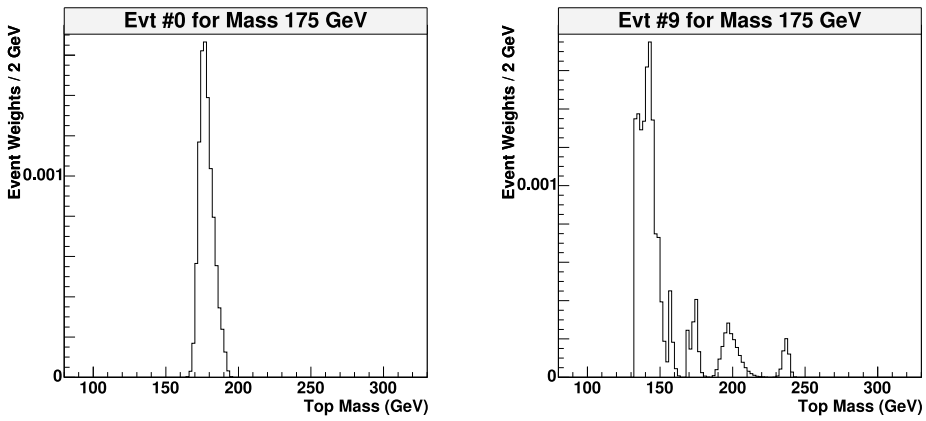

(a) (b)

FIGURE 6.4. Event weight distributions for two $t\bar{t}$ events with Monte Carlo-generated top quark mass of 175 GeV.

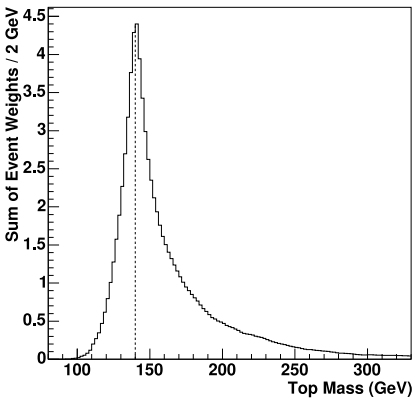

(a) m_{top} = 140 GeV (333 events)

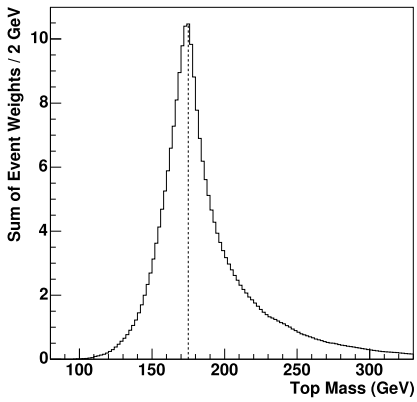

(b) m_{top} = 175 GeV (1323 events)

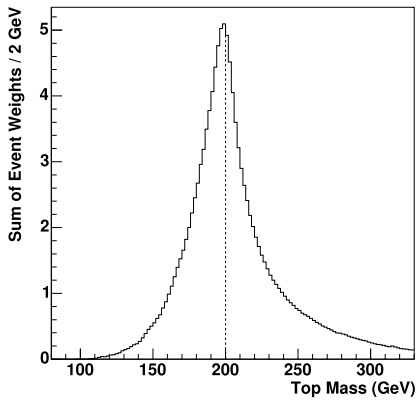

(c) m_{top} = 200 GeV (673 events)

FIGURE 6.5. Sums of event weight distributions from Monte Carlo $t\bar{t} \rightarrow \mu\mu$ decays, using parton-level information. Distributions are shown for top masses of 140 GeV, 175 GeV, and 200 GeV. This dashed vertical lines indicate the input top mass used in each sample.

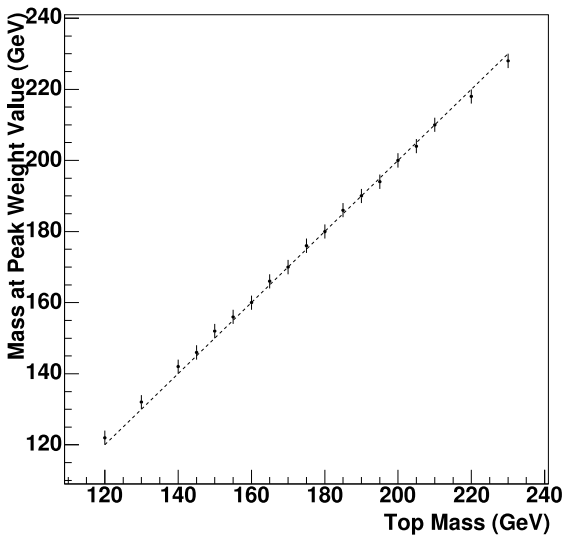

FIGURE 6.6. Peaks from sums of parton-level event weight distributions versus top quark mass. The dashed line indicates perfect agreement between the event weight peak and input top quark mass.

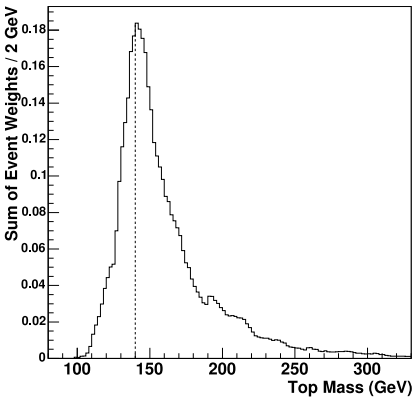

(a) m_{top} = 140 GeV (333 events)

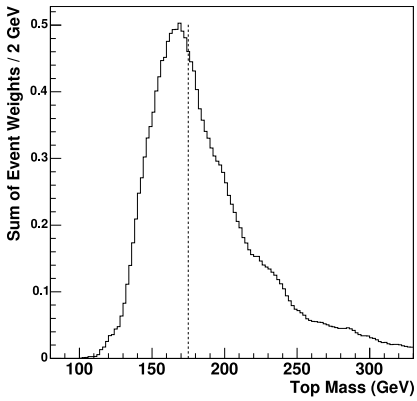

(b) m_{top} = 175 GeV (1323 events)

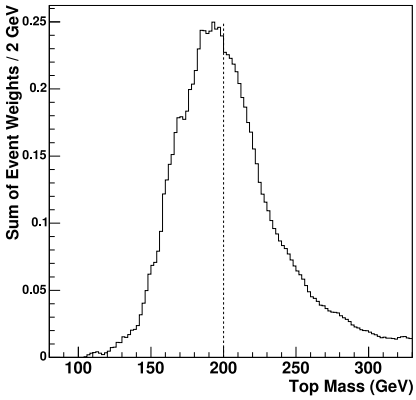

(c) m_{top} = 200 GeV (673 events)

FIGURE 6.7. Sums of event weight distributions from Monte Carlo $t\bar{t} \rightarrow \mu\mu$ decays, using particle-level information. Distributions are shown for top masses of 140 GeV, 175 GeV, and 200 GeV.

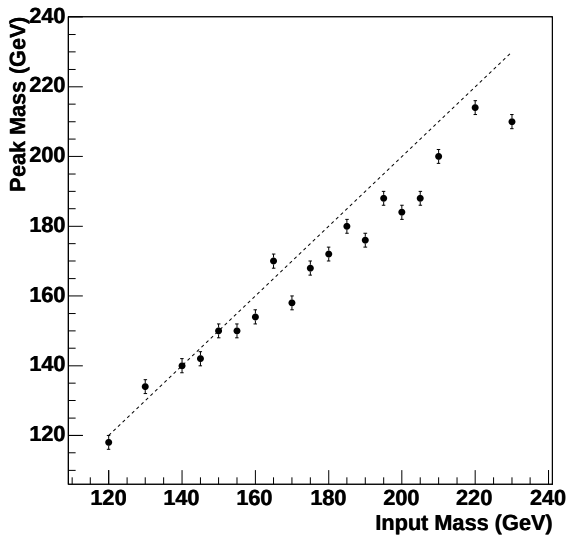

FIGURE 6.8. Peaks from sums of reconstructed particle-level event weight distributions versus top quark mass. The dashed line indicates perfect agreement between the event weight peak and input top quark mass.

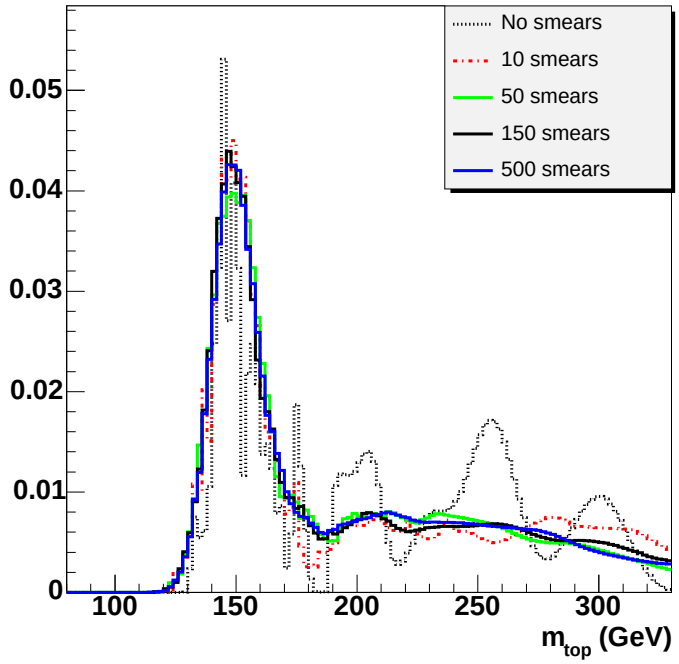

FIGURE 6.9. Event weight distributions for a 175 GeV Monte Carlo $t\bar{t}$ event with various amounts of detector smearing.

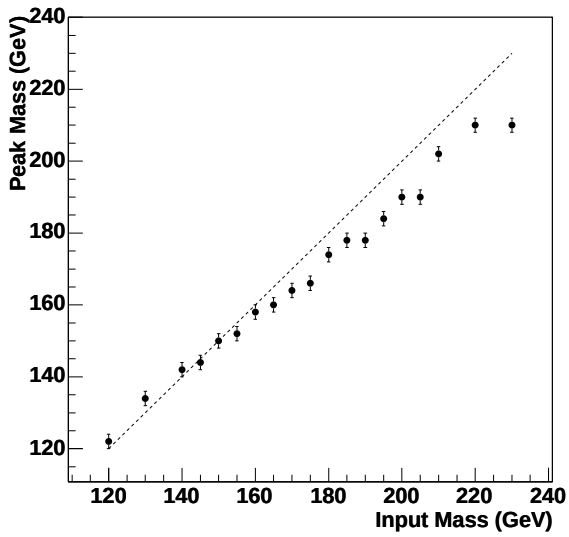

FIGURE 6.10. Peaks from sums of reconstructed particle-level event weight distributions versus top quark mass, with 150 smears over detector resolutions applied to each event. The dashed line indicates perfect agreement between the event weight peak and input top quark mass.

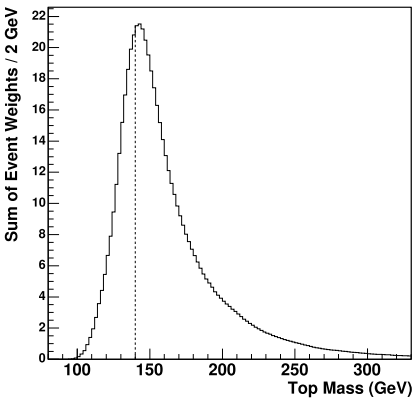

(a) m_{top} = 140 GeV (333 events)

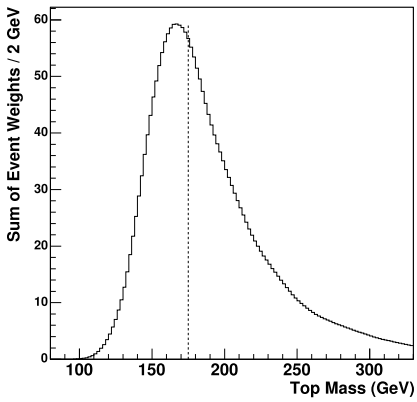

(b) m_{top} = 175 GeV (1323 events)

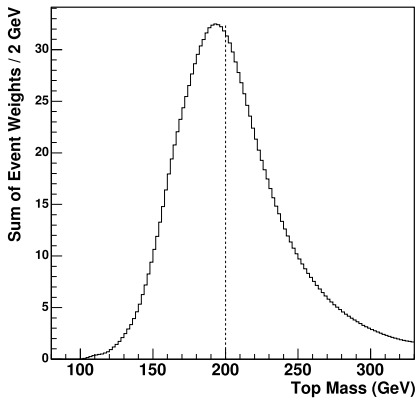

(c) m_{top} = 200 GeV (673 events)

FIGURE 6.11. Normalized sums of event weight distributions from Monte Carlo $t\bar{t} \rightarrow \mu\mu$ decays using particle-level information. Particles in each event are smeared 150 times. Distributions are shown for top masses of 140 GeV, 175 GeV, and 200 GeV.

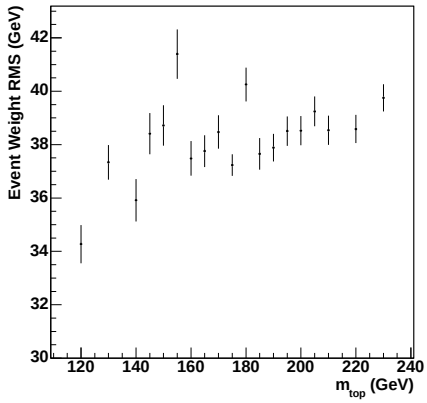

FIGURE 6.12. Average RMS versus top mass for Monte Carlo $t\bar{t}$ samples.

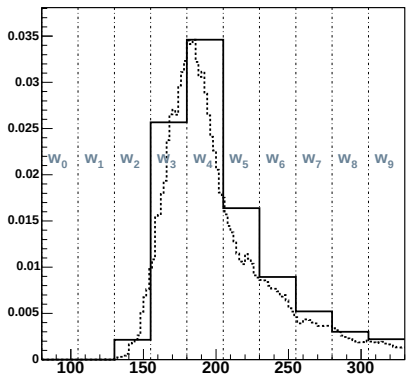

FIGURE 6.13. A 175-GeV event weight distribution, before and after rebinning into 25-GeV bins.

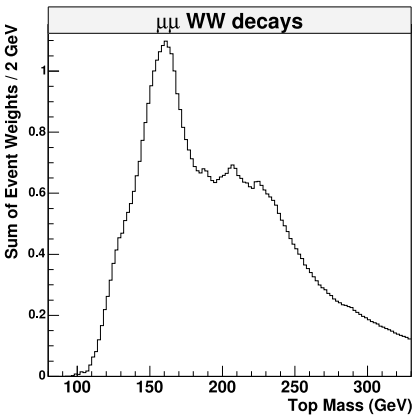

(a) $WW \to \mu\mu$

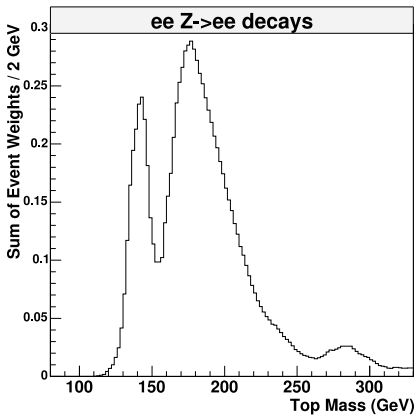

(b) $Z \to ee$

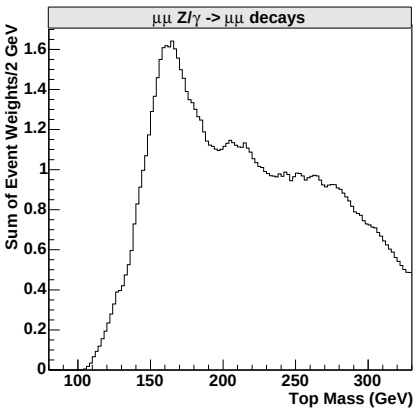

(c) $Z \to \mu\mu$

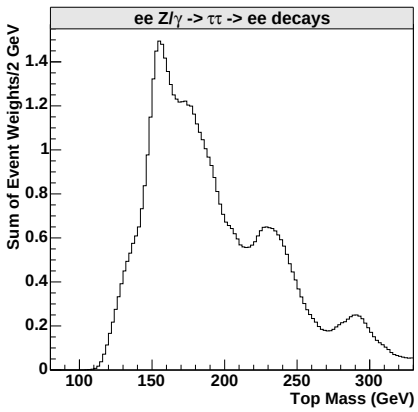

(d) $Z \to \tau\tau \to ee$

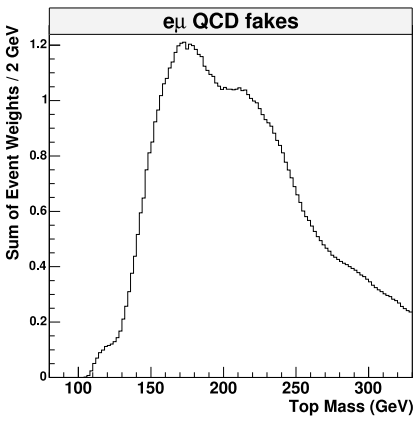

(e) $e\mu$ QCD Fakes

FIGURE 6.14. Sums of smeared event weight distributions for dominant background processes in the dilepton decay channels.

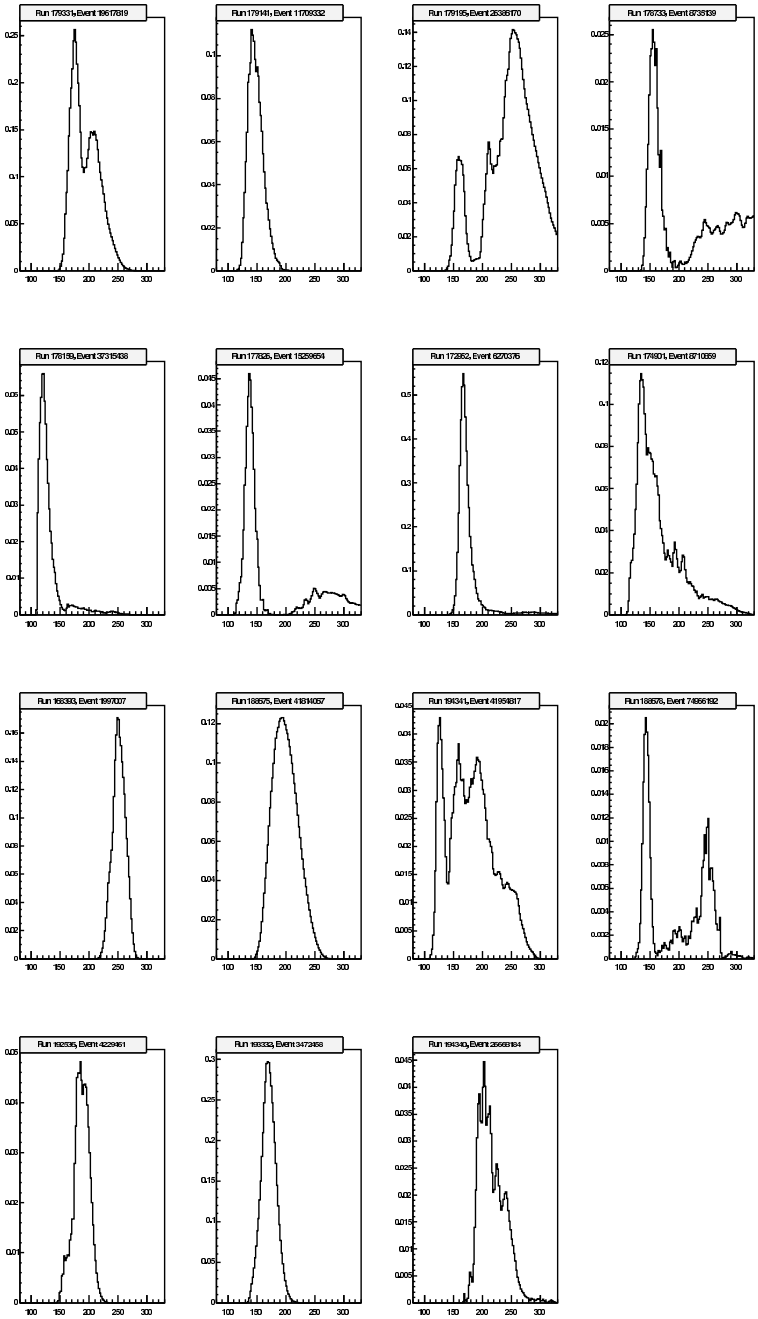

FIGURE 6.15. Event weight distributions for the 15 $e\mu$ events seen in data.

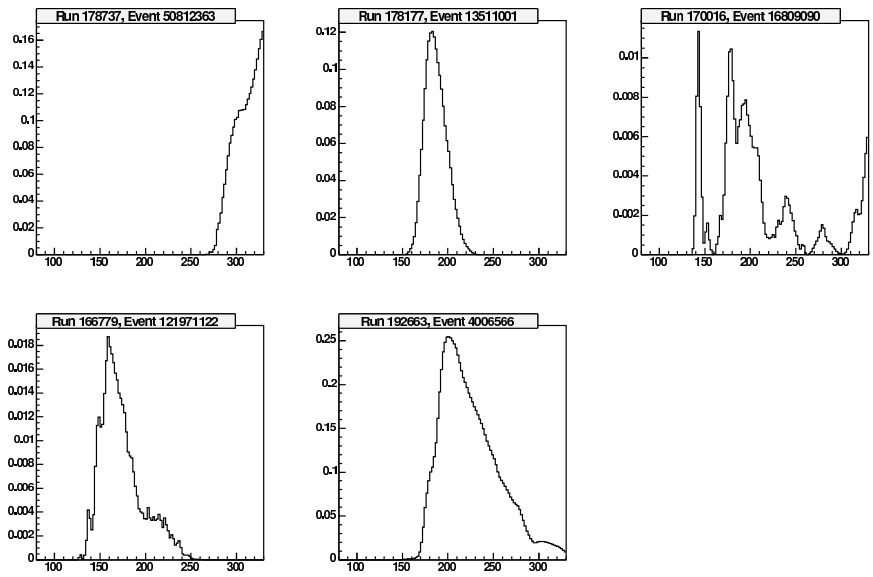

FIGURE 6.16. Event weight distributions for the 5 *ee* events seen in data.

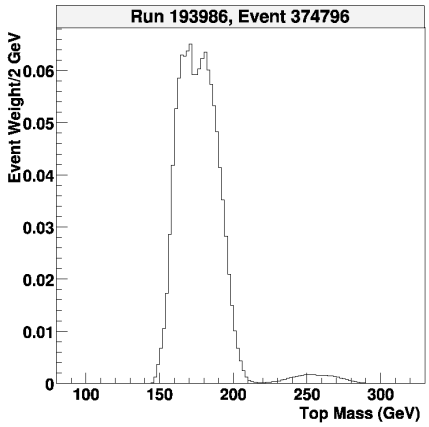

FIGURE 6.17. Event weight distribution for the 1 $\mu\mu$ event with non-zero weight seen in data.

CHAPTER 7
LIKELIHOOD FIT

Once event weight vectors have been created for all Monte Carlo events, it remains to compare them to weight vectors from data events in order to obtain a measurement of the top quark mass. This comparison is made through the use of a maximum likelihood fit. This chapter explores the formation of the likelihood function used for the fit, the optimization of parameters within the fit, and the results of the fit on ensembles of simulated event data.

7.1 Principles of Likelihood Fits

A probability density function (PDF) $f(\mathbf{x}|\alpha)$ with a set of parameters α allows one to predict the probability that a set of measurements $\mathbf{x}$ will take on a certain value. Conversely, if the values of α are unknown, they can be estimated from multiple measurements of $\mathbf{x}$. The PDFs from all N events within a data sample can be combined to form a joint likelihood

$$L(\mathbf{x}|\alpha) = \prod_{i=1}^{N} f(\mathbf{x}_i|\alpha). \tag{7.1}$$

An estimate $\hat{\alpha}$ of the parameters α may be found by maximizing the value of this likelihood [56]. It is computationally convenient to use the logarithm of the likelihood:

$$\ln L(\mathbf{x}|\alpha) = \sum_{i=1}^{N} \ln f(\mathbf{x}_i|\alpha), \tag{7.2}$$

rather than the likelihood itself for this maximization. The maximum of this function (or, equivalently, the minimum of $-\ln L$) occurs at the same $\hat{\alpha}$ as for Equation 7.1. Furthermore, it can be shown that, in the limit of an infinite number of data events, the uncertainty in $\hat{\alpha}$ is described by the region in which the value of $\ln L(\mathbf{x}|\alpha)$ differs by less than 0.5 units from its maximum value. Section 7.3 discusses the applicability of this uncertainty estimation to the low-statistics sample used in the determination of m_{top}.

In this analysis, α is composed of m_{top} and the number of signal (n_s) and background (n_b) events in the data sample. The set of observed values contains the number of observed events in the sample (N), the set of event weight vectors ($\{\vec{w}\}$), and the expected number of background events ($\bar{n}_b \pm \sigma_b$), as estimated in Chapter 6.

One could also include an expectation for the total number of signal events ($\bar{n}_s$) in the set $\mathbf{x}$. However, an estimate of $\bar{n}_s$ requires assuming a value for the top production cross section. As mentioned in Chapter 2, such an assumption in turn implies an assumed value of m_{top}. Since this analysis seeks to obtain a measurement of m_{top} without a prior estimate of its value, $\bar{n}_s$ is ignored in the formation of the likelihood.

The parameters n_s and n_b may be easily treated as continuous variables for the purposes of the minimization of $-\ln L$. It is not so easy to treat m_{top} in the same manner, as Monte Carlo samples exist only for certain discrete top mass values. In principle, one could use these samples to create a parameterization of the PDF as a function of m_{top}, allowing for the $-\ln L$ function to be simultaneously minimized with respect to m_{top}, n_s, and n_b. Alternately, once can minimize the $-\ln L$ only with respect to n_s and n_b at each Monte Carlo mass point, and then parameterize the resulting likelihood values with respect to m_{top}.

The second approach is chosen for this analysis. The MINUIT [57] package is used to numerically calculate the minimum value of $-\ln L$ at each mass point. A polynomial fit is then performed to find the mass value at which $-\ln L$ reaches an overall minimum.

7.2 Functional Form of the Likelihood

The likelihood function L($\{\vec{w}\}$,$\bar{n}_b, \sigma_b$,$N|m_{top}$,n_s,n_b) consists of three components. Consistency between the observed and expected number of background events is enforced through a gaussian constraint:

$$g(n_b, \bar{n}_b, \sigma_b) \equiv \frac{1}{\sqrt{2\pi\sigma_b}} exp[(n_b - \bar{n}_b)^2/2\sigma_b^2], \tag{7.3}$$

where σ_b is the uncertainty in the background yield.

A Poisson constraint requires agreement between the total observed number of events and the sum of n_s and n_b:

$$p(n_s + n_b, N) \equiv \frac{(n_s + n_b)^N e^{-(n_s+n_b)}}{N!}. \tag{7.4}$$

The remaining likelihood component $L^*(\{\vec{w}\}|m_{top}, n_s, n_b)$ describes the probability that the set of observed event weights $\{\vec{w}\}$ agree with the template weights for a given m_{top}. The overall likelihood may thus be written as

$$L(\{\vec{w}\}, \bar{n}_b, \sigma_b, N|m_{top}, n_s, n_b) = g(n_b, \bar{n}_b, \sigma_b)p(n_s + n_b, N)L^*(\{\vec{w}\}|m_{top}, n_s, n_b). \tag{7.5}$$

The function L^* is calculated from the probability that each observed weight vector $\vec{w}$ is consistent with either a signal or background event. This probability is calculated through the use of the continous signal and background probability densities, $f_s(\vec{w}|m_{top})$ and $f_b(\vec{w})$. These signal and background functions are not known directly, but are instead estimated from the event weight vectors within their respective templates [58]. A kernel function K is placed at the value of each event weight vector, and the probability density $f(\vec{w})$ is estimated by averaging over all vectors $\vec{w}_i^{MC}$ within a Monte Carlo template:

$$f(\vec{w}) = \frac{1}{N_{MC}h^d} \sum_{i=1}^{N_{MC}} K(\frac{\vec{w} - \vec{w}_i^{MC}}{h}) \tag{7.6}$$

The resulting function $f(\vec{w})$ provides an estimate of the agreement of the observed weight vector $\vec{w}$ and the weight vectors within the Monte Carlo template. In this function, h is a smoothing parameter that may be tuned to optimize the performance of the likelihood fit. This optimization is discussed in Section 7.3.

A gaussian is commonly used as a kernel function, and serves as a convenient choice here. The kernel function is defined as a multidimensional gaussian over the nine dimensions of the weight vector $\vec{x}$:

$$K(\vec{x}) = \frac{1}{(2\pi)^{9/2}} \prod_{j=1}^{9} e^{-x_j^2/2}. \tag{7.7}$$

The normalization of this gaussian assumes that $\vec{x}$ may take on any value. However, the normalization of the weight vectors implies that

$$\sum_{i=1}^{9} x_i \leq 1. \tag{7.8}$$

The normalization of the gaussian should thus take place only over this allowed space. Since such a normalization is computationally intensive, an integration is instead performed over the hypercube $0 \leq x_i \leq 1$, and the result is used as a normalizing factor for the kernel K. The signal probability density $f_s(m_{top})$ may then be expressed as

$$f_s(\vec{w}|m_{top}) = \frac{1}{N} \sum_{i=1}^{N_{MC}(m_{top})} \prod_{j=1}^{9} \frac{exp[-(w_j - w_{ji}^{MC})^2/2h^2]}{\int_0^1 exp[-(w' - w_{ji}^{MC})^2/2h^2]dw'}. \tag{7.9}$$

This limits of the normalization integral are not strictly correct, in that they allow individual weight vector components between 0 and 1, rather than applying the stricter requirement of Equation 7.8. However, the effect of using these loose limits is small, as seen in Section 7.3.

The background probability density is defined similarly. Because there may be multiple backgrounds within a channel, the contribution from each background k is weighted according to its expected contribution to the overall background, b_k:

$$\frac{b_k N_k^{MC}}{\sum_{k=1}^{N_{bg}} b_k N_k^{MC}} = \frac{\bar{n}_{b,k}}{\bar{n}_b}. \tag{7.10}$$

Here, $\bar{n}_{b,k}$ is the expected number of background events from the kth background, and N_k^{MC} is the number of weight vectors within the template for that background. The weight b_k may differ from the ratio of $\bar{n}_{b,k}$ to the total expected background $\bar{n}_b$ due to the fact that the number of events within a template is not constant for all backgrounds.

The background probability density is found by summing over all events in each background template:

$$f_b(\vec{w}) = \frac{1}{\sum_{k=1}^{N_{bg}} b_k N_k^{MC}} \sum_{k=1}^{N_{bg}} b_k \sum_{i=1}^{N_k^{MC}} \prod_{j=1}^{9} \frac{exp[-(w^i - w_{ji}^{MC})^2/2h^2]}{\int_0^1 exp[-(w' - w_{ji}^{MC})^2/2h^2]dw'}. \tag{7.11}$$

Finally, the overall likelihood may be expressed in terms of f_s and f_b as

$$L(\{\vec{w}\},\bar{n}_b,N|m_{top},n_s,n_b) = g(n_b,\bar{n}_b,\sigma_b)p(n_s+n_b,N)\prod_i^N \frac{n_s f_s(\vec{w}|m_{top})+n_b f_b(\vec{w})}{n_s+n_b}. \quad (7.12)$$

The negative logarithm of this function is then maximized with respect to n_s and n_b at each Monte Carlo top mass. A fit is performed on the resulting likelihood points to find the most likely value for the top mass. This fit is discussed in the following section.

A full treatment of the PDE method requires transforming the weight vectors $\vec{w}_i$ into a basis in which the elements of the vectors are uncorrelated. While a simple linear transformation can diagonalize the covariance matrices of both the signal and background probability densities, such a transformation creates computational difficulties in evaluating the integrals in Equations 7.9 and 7.11. Preliminary attempts at evaluating the probability densities in the transformed bases were found to increase the computing time needed to evaluate f_s and f_b but showed no improvement over results in the unchanged bases. The basis change was thus abandoned for this analysis. Correlations between weight vector elements were tested through ensemble tests, as described in the next section.

7.3 Optimization of the Likelihood Fit

Once the likelihood function described above is minimized at each Monte Carlo mass point, it remains to fit the points to a continuous function. The minimum of this function is taken as an estimate of the top quark mass. The range between the minimum of the function and the points at which the function is 0.5 units greater than its minimum is used to define the uncertainty on the mass measurement.

The form of the likelihood fit function is not assumend beforehand, but is determined through tests on Monte Carlo ensembles. The range over which this fit must be performed is likewise unknown prior to ensemble testing. Lastly, the likelihood function contains a smoothing parameter h whose value must also be determined empirically.

Fits are tested by forming test ensembles of events from the Monte Carlo templates. Ensembles are generated separately in the ee, $e\mu$, and $\mu\mu$ channels, with the number of

events in each channel's ensemble equal to the observed number of events in that channel. Events from both signal and background templates are included in the ensembles through the use of a random number generator. For an ensemble of N events with $\bar{n}_b$ expected background events, a random number between 0 and N is generated. If the number is less than $\bar{n}_b$, an event is chosen from the background template. Otherwise, an event is picked from a signal template. In the case where there are multiple backgrounds, an event from background k is chosen if the random number R meets the condition

$$\sum_{i=1}^{k-1} \bar{n}_{b,i} \leq R \leq \sum_{i=1}^{k} \bar{n}_{b,i}.$$

Event weights used in the ensemble are removed from the templates, so as not to bias the comparison between ensemble and template events. Likelihoods are then calculated for the ensemble events. Ensemble tests over the combined dilepton channels are performed by summing likelihoods over the three individual channels.

Due to the finite statistics available in the templates, the likelihood values are not known to infinite precision. An estimate of the uncertainty on the likelihood value is made splitting each template into smaller "sub-templates". Likelihoods are generated for a test ensemble using each of these sub-templates. The resulting variance of likelihood values is taken as an estimate of the likelihood uncertainty.

The uncertainty in likelihood values is calculated by generating ensembles ensembles of 21 dilepton events at $m_{top} = 175$ GeV. For the sake of simplicity, only $e\mu$ signal events are used in these ensembles. For a given ensemble of events, all templates are divided into 10 sub-templates. Likelihood values are calculated for the ensemble at each mass point using each of the sub-templates in turn, and the standard deviations of the values at each mass point are calculated. These deviations are then divided by $\sqrt{10}$ to provide an estimate of the uncertainty of the likelihood measurement using the original templates.

Table 7.1 shows likelihood uncertainties from five ensemble tests of 21 $e\mu$ events. It is clear from this table that uncertainties may vary greatly from ensemble to ensemble. However, no systematic change in the size of the uncertainty as a function of top quark

mass is observed. Thus, the average uncertainty of 0.5 as taken from ensemble tests is used as the estimated likelihood uncertainty on all mass points. The exact value of the average is less important than the assumption that the uncertainties do not vary with mass, as it is such variances that can affect the performance of the likelihood fit. The fit is described in more detail in Section 7.3.1.

Further ensemble tests are performed using sets of 2, 5, and 25 sub-templates. The choice of the number of sub-templates to use for these tests is somewhat arbitrary. A small number of sub-templates may not be sufficient to calculate a reasonable average. On the other hand, if templates are divided into a large number of sub-templates, the individual sub-templates may not contain enough events to provide a reasonable estimation of the probability density. Nonetheless, Table 7.2 shows that the results of these tests are consistent with those seen using 10 sub-templates.

An ideal likelihood fit has the following two properties:

- The mass at the likelihood fit minimum for an ensemble matches the input top mass m_{top}.
- The pull distribution for a set of ensembles is a gaussian with width of one, where *pull* is defined as $(m_{fit} - m_{top})/\sigma_L$, and σ_L is the uncertainty from the likelihood fit. A pull width of one indicates that the error estimate from the (minimum likelihood +0.5) points is justified.

Ensemble tests are performed on a number of different fit functions, fit ranges, and h values to determine the optimal values for the likelihood fit.

7.3.1 Fit Functions

If the likelihood function is gaussian, then one would naively expect that $-\ln L$ would be modeled well by a quadratic fit function. Such a function has the additional advantage that any successful fit necessarily contains points at which the function value is 0.5 units greater

TABLE 7.1. Likelihood uncertainties for ensemble tests using 10 sub-templates

m_{top} (GeV)	Ensemble Test # 1	2	3	4	5
120	0.72	0.59	0.52	0.69	0.63
130	0.44	0.67	0.40	0.71	0.81
140	0.73	0.74	0.18	0.58	0.79
150	0.74	0.60	0.17	0.67	0.60
160	0.48	0.55	0.25	0.50	0.45
170	0.57	0.47	0.21	0.58	0.52
180	0.35	0.29	0.21	0.16	0.47
190	0.48	0.51	0.70	0.55	0.26
200	0.36	0.41	0.31	0.55	0.34
210	0.57	0.25	0.44	0.67	0.40
220	0.45	0.38	0.44	0.76	0.34
230	0.21	0.42	0.34	0.58	0.27

TABLE 7.2. Likelihood variances for sub-templates, averaged over all mass points.

Test #	Number of sub-templates 2	5	10	25
1	0.45±0.44	0.78±0.54	0.74±0.38	0.75±0.46
2	0.25±0.15	0.34±0.23	0.41±0.25	0.44±0.26
3	0.27±0.27	0.48±0.37	0.54±0.36	0.61±0.40
4	0.24±0.21	0.41±0.27	0.48±0.33	0.52±0.35
5	0.38±0.37	0.43±0.28	0.55±0.35	0.61±0.39
6	0.18±0.11	0.38±0.26	0.42±0.25	0.47±0.29
7	0.55±0.49	0.55±0.32	0.72±0.43	0.81±0.46
8	0.61±0.61	0.56±0.28	0.77±0.43	0.91±0.42

than its minimum value. This is not the case for higher order fits, which may peak at a local maximum before reaching a point 0.5 units greater than the minimum, as in Figure 7.1. Such fits yield a fit mass but do not necessarily provide a useful estimate of the uncertainty on that mass.

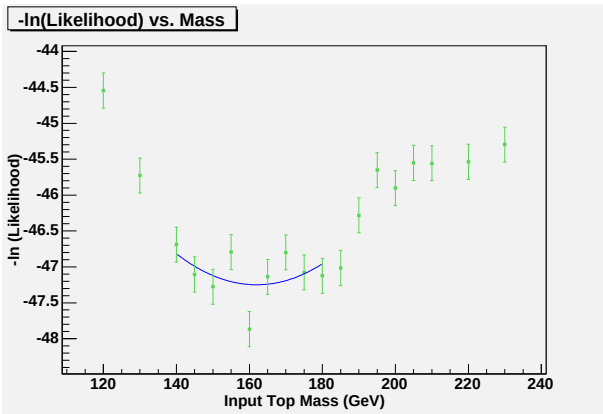

(a) quadratic fit

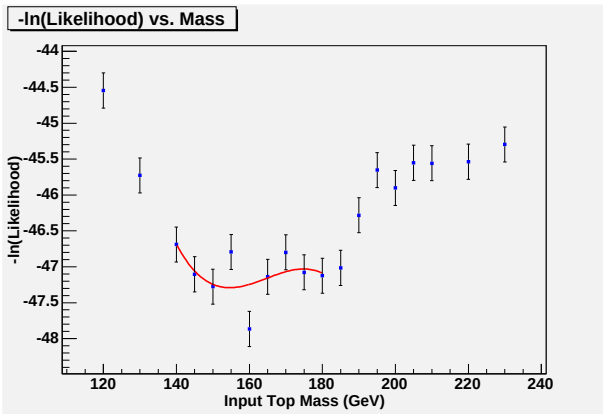

(b) cubic fit

FIGURE 7.1. Quadratic and cubic fits to an ensemble of 15 *ee* events. Note that the cubic fit reaches a maximum before reaching the (maximum+0.5) point.

The function used for the likelihood fit is determined from ensemble tests performed using quadratic, cubic, and quartic fit functions. Tests are performed on 1,000 ensembles of combined dilepton events over all mass points from 120 GeV to 230 GeV. Ensemble fit minima less than 70 GeV are arbitrarily set to 70 GeV, with an uncertainty of 50 GeV

assigned in order to reduce the effect of poorly fit ensembles on the average fit. Likewise, minima above 280 GeV are set to 280±50 GeV. It is found that minima occur at such extreme values only for masses less than 140 GeV or greater than 210 GeV, where the number of mass point used in likelihood fits is reduced. As discussed in Secton 7.3.3, these masses are thus excluded when calibrating the likelihood fitter.

It is found that the cubic and quartic fits do not provide a significant improvement in agreement between input mass and likelihood minimum over the quadratic fits. The higher order fits do substantially increase the fraction of ensembles which do not yield a good estimate of the fit uncertainty, as illustrated in Figure 7.2. (Here, a "good estimate" is defined as a fit with local maximum values greater than 0.5 units above the minimum value on either side of the minimum.) For these reasons, a quadratic function is used to fit all the likelihood points.

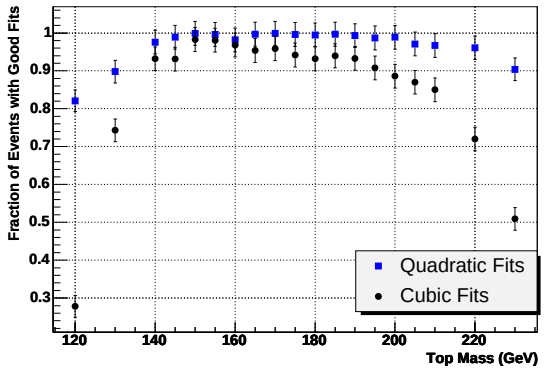

FIGURE 7.2. Fraction of dilepton ensembles with good estimates of fit uncertainties from quadratic and cubic fits.

7.3.2 Fit Range

Further Monte Carlo tests were performed to determine the range of mass values over which to perform the likelihood fit. Because templates exist for only a few masses, a fit range that is too narrow may include insufficient points for determining the likelihood minimum.

Conversely, since the likelihood function presumably goes to a constant value far from the input top mass (where the minimization of $-\ln L$ yields $n_s \rightarrow 0$), a fit range that is too wide will overestimate the uncertainty in the minimum, as in Figure 7.3. The best value for the fit range is found by simultaneously optimizing the range with the value of the h parameter.

7.3.3 h Parameter

As with the fit ranges, the choice of h must be balanced between values that are too small and values that are too large. A value of h that is too small results in a gaussian that approaches a delta function, yielding no information about event weight vectors that do not exactly match a template weight vector. Values that are too large broaden the gaussian and allow for little distinguishability between weight vectors with different values.

Ensemble tests were performed for h values between 0.05 and 0.50, testing h in increments of 0.05. Tests were also performed for fit ranges between ± 10 and ± 50 GeV, incrementing the ranges by 10 GeV. For each test, 100 ensembles of signal and background events were generated. Fifteen events were chosen from the $e\mu$ channel, 5 from the ee channel, and 1 from the $\mu\mu$ channel in order to mimic the results from data. The average of the likelihood minima at each mass point was plotted against the input mass, with both the minima average and the input mass shifted by 175 GeV. A linear fit was then applied to the result:

$$\text{(Likelihood minimum - 175 GeV)} = M(m_{top}\text{-175 GeV}) + B. \tag{7.13}$$

Here, M is the slope of the linear fit, and B is the offset at a mass of 175 GeV. Pull distributions were also generated, as in Figure 7.4. As not all pull distributions appear gaussian, the root mean square (RMS) of the pull distribution rather than the width of a fitted gaussian was used to characterize the width of the distribution.

One wishes to find a set of values for h and the fit range that generates a fit slope of M=1, an offset of 0, and a pull RMS of 1. As the plots in Figure 7.5 show, no combination of h and fit range meets all of those requirements. Values of h and fit range are instead

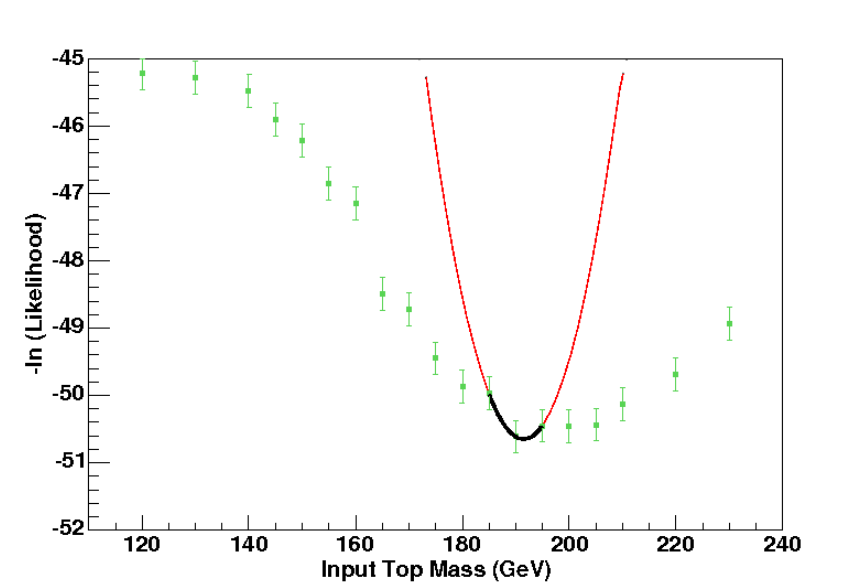

(a) ±5 GeV fit

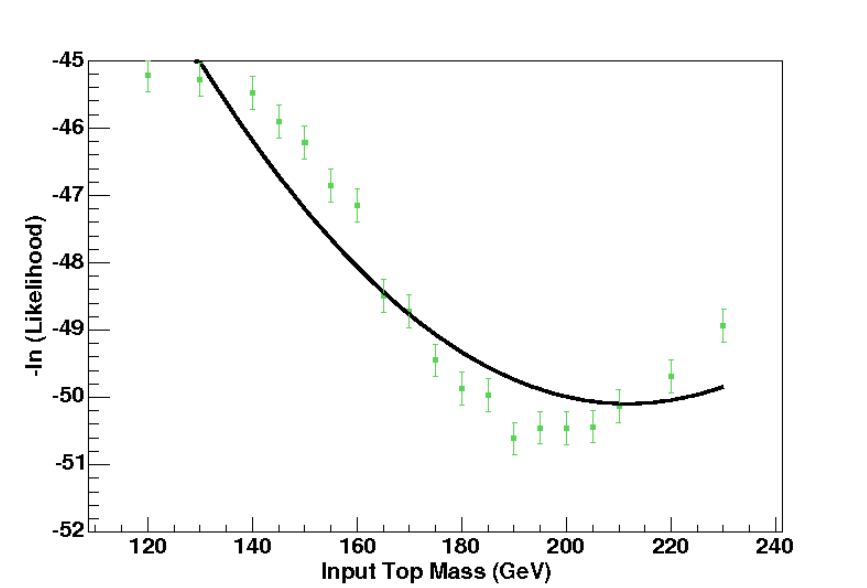

(b) ±100 GeV fit

FIGURE 7.3. Fits in the range (a) ±5 GeV and (b)±100 GeV around the minimum for an ensemble of 15 $e\mu$ events at m_{top} = 175 GeV. In Figure (a) the red line indicates the extension of the black fit parabola beyond the ±5 GeV fit range.

chosen to produce a fit slope and offset near their optimal values while still generating a pull RMS consistent with 1.

The values of h and fit range chosen for the likelihood fit are 0.15 and ± 20 GeV, respectively. Further ensemble tests were performed on 1,000 combined dilepton ensembles using these fit values. The resulting pull RMS values have an average of ≈ 0.94 for masses in the range 140 to 210 GeV, as shown in Figure 7.7. This average is pulled down by ensembles at low values of m_{top}. Values above 160 GeV show pull RMS values within a few percent of the ideal value of 1.0. RMS values for masses of 120, 130, 220, and 230 GeV are not included in Figure 7.7, as a large fraction of events at these points have fits outside the allowed fit mass region of 70-280 GeV. Such events appear as peaks at pull values of ± 1, as in Figure 7.6.

Figure 7.8 shows that the relationship between likelihood minima and input masses is adequately described by a linear fit. Mass points below 140 GeV or above 210 GeV are again excluded due to the large fraction of poorly fit minima at those points. The slope and offset of a linear fit to the remaining points are 0.96 and 1.7 GeV, respectively. The deviation of these values from their ideals may be due to the approximation used in the likelihood normalization, as discussed in Section 7.2. The slope and offset observed from the Monte Carlo tests are used as corrective calibration factors for the likelihood minimum observed in data.

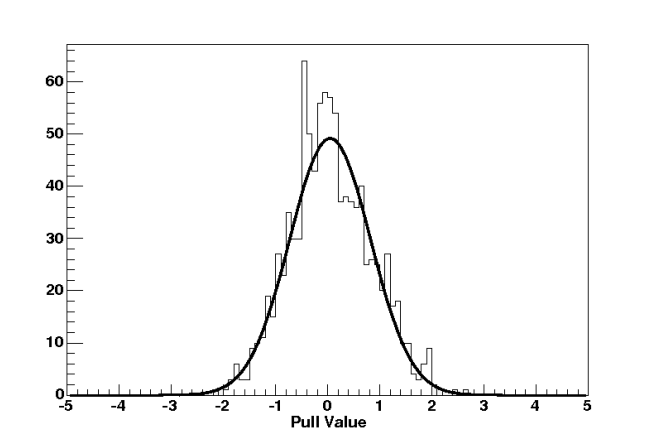

(a) 150 GeV

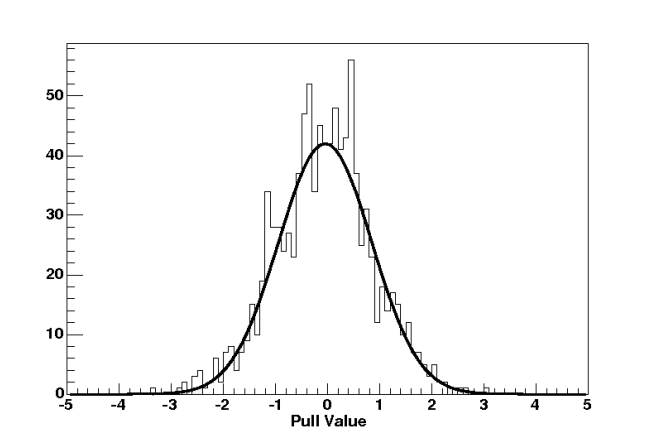

(b) 175 GeV

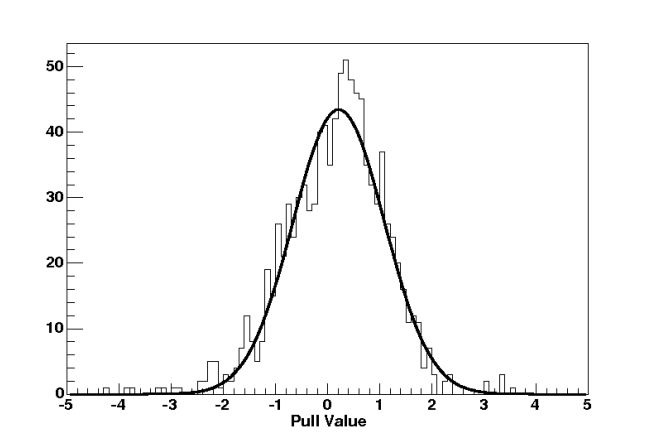

(c) 200 GeV

FIGURE 7.4. Pull distributions for 1,000 ensembles of 21 dilepton events at (a) 150 GeV, (b) 175 GeV, and (c) 200 GeV.

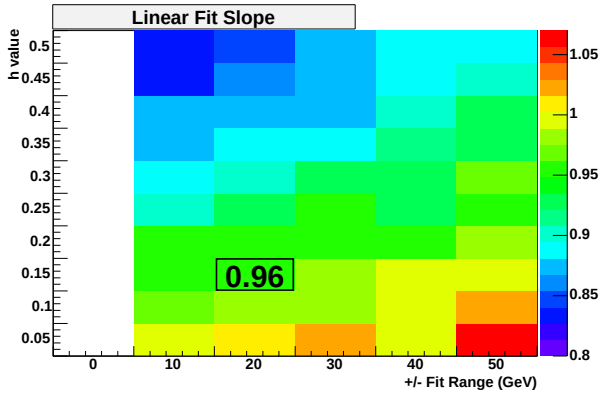

(a) M

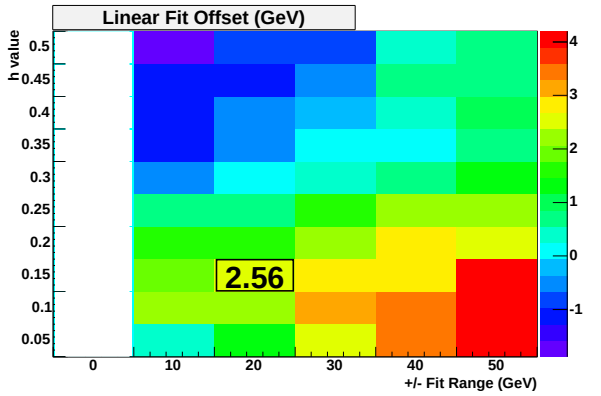

(b) B (GeV)

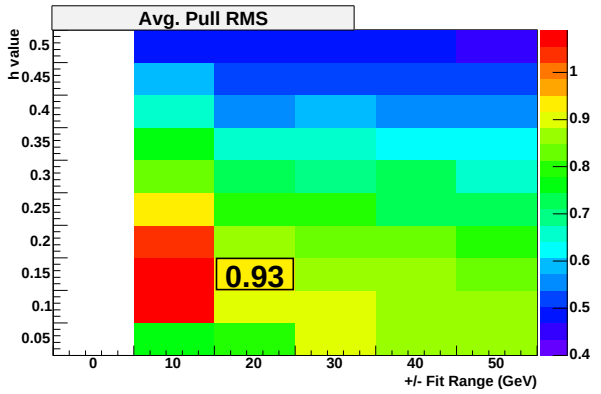

(c) Pull RMS

FIGURE 7.5. (a) Linear fit slope, (b) fit offset, and (c) pull RMS vs. fit range and *h*.

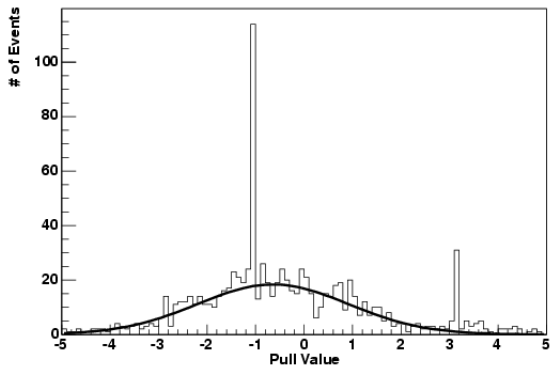

(a) 120 GeV

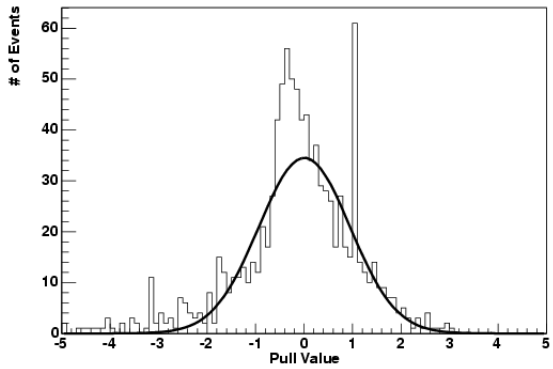

(b) 230 GeV

FIGURE 7.6. Pull distributions for (a) 120 GeV and (b) 230 GeV input top quark masses. The peaks at ± 1 indicate events in which the likelihood fit minimum is outside the allowed range of 70-280 GeV.

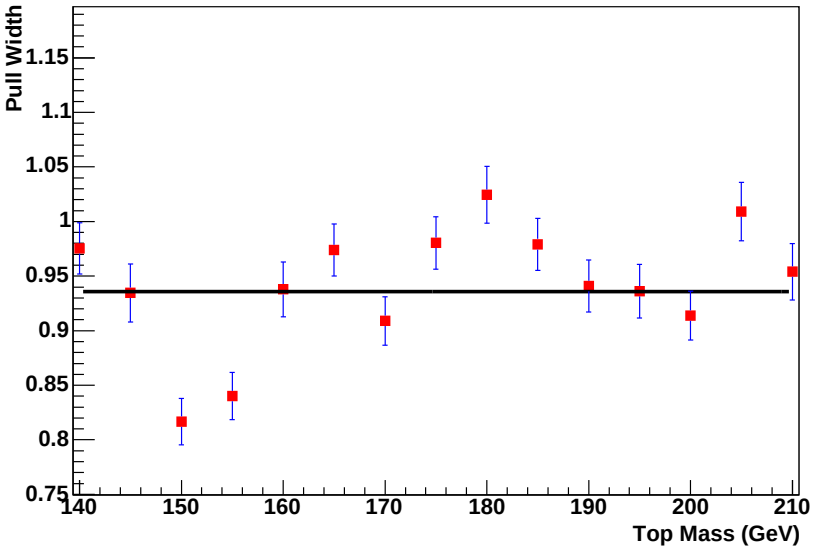

FIGURE 7.7. Widths of pull distributions versus m_{top}

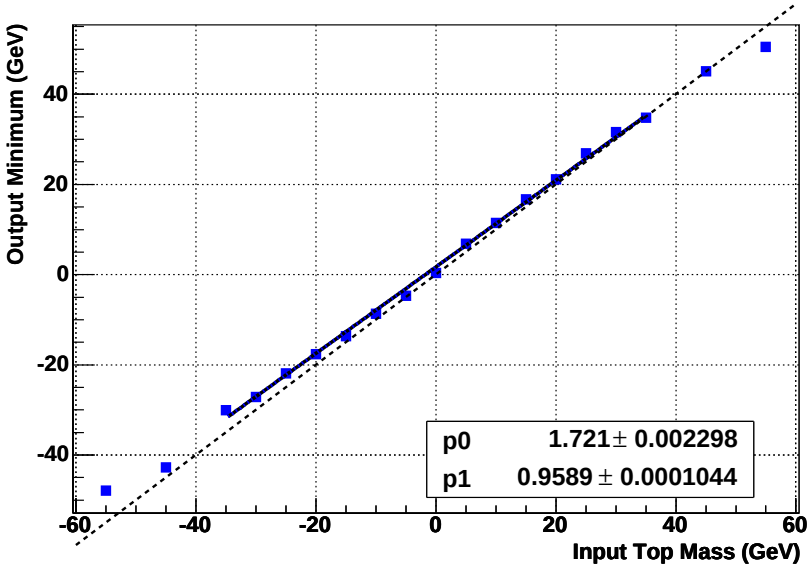

FIGURE 7.8. Linear fit of -ln$L$ minima to m_{top}.

CHAPTER 8
RESULTS

Using the likelihood fit procedure described in the previous chapter, event weight vectors from the 21 candidate dilepton events may be compared to the Monte Carlo signal and background templates. The result of that fit provides a measurement of the top quark mass along with the statistical uncertainty on that measurement. Further studies estimate additional systematic uncertainties. These studies are described in this chapter, and a measurement of the top quark mass is provided.

8.1 Likelihood Fit to Data

The log-likelihood fits for the 15 $e\mu$ events, 5 ee events, and 1 $\mu\mu$ event are shown in Figure 8.1. The respective minima are at 148 ± 11, 198 ± 17, and 183 ± 34 GeV. The combined fit is performed by summing the logarithms of the likelihoods of the individual channels, as in Figure 8.2, and the minimum occurs at 178 GeV. Calibrating this according to the fit in Figure 7.8 yields a top mass of 175.6 GeV, with a statistical error of ± 10.7 GeV.

The large difference in minima between the $e\mu$ and ee channels is cause for concern, but is not entirely unexpected. Figure 8.3 shows distributions of fit minima over 1000 Monte Carlo ensembles of $e\mu$ and ee events with $m_{top} = 175$ GeV. Roughly 1% of $e\mu$ events produce minima less than 150 GeV, while 89% of ee events produce minima above 190 GeV. Distributions of minima from $\mu\mu$ events are not shown, as the low signal-to-background ratio in these events produces a wide range of minima. This also accounts for the large statistical uncertainty in the $\mu\mu$ channel.

The observed overall statistical uncertainty is in line with expectations, as demonstrated in Figure 8.4. Over 1000 combined Monte Carlo samples of dilepton events, the average

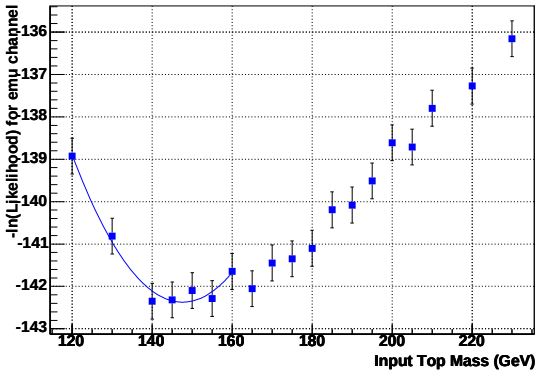

(a) $e\mu$

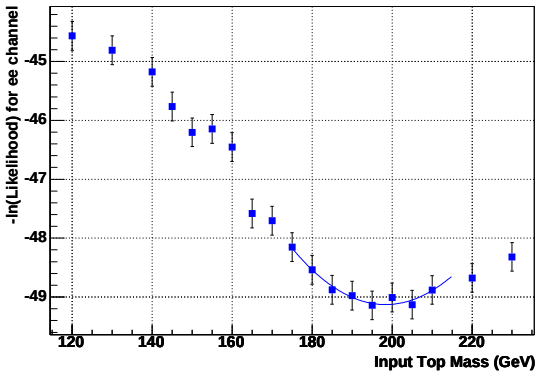

(b) ee

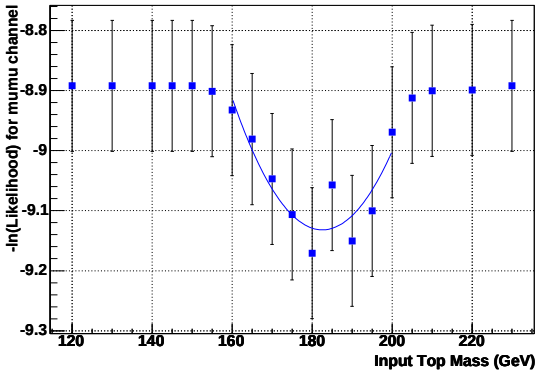

(c) $\mu\mu$

FIGURE 8.1. -ln (Likelihood) minima versus mass for data events in the (a) $e\mu$, (b) ee, and (c) $\mu\mu$ channels.

statistical uncertainty is 9.3 GeV, with 76% of events falling below the observed uncertainty of 10.7 GeV.

8.2 Systematic Uncertainties

Uncertainties in measurements of jet and lepton momenta as well as in the overall jet energy within an event lead to systematic uncertainties in the top quark mass measurement. Variations in jet multiplicity, template shape, and parton distribution functions (PDFs) used in event generation create additional uncertainties. Each of these variations is evaluated in turn, and an overall systematic uncertainty is defined by adding the individual uncertainties in quadrature.

8.2.1 Jet Energy Scale

Miscalibrated jets within an event can create significant shifts in the measured top mass. There are four known factors which contribute to jet mismeasurement:

- a 3.4% uncertainty in jet energies for light quark jets,
- an additional 2.1% uncertainty in jet energies from b quarks,
- a 1% uncertainty due to the p_T dependence of jet energies,
- and a 1.4% uncertainty from differences in η-dependent corrections between data and Monte Carlo[59][46].

These factors produce a combined uncertainty of $\sigma = 4.4\%$ on the jet energies.

To evaluate the effect of this uncertainty on the mass measurement, event selection is repeated over all Monte Carlo samples in each dilepton channel, with jets with the samples shifted by $\pm 1\sigma$ prior to event selection. New event weight templates are generated from events with these revised jet energies, and sample ensembles are created from the new templates. Likelihood fits are made by comparing the new ensembles to the original Monte

Carlo templates. These fits are repeated for 1000 ensembles in the combined dilepton channels. Differences between the new fits and the original fit are used to estimate the uncertainty from the change in jet energy scale. Figure 8.5 shows that, for an input mass of 176.4 GeV, jets shifted by $+1\sigma$ increase the value of the output minimum by 3.8 GeV, while jets shifted by -1σ decrease the output minimum by 5.3 GeV. The larger of the two errors is taken as the uncertainty due to jet energy scale effects.

8.2.2 Jet and Lepton Resolution

The uncertainty in jet energy due to the finite resolution of the calorimeter is described by Equation 4.5. The effect of this uncertainty on the mass measurement is found by generating templates from Monte Carlo samples in which the jet resolutions have been smeared by $\pm 1\sigma$ from their default values. Such samples only exist for m_{top}=175 GeV. Results from likelihood fits to 1000 ensembles made from these revised samples are compared with those from the original samples. As with the jet energy systematic, differences between the two results are used as an estimate of systematic uncertainty. The larger of the difference between the original and $\pm 1\sigma$ samples is found to be 0.5 ± 0.3 GeV, as shown in Table 8.1. This value is taken as the uncertainty due to jet energy resolution.

Muon resolution is described in Chapter 4.3. The uncertainty due to muon resolution is calculated in much the same way as the uncertainty from jet resolutions. However, unlike the case for jets, no Monte Carlo samples exist in which the muons are smeared by any value other than their default resolutions. This smearing is applied to all Monte Carlo muons.

In order to estimate the effect of different muon resolutions on top quark mass, an "oversmeared" event sample is produced in which muons are re-smeared by their original resolutions. This sample is compared to samples in which muons are re-smeared by resolutions of $\pm 1\sigma$ of their original values. Comparisons are made from 1000 ensemble tests at $m_{top} = 175$ GeV for the new samples via likelihood fits. The maximal difference

TABLE 8.1. Likelihood fit minima for smeared jet and muon samples at $m_{top} = 175$ GeV.

Jets		Muons	
Smearing	Likelihood Minimum (GeV)	Smearing	Likelihood Minimum (GeV)
No Jet Smearing	177.4 ± 0.3	Default Muon Smearing	177.4 ± 0.3
Jet Res. +1σ	177.9 ± 0.3	Oversmeared	176.9 ± 0.3
Jet Res. -1σ	177.1 ± 0.3	Oversmeared +1σ	176.9 ± 0.3
		Oversmeared -1σ	176.5 ± 0.3

of 0.4 GeV between samples is taken as the systematic uncertainty due to the finite muon resolution.

The results of ensemble tests on summarized jets and muons are given in Table 8.1. Uncertainties in electron momentum resolution are far smaller than for either jets or muons. The effect of such uncertainties on the measured top quark mass is thus expected to be negligible relative to effects already mentioned, and is not evaluated directly.

8.2.3 $t\bar{t}$ + Jet Events

Gluon radiation in a $t\bar{t}$ decay can result in a final state with more than two high-p_T jets. It is expected that 32% of $t\bar{t}$ events will contain one such extra jet, while 8% will contain two extra jets. As this analysis assumes that the two highest-p_T jets in an event are produced by b quarks, this can lead to a gluon jet being treated as a b jet within the event selection and weight generation processes.

A Monte Carlo "$t\bar{t}$+1 jet" sample at $m_{top} = 175$ GeV has been produced which contains one extra jet per event. The effects of this extra jet on the mass measurement is evaluated as with all the previous systematics: event weight ensembles are generated from the new sample and are compared to the original templates via the likelihood fit. The result of this comparison is shown in Table 8.2. The difference of 4.1 GeV between the minima is scaled by 32%, resulting in an uncertainty of 1.3 GeV due to events with one extra jet.

TABLE 8.2. Likelihood fit minima for $t\bar{t}$ and $t\bar{t}$ + 1 jet samples at $m_{top} = 175$ GeV.

Process	Likelihood Minimum (GeV)
$t\bar{t}$ + 0 jets	175.4 ± 0.3 GeV
$t\bar{t}$ + 1 jet	179.5 ± 0.3 GeV

There is no Monte Carlo sample for events with two extra jets. To estimate this systematic, it is assumed that the effect of the second extra jet is to double the fraction of events in which at least one gluon jet is identified as coming from a b quark. It is further assumed that increasing this fraction leads to a doubling of the 4.1 GeV difference between the original and extra-jet templates. The resulting difference is scaled by 8%, giving an uncertainty of 0.7 GeV. This is added to the 1-jet uncertainty to give an overall systematic of 2.0 GeV.

8.2.4 Event Parton Distribution Functions

As mentioned in Chapter 4.1, the parton distributions in Monte Carlo are determined by the CTEQ5 parameterization. This calculates parton structure functions from a phenomenological fit of data from deep inelastic scattering, W boson production, Drell-Yan experiments, and collider data. Other fits to this data also exist [60]. Variations in PDFs may contribute to additional uncertainties in the measurement of the top quark mass.

To account for these uncertainties, PYTHIA samples are created for $t\bar{t} \rightarrow e\mu$ decays for a number of leading-order and next-to-leading-order PDF parameterizations. Samples are generated at $m_{top} = 175$ GeV in the $e\mu$ channel, and a simplified selection scheme is introduced by cutting on jet and lepton energy as well as $\not{E}_T$. Events that pass these cuts are used to form ensembles that are compared to the default Monte Carlo templates. One hundred ensemble tests of 15 events each are performed, and the uncertainty in the $e\mu$ channel is taken as half the difference between the largest and smallest fit minima (see Table 8.3). Since samples don't exist for the ee and $\mu\mu$ channels, the uncertainty in the overall measurement is found by scaling the $e\mu$ error up by the square root of the ratio of

TABLE 8.3. Likelihood fitter minima for various PDF samples for $e\mu$ events at $m_{top} =$ 175 GeV.

PDF	Likelihood Minimum (GeV)
MRST(c-g) LO	173.4 ± 0.6
MRST(h-g) LO	173.8 ± 0.6
MRST(l-g) LO	173.8 ± 0.6
MRST(l-a_s) LO	173.4 ± 0.7
MRST(h-a_s) LO	174.0 ± 0.5
MRST(h-t) NLO	174.7 ± 0.7
CTEQ5M MS NLO	173.6 ± 0.7

the total number of events and the $e\mu$ total, $\sqrt{21/15}$. The overall uncertainty is found to be 0.7 GeV.

8.2.5 Template Statistics

The finite statistics of the event templates lead to an uncertainty in likelihood values, as noted in Chapter 7.3. This leads to an uncertainty in the exact position of the likelihood fit minimum. This uncertainty is evaluated in much the same manner as for the likelihood points themselves. Each Monte Carlo template is split into smaller sub-templates, and ensembles of dilepton events are fit to each of the sub-templates. Variations in fit minima across the sub-templates provide an estimate of the template uncertainty.

Thirty ensemble tests were performed for sets of 21 dilepton events. Templates were broken into 3 sub-templates, and the uncertainty in fit minimum was found to be 0.9 GeV. Repeated tests using 5 and 10 sub-templates yielded uncertainties of 0.9 GeV and 1.0 GeV, respectively. The overall uncertainty is taken as the average of these results, 0.9 GeV.

8.2.6 Background Shape

The low number of background events that pass selection cuts leads to background templates containing only a few dozen events. The shape of these templates is thus less well

understood than is the shape of the signal templates, which contain upwards of one thousand events. High-statistics background templates may be created with the PMCS simulator discussed in Chapter 4.1. The agreement between event kinematic variables in PMCS and the default Monte Carlo is not strong enough for the PMCS background samples to be used in place of the original templates. However, ensembles tests using PMCS samples may be compared to the original ensemble tests to get an estimate of the effect of the low-statistics background templates on the fit mass.

As a cross check, additional ensemble tests are performed using crude "dummy" background event weight templates in place of the original background samples. Each event weight within a dummy background is generated from a gaussian distribution from 10,000 random numbers. The widths of the event weights vary randomly from 20 to 60 GeV, and peaks are chosen between 170 and 210 GeV. These values are chosen to mimic the means and widths seen in the original Monte Carlo backgrounds. The values are tuned for each dummy background so that the mean and width of the new template matches that of the Monte Carlo background.

The results of likelihood fits to PMCS and dummy backgrounds are shown in Figure 8.6, along with the fit to the original templates. At the measured fit minimum, the PMCS fit differs from the fit using the Monte Carlo background templates by 1.3 GeV, while the dummy fit differs by 2.3 GeV. These small errors, even with the dummy backgrounds, illustrate the relative insensitivity of the likelihood fitter to fluctuations within the background templates. As the PMCS templates are expected to be the more accurate representations of the background processes, the PMCS fit difference is taken as the systematic uncertainty on the background shape.

8.2.7 Dielectron Trigger Efficiency

In the selection code for Monte Carlo events in the $e\mu$ and $\mu\mu$ channels, trigger efficiencies are simulated from efficiencies derived with data in those channels. No such modeling

is performed in the *ee* Monte Carlo event selection, which means that the Monte Carlo treats the *ee* triggers as 100% efficient. Since the triggers tend not to be fully efficient at the electron momentum selection cut of 15 GeV, the events selected from Monte Carlo samples contain a larger fraction of low-p_T electrons than events selected from data.

This effect is taken into account by modeling the ELE_NLV(1,20) trigger on each electron in a 175-GeV Monte Carlo sample. The turn-on curve for this trigger has the strongest p_T dependence of any electron trigger, as described in [61]. Events are randomly discarded based on the efficiency of the trigger relative to the p_T of each electron within the event. Once again, ensemble tests are used to compare events passing the simulated trigger to events from the original Monte Carlo.

The variance in output mass between this sample and a sample without the simulated trigger is found to be 0.4 GeV. This is the variance that would be expected if all events were selected with the ELE_NLV(1,20) trigger. Since other triggers are used in selecting dielectron events, and since all the other triggers depend less strongly on p_T than does ELE_NLV(1,20), the overall effect on the measured mass from dielectron trigger efficiency is assumed to be negligible.

8.3 Final Result of Mass Measurement

The measured top quark mass from 21 dilepton events is 175.6 GeV. The statistical uncertainty on this measurement is 10.7 GeV. The systematic uncertainties are summarized in Table 8.4. The total systematic error is 6.0 GeV.

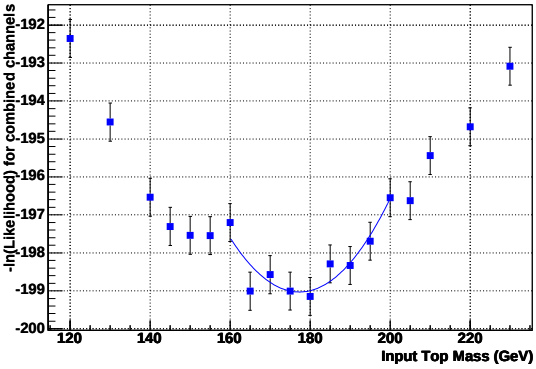

FIGURE 8.2. -ln (Likelihood) minima versus mass in data for the combined dilepton channels.

TABLE 8.4. Summary of systematic errors.

Source	Uncertainty (GeV)
Jet Energy Scale	± 5.3
Jet Resolution	± 0.5
Muon Resolution	± 0.4
$t\bar{t}$+jets	± 2.0
PDF variation	± 0.7
Template Fit Statistics	± 0.9
Background Template Shape	± 1.3
Total Systematic Error	± 6.0

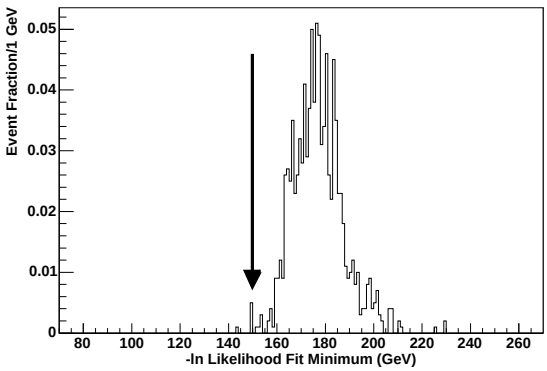

(a) $e\mu$

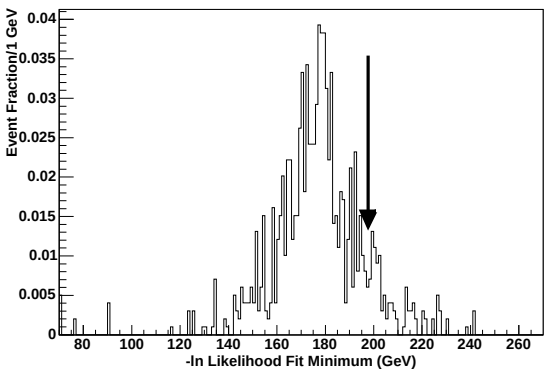

(b) ee

FIGURE 8.3. Distributions of fit minima from 1000 Monte Carlo ensemble tests in the (a) $e\mu$ and (b) ee channels at $m_{top} = 175$ GeV. The arrows indicate the minima observed from data.

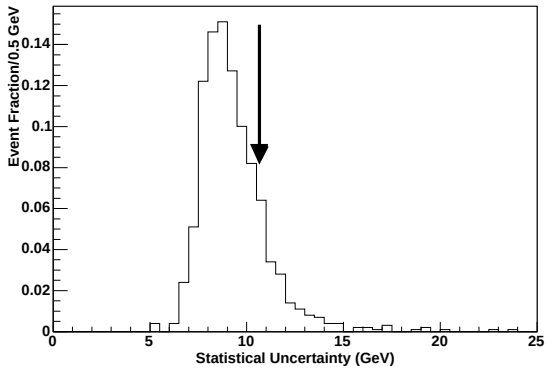

FIGURE 8.4. Distribution of statistical uncertainties from 1000 Monte Carlo tests on combined dilepton ensembles at $m_{top} = 175$ GeV. The arrows indicates the uncertainty observed from data.

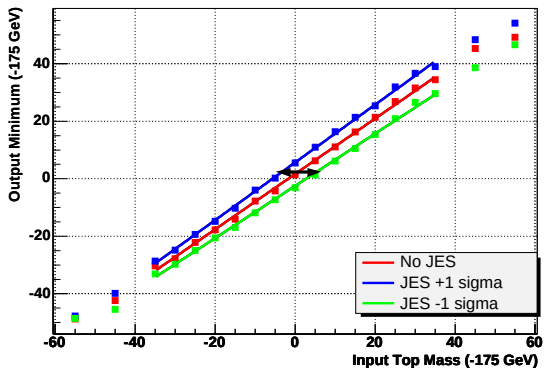

FIGURE 8.5. Likelihood minima versus top quark mass for unsmeared events, and for events in which jet energies have been shifted by $\pm 4.4\%$.

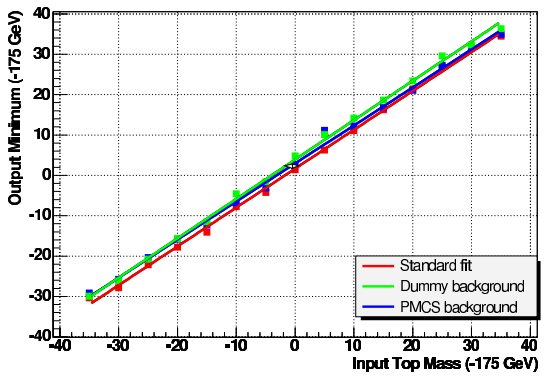

FIGURE 8.6. Likelihood minima vs. m_{top} using standard, PMCS, and dummy background templates.

CHAPTER 9
CONCLUSION

The mass of the top quark was first measured during Run I of the Tevatron, soon after the particle was discovered. Measurements made at the time by the CDF and DØ collaborations indicated that the top quark is by far the heaviest of the known elementary particles, with a mass in excess of 170 GeV. Enhancements in the number and energy of proton-antiproton collisions during Run II of the Tevatron allow this mass to be measured with much less statistical uncertainty than in Run I. This thesis provides a measurement of the top quark mass from "dilepton" decays of $t\bar{t}$ pairs, in which each top quark decays to a b quark and a W boson, and in which each W in turn decays to a lepton and a neutrino. Events are categorized as either ee, $e\mu$, or $\mu\mu$, depending on the flavor of the produced leptons.

Such events are selected from data collected at the DØ detector by searching for their decay signatures – two high-momentum jets from the b quarks, two high-momentum leptons from the W bosons, and a large imbalance in measured energy within the event due to the neutrinos. Selection criteria are applied to efficiently pick $t\bar{t}$ events from data while simultaneously reducing background events that mimic this decay signature. After applying these criteria to approximately 360 pb^{-1} of data collected between April 2002 and August 2004, a total of 5 ee, 15 $e\mu$, and 1 $\mu\mu$ candidate events remain.

The two undetected neutrinos within each dilepton decay prevent the top quark mass from being reconstructed directly from observed kinematic variables. Instead, the mass of the top quark is assumed, along with the rapidity of each neutrino. A weight is assigned to each assumption based on the agreement of the calculated momentum of the neutrino pair and the observed energy imbalance within the event. A range of assumed top quark masses from 80 GeV to 330 GeV are explored, with multiple rapidity assumptions for each mass assumption. The resulting distributions of event weights versus assumed top quark mass

provide a means of extracting mass information from an event.

The top quark mass is measured by comparing the event weight distributions of the 21 events in data with distributions generated from Monte Carlo samples of $t\bar{t}$ decays for assumed top quark masses between 120 GeV and 230 GeV. Data distributions are also compared to event weights generated for background processes in each of the dilepton decay channels. A likelihood fit is performed to determine the top quark mass from these distributions.

The top quark mass is measured from the 21 dilepton decays to be $175.6 \pm 10.7(\text{stat.}) \pm 6.0(\text{syst.})$ GeV. This result agrees well with the mass of 168.4 ± 12.8 GeV measured on dilepton events in Run I at DØ, while improving on the uncertainty of the Run I measurement. The new result has been combined with a complementary analysis [63] and with events from orthogonal dilepton selection criteria [64] to produce a measured DØ Run II top quark mass of 178.1 ± 8.3 GeV in the dilepton decay channel [62]. The combined result, like the result from the neutrino weighting analysis described in this document, is in good agreement with measurements in other $t\bar{t}$ decay channels, and is used in calculating the current overall world average of the top quark mass as 171.4 ± 2.1 GeV (see Figure 9.1).

The Run II dataset continues to expand. As of October, 2006, more than 1.6 fb^{-1} of data has been collected at DØ, as shown in Figure 9.2. This represents a quadrupling of the dataset used in this analysis. The statistical uncertainty on mass measurements from this new dataset can be expected to decrease by a factor of two, yielding a dilepton-channel measurement in which statistical and systematic uncertainties will be comparable.

As data accumulates further, more work will need to be done to reduce the systematic uncertainties in the measurement. Such efforts have already been undertaken to improve the uncertainty on the jet energy scale, the dominant systematic in this analysis. The increased data yield has allowed for more precise measurements of the response and showering corrections applied to jet energies, as described in Chapter 4.2.3. The uncertainty in jet energies has been reduced from 4.4% to 3% for energies above 20 GeV, and it is expected

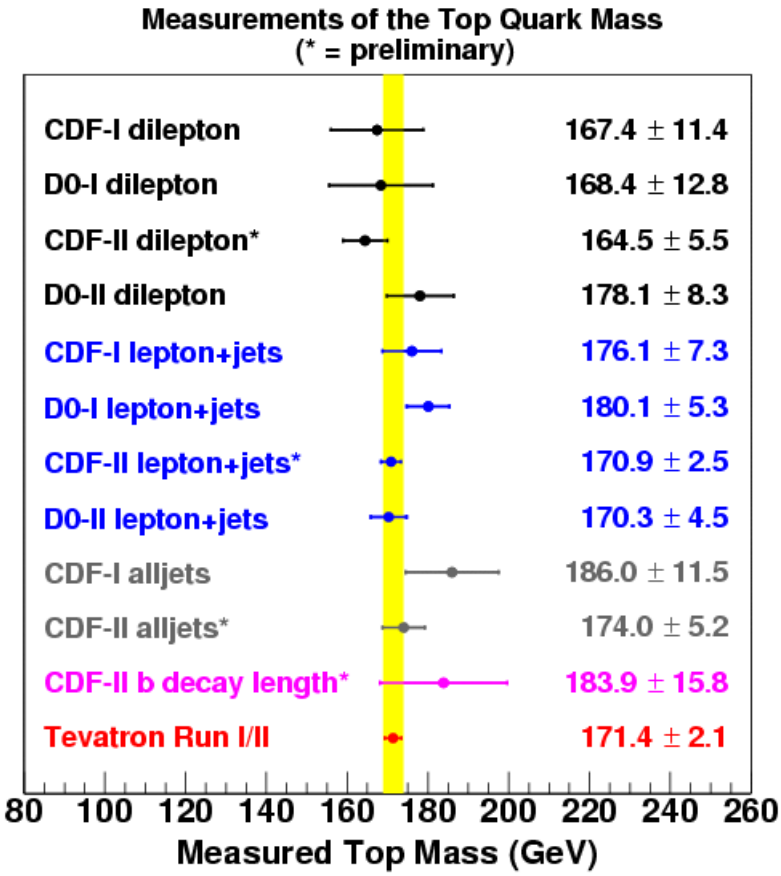

FIGURE 9.1. World average of m_{top}, from measurements at DØ and CDF.

that this uncertainty will eventually drop to under 1% [65].

Analysis on a 1 fb^{-1} dataset has already begun for the $e\mu$ channel, using the neutrino-weighting methods described in Chapters 6-7 [66]. The new analysis revises the existing template-generation scheme in an attempt to reduce the dimensionality of the templates and simplify the PDE calculations. Higher-order polynomial fits to likelihood minima are also being explored. A preliminary measurement on this expanded data set in the $e\mu$ decay channel yields a result of $173.6 \pm 6.7(\text{stat.})^{+5.1}_{-4.0}(\text{syst.})$ GeV. For the first time, a dilepton-channel mass measurement limited by systematic uncertainties, rather than statistics, is within reach. It is hoped (and expected) that the further improvements on the neutrino-weighting method will lead to ever more precise measurements of the top quark mass.

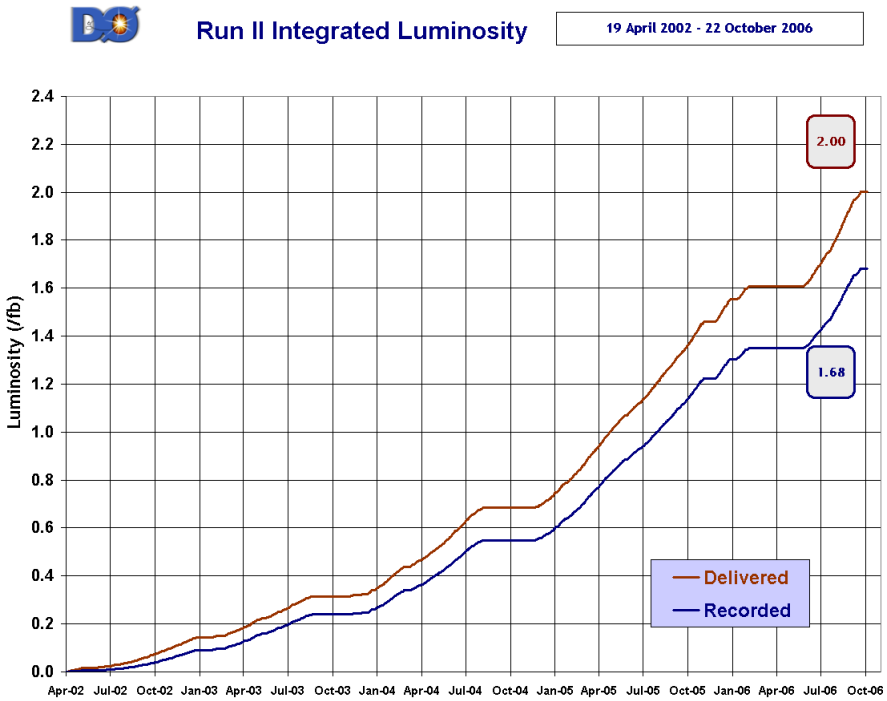

FIGURE 9.2. Recorded luminosity at DØ versus time

APPENDIX A
LEPTON TRIGGERS USED IN THE ANALYSIS

Data in this analysis were collected from a constantly evolving set of triggers, spanning versions 8-13 of the DØ trigger list. Although the triggers changed over time, they share certain commonalities. For instance, all Level 1 muon triggers require hits in two layers of muon scintillators, while all Level 1 electron triggers require towers above a threshold energy in the EM calorimeter. The requirements for all triggers used in this analysis are documented below.

A.1 Muon Triggers

Muons in this analysis are required to fire the so-called "tight scintillator" (or *mu1ptxatxx*) Level 1 trigger. This trigger fires when hits are present in layers of the muon scintillator system both inside and outside the muon toroid. In the forward region of the detector, only A- and B-layer pixels are used for triggering purposes. Hits in the B-layer are projected back to the A-layer, and the *mu1ptxatxx* trigger fires only if the B-layer hit is within one pixel in η or ϕ of an A-layer hit. In the central region, either B-layer or C-layer hits can be matched to an A-layer scintillator. Since the B- and C-layer scintillators span different regions in η and ϕ than the A-layer, the matching between layers is more complicated than in the forward region. Matching roads between layers are formed from detector hit distributions of samples of 4 GeV Monte Carlo muons. Hits that fall within these roads cause the *mu1ptxatxx* trigger to fire.

Dimuon triggers are formed by searching for two or more *mu1ptxatxx* triggers within an event. Two *mu1ptxatxx* triggers can fire a dimuon trigger provided that the A-layer hits for the triggers are separated in η and ϕ by at least two scintillators. The dimuon trigger is denoted *mu2ptxatxx*.

The *mu1ptxatxx* trigger allows for hits within the fiducial area of the muon system ($|\eta| < 2.0$). Other Level 1 muon triggers are formed from muon hits within the η coverage of the CFT. The single muon and dimuon version of these triggers are denoted *mu1ptxwtxx* and *mu2ptxwtxx*, respectively. Other Level 1 muon triggers make use of tracks found in the CFT and muon wire chamber hits. These triggers are not used in this analysis, but are detailed in [67].

Level 2 muon triggers are satisfied if at least one muon of medium quality is reconstructed at Level 2. Although the Level 2 triggers have the capability of imposing a cut on muon p_T, such cuts are not used for the triggers in this analysis. Level 3 triggers require at least one reconstructed muon of medium quality, and may also require a minimum p_T or central track match for that muon. Exact muon trigger requirements for each trigger list version are given in Tables A.1 and A.3.

A.2 Electron Triggers

Level 1 electron triggers are formed based on the energy and number of towers found within the EM calorimeter. Three distinct types of Level 1 electron triggers are used in this analysis:

- **CEM(1,X)** This trigger fires if at least one EM tower with transverse energy $>$ X GeV is present.
- **CEM(2,X)** This trigger fires if at least two EM towers are present. Each tower must contain at least X GeV of transverse energy.
- **CEM(3,3)** This trigger fires if at least two EM towers with at least 3 GeV of transverse energy are present. Additionally, at least one tower must have transverse energy greater than 9 GeV.

Level 2 electron triggers are formed from the energy of individual towers as well as the combined energy from towers within an event. Additional triggers may be formed by

summing energies of a seed tower and neighboring towers. Level 3 triggers require at least one reconstructed electron, and may require a minimum E_T for that electron. Some Level 3 triggers also require that the electron meets shower shape requirements. The Level 3 electron triggers used in this analysis are:

- **1LX** One loose reconstructed electron with $E_T >$X GeV.
- **2LX** Two loose electrons, each with $E_T >$X GeV.
- **SHX** One loose electron with $E_T >$X GeV that passes a loose shower shape cut.
- **2SHX** Two loose electrons, each with $E_T >$X GeV and passing a loose shower shape cut.
- **SHTX** One loose electron with $E_T >$X GeV that passes a tight shower shape cut.
- **RD5** One electron reconstructed with the road method [68], a method for finding electrons within jets. The electron must satisfy $0.6 < E/p < 1.05$ with tight requirements, and must have a matching track of at least 5 GeV.

Electron triggers used in the *ee* and $e\mu$ channels are listed in Tables A.2 and A.3.

TABLE A.1. Dimuon trigger requirements for each trigger list version

Trigger List Version	Level 1 Condition	Level 2 Condition	Level 3 Condition
v8-v10	mu2ptxatxx	$\geq$1 medium muon	*None*
v11	mu2ptxatxx	$\geq$1 medium muon	$\geq$1 track $>$10 GeV -OR- $\geq$1 loose muon, $p_T > 15$GeV
v12-v13	mu2ptxatxx	$\geq$1 medium muon	$\geq$1 track $>$5 GeV -OR- $\geq$1 loose muon, $p_T > 6$GeV

TABLE A.2. Dielectron trigger requirements for each trigger list version

Trigger List Version	Level 1 Condition	Level 2 Condition	Level 3 Condition
v8-v11	CEM(2,10)		1L20
v12	CEM(1,11) -OR- CEM(2,6) -OR- CEM(3,3)	total E_T of two leading towers $>$ 18 GeV	2L20 -OR- SH15
v13.0-v13.1	CEM(1,11) -OR- CEM(2,6) -OR- CEM(3,3)	total E_T of two leading towers $>$ 18 GeV	2L20 -OR- 2SH8 -OR- 2L15 + SH15
v13.0-v13.1	CEM(1,11) -OR- CEM(2,6) -OR- CEM(3,3)	total E_T of two leading towers $>$ 18 GeV	2L20 -OR- 2SH10 -OR- 2L15 + SH15

TABLE A.3. Electron-muon trigger requirements for each trigger list version

Trigger List Version	Level 1 Condition	Level 2 Condition	Level 3 Condition
v8.0-v8.4	mu1ptxwtxx + CEM(1,5)		1L10
v8.4-11	mu1ptxatxx + CEM(1,5)		1L10
v12	mu1ptxatxx + CEM(1,6)		1L12
v13	mu1ptxatxx + CEM(1,6)	$\geq$1 medium muon	SHT7 -OR- 1L12 -OR- RD5

APPENDIX B
ALGEBRAIC SOLUTION FOR NEUTRINO RAPIDITY

The neutrino weighting scheme outlined in Chapter 6 relies on calculating the momentum of each neutrino from momentum measurements of the b quarks and leptons in each $t\bar{t}$ decay. Values of m_{top} and $\eta_{neutrino}$ must be also be assumed. These assumptions yield a solution for neutrino momentum that is quadratic in nature, as in shown below.

A schematic of a top quark decay is shown in Figure B.1. Each particle i is described by a four-vector $p_i = (E_i, \vec{p}_i)$, with a mass given by $m_i^2 = p_i^2$. Conservation of energy and momentum implies that

$$p_{top} = (p_b + p_\ell + p_\nu) \tag{B.1}$$

and

$$p_W = (p_\ell + p_\nu). \tag{B.2}$$

Assuming that the neutrino is massless, squaring Equations B.1 and B.2 yields

$$p_\ell p_\nu + p_b p_\nu = \frac{m_{top}^2 - m_b^2 - m_\ell^2 - 2p_\ell p_b}{2} \tag{B.3}$$

and

$$2p_\ell p_\nu = m_W^2 - m_\ell^2, \tag{B.4}$$

respectively. Combining Equations B.3 and B.4 gives

$$2p_b p_\nu = m_{top}^2 - m_b^2 - m_W^2 - 2p_\ell p_b. \tag{B.5}$$

The products $p_b p_\nu$ and $p_\ell p_\nu$ can thus be expressed as:

$$p_b p_\nu = \frac{m_{top}^2 - m_b^2 - m_W^2}{2} \equiv \alpha_1, \tag{B.6}$$

and

$$p_\ell p_\nu = \frac{m_W^2 - m_\ell^2}{2} \equiv \alpha_2. \tag{B.7}$$

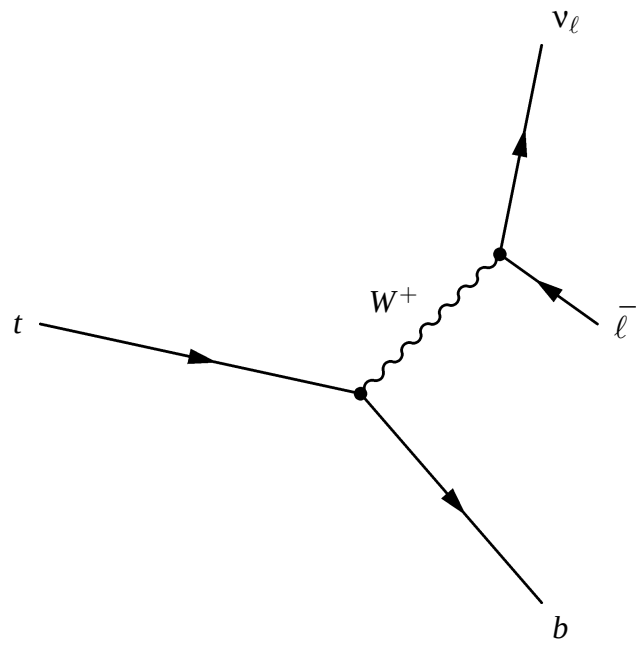

FIGURE B.1. Top decay with a lepton final product.

Expanding the dot products on the left-hand side of Equations B.6 and B.7 and using the relations

$$E = p_T sinh\eta \tag{B.8}$$

$$p_z = p_T cosh\eta \tag{B.9}$$

yields:

$$E_b p_{T_\nu} sinh\eta - p_{b_z} p_{T_\nu} cosh\eta - \alpha_1 = p_{x_b} p_{x_\nu} + p_{y_b} p_{y_\nu} \tag{B.10}$$

$$E_\ell p_{T_\nu} sinh\eta - p_{\ell_z} p_{T_\nu} cosh\eta - \alpha_2 = p_{x_\ell} p_{x_\nu} + p_{y_\ell} p_{y_\nu}. \tag{B.11}$$

When both equations are solved for p_{T_ν}, the result is:

$$p_{T_\nu} = (\frac{p_{x_b}}{E_b sinh\eta - p_{b_z} cosh\eta}) p_{x_\nu} + (\frac{p_{y_b}}{E_b sinh\eta - p_{b_z} cosh\eta}) p_{y_\nu} + \frac{\alpha_1}{E_b sinh\eta - p_{b_z} cosh\eta} \tag{B.12}$$

$$p_{T_\nu} = (\frac{p_{x_\ell}}{E_\ell sinh\eta - p_{\ell_z} cosh\eta}) p_{x_\nu} + (\frac{p_{y_\ell}}{E_\ell sinh\eta - p_{\ell_z} cosh\eta}) p_{y_\nu} + \frac{\alpha_2}{E_\ell sinh\eta - p_{\ell_z} cosh\eta}. \tag{B.13}$$

If the following constants are defined:

$$
\begin{aligned}
A_b &\equiv \frac{p_{x_b}}{E_b sinh\eta - p_{b_z} cosh\eta} \\
B_b &\equiv \frac{p_{y_b}}{E_b sinh\eta - p_{b_z} cosh\eta} \\
C_b &\equiv \frac{\alpha_1}{E_b sinh\eta - p_{b_z} cosh\eta} \\
A_\ell &\equiv \frac{p_{x_\ell}}{E_\ell sinh\eta - p_{\ell_z} cosh\eta} \\
B_\ell &\equiv \frac{p_{y_\ell}}{E_\ell sinh\eta - p_{\ell_z} cosh\eta} \\
C_\ell &\equiv \frac{\alpha_2}{E_\ell sinh\eta - p_{\ell_z} cosh\eta},
\end{aligned}
$$

then Equations B.12 and B.13 may be expressed more simply as:

$$p_{T_\nu} = A_b p_{x_\nu} + B_b p_{x_\nu} + C_b \tag{B.14}$$

$$p_{T_\nu} = A_\ell p_{x_\nu} + B_\ell p_{x_\nu} + C_\ell. \tag{B.15}$$

Setting the right-hand sides of Equations B.14 and B.15 equal yields:

$$p_{x_\nu} = \kappa p_{y_\nu} + \varepsilon, \tag{B.16}$$

where

$$
\begin{aligned}
\kappa &\equiv \frac{B_\ell - B_b}{A_b - A_\ell} \\
\varepsilon &\equiv \frac{C_\ell - C_b}{A_b - A_\ell}.
\end{aligned}
$$

Squaring Equation B.14 and substituting B.16 produces the following quadratic equation:

$$
\begin{aligned}
0 = {} & [\kappa^2(A_b^2 - 1) + B_b^2 - 1]p_{y_\nu}^2 + \\
& [2\varepsilon\kappa(A_b^2 - 1) + 2A_b C_b \kappa + 2B_b C_b]p_{y_\nu} + \\
& [(A_b^2 - 1)\varepsilon^2 + 2\varepsilon A_b C_b + C_b^2].
\end{aligned} \tag{B.17}
$$

The coefficients in this equation depend only on $\vec{p}_b$, $\vec{p}_\ell$, and assumed values for m_{top} and η. The values chosen for m_{top} and η are described in Chapter 6. Equation B.17 yields

up to two real solutions for the momentum component p_{y_ν}. Once p_{y_ν} is determined, p_{x_ν} follows directly from Equation B.16. Thus, there may be 0, 1, or 2 real solutions per neutrino for each assumption of m_{top} and η.

APPENDIX C
LEVEL 1 MUON MONITORING TOOLS

The University of Arizona group at DØ is responsible for the construction, commissioning, and maintenance of the Run II Level 1 Muon trigger. This system forms triggers based on combinations of Central Trakc Trigger (CTT) tracks, muon scintillator hits, and muon wire chamber hits. This appendix outlines the monitoring and diagnostic tools available for the Level 1 Muon system.

C.1 Overview of the Level 1 Muon Trigger

The Level 1 Muon system consists of three regional trigger crates, which form trigger hits in the central, north, and south regions of the detector. (Here, "central" is defined as $-1.0 < \eta < 1.0$, "north" is defined as $1.0 < \eta < 2.0$, and "south" is defined as $-2.0 < \eta < -1.0$.) Each regional crate contains eight "MTC05" trigger cards, which form octant-level triggers based on combinations of scintillator hits and CTT tracks, and eight "MTC10" cards, which form triggers from combinations of scintillators and wire hits. Decisions from these sixteen cards are combined into regional decisions in each crate at the Muon Trigger Crate Manager (MTCM). The MTCM decisions are in turn combined into a global trigger by the Muon Trigger Manager (MTM). The MTM also contains an MTCM, and communicates the global trigger decisions to the Trigger Framework. A schematic of the Level 1 Muon trigger is shown in Figure C.1.

C.2 Level 1 Muon Monitoring

A number of real-time and long-term monitoring tools have been developed for the Level 1 Muon system. The real-time tools are used by CalMuon (Calorimeter+Muon) shifters and

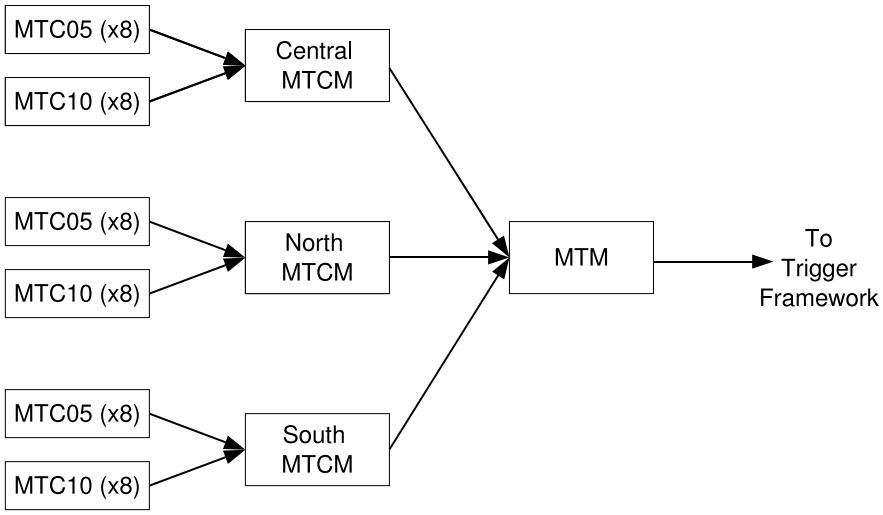

FIGURE C.1. The Level 1 Muon Trigger system.

Shift Captains in the DØ control room for constant monitoring of the system. Long-term tools are used by Level 1 Muon experts for daily and weekly checks of trigger performance, and for diagnostic purposes when there are problems with the system. The available tools are outlined below.

C.2.1 Real-Time Monitoring Tools

The real-time monitoring tools are designed to identify major problems with the Level 1 Muon system, and to alert non-expert shifters to the possible causes of such problems. There are four such tools in current use:

- **Power Supply Monitoring** The status of the low voltage supplies providing power to the Level 1 Muon regional crates is monitored by the CalMuon shifter, via an online Graphical User Interface (*GUI*) located at: */projects/l1muo/REGmonitor/CrateMonitor*. This allows for monitoring of voltages, currents, and temperatures of all the supplies powering Level 1 Muon (Figure C.2). Supply trips are reported to shifters automatically via the Significant Event System [69], which issues a run-pausing alarm until the trip is resolved. This prevents shifters from unknowingly collecting physics data

while the Level 1 Muon system is powered off.

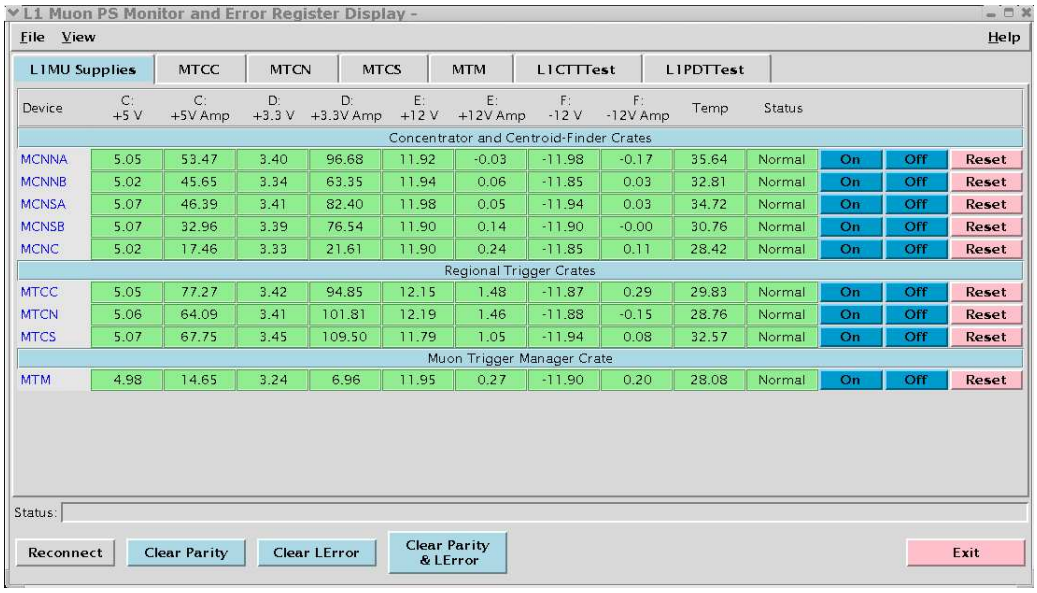

FIGURE C.2. Level 1 Muon power supply monitor.

- **Beginning-of-Turn Triggers**. Each MTC05 and MTC10 card receives input data asynchronously, and stores that data in FIFOs. When all the FIFOs on a card go to a non-empty state, a special synchronization trigger bit is set high. In normal operation, all FIFOs are emptied each turn during the sync gap, and go non-empty on the first beam crossing after the gap. Thus, the synchronization trigger bit should go high at the start of each turn; for that reason, this bit is known as the "Beginning-of-Turn" (BOT) trigger. This trigger should fire at a nominal rate of once per turn, or 47712 Hz.

  BOT triggers from all trigger cards in a region are summed with a logical AND by the regional MTCM and passed on to the MTM. These sums are formed separately for the MTC05 and MTC10 cards. The MTM in turn forms a logical AND of all regional BOT (*BOT-AND*) signals. It also forms a logical OR (*BOT-OR*) of these signals. The logical AND and logical OR triggers are sent to the trigger framework, and are monitored by the daqAI [70] system. If the either or these rates differ from

47712 Hz by more than 50 Hz, an audio alarm is sent in the control room. Since problems with muon or CTT front ends can cause the BOTs to deviate from their nominal value, a re-initialization of the serial command link (or *sclinit*) is issued along with the alarm in an attempt to re-synchronize the inputs to the Level 1 Muon system. If this fails, a second audio alarm is issued, alerting the CalMuon shifter to check for problems.

Deviations from nominal BOT rates are generally caused by one of three failure modes. In the first mode, a front end input fails to send data to Level 1 Muon. This can be caused by a power outage at the front end, an unplugged cable, or a problem with the transmitter or receiver of Level 1 Muon input data. When this problem appears, the BOT-AND signal goes to zero, as the FIFO from the problem input never receives data. In the second failure mode, a front end sends data with the wrong timing structure. This can be due to shorted or damaged cables causing glitches in the signal. This problem manifests itself by causing the BOT-OR signal to fire at a rate higher than 47712 Hz, as the problem input empties or fills its FIFO at incorrect times. Finally, accelerator clock problems or other timing issues can cause deviations in both BOT trigger rates.

The above list of problems is not exhaustive. Other issues can also cause variations in BOT rates. For this reason, the BOT trigger rates are the first things checked by shifters and experts. The triggers formed by the Level 1 Muon system cannot be trusted unless the BOT triggers are also firing correctly.

- **Trigger Examine Plots** Event data from a representative fraction of events collected during a physics run are collected and plotted into histograms with Trigger Examine, an online tool run by the Shift Captain. This tool plots distributions for a variety of triggers, including the Level 1 Muon octant-level triggers. Plots are made for three different trigger types: scintillator triggers, wire triggers, and BOTs. An example of these plots appears in Figure C.3. Shift Captains can check for problems in Level 1

Muon by comparing these plots to template distributions. A full description of the plots is available at:

`http://www-clued0.fnal.gov/~jtemple/L1MU_GM_Plots.html`

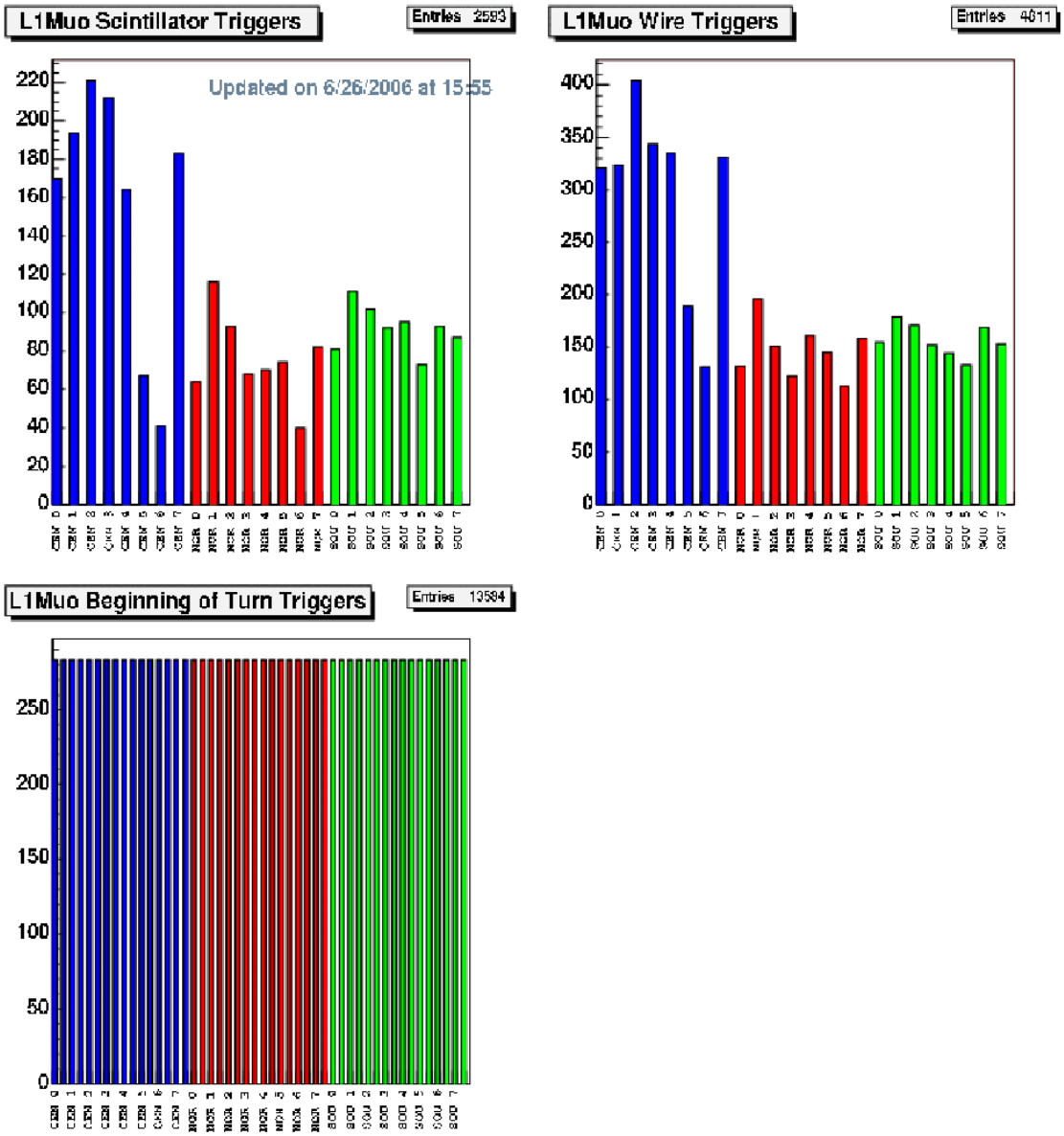

FIGURE C.3. Trigger Examine plots. Central triggers are in blue, north triggers are in red, and south triggers are in green.

- **Tight Scintillator Rates** CalMuon shifters constantly monitor two specific muon triggers: mu1ptxctxx and mu1ptxbtxx. The mu1ptxctxx trigger fires when tight scintillator hit patterns are found in the central region, while mu1ptxbtxx fires based on tight hits in the north and south. These triggers have been used throughout the course of Run II; thus, their rates as a function of luminosity are well-understood. Shifters can compare the rates against expected rates for a given luminosity at any point via an online GUI located at /projects/l1muo/ratecheck/ExpectedGUI.py. This comparison is also performed automatically whenever a CalMuon shifter completes an online checklist at the end of a physics run. Rates can very widely due to beam conditions; however, if observed rates differ by more than 20% from their expected values, a warning message is sent to the CalMuon shifter.

C.2.2 Long-Term Monitoring Tools

Additional monitoring tools exist for finding problems which affect the efficiency of the Level 1 Muon trigger, but which do not disrupt data taking. Many of these tools run automatically as "cron jobs" of the *l1muo* online account, and their output is displayed on the Level 1 Muon home page:
`http://www-d0online.fnal.gov/www/groups/l1muo`.
The list of l1muo cron jobs is kept in */projects/l1muo/cronjobs/l1muocron*. The function of each job is described below.

- **Trigger Simulator** The Level 1 Muon trigger simulator (*tsim_l1muo*) is run every hour, and uses data read from muon and CTT front ends to simulate the Level 1 Muon trigger algorithms. At the end of each hour, comparisons are made between simulated trigger decisions and hardware decisions read out from the Level 1 Muon MTCMs. Histograms are formed from these decisions with the *l1muo_analyze* package, and are displayed at:
  `http://www-d0online.fnal.gov/www/groups/l1muo/analyzeplots.html`.

This page is updated to always show plots from the past seven days of data taking, as in Figure C.4. Status pictures are generated based on the output of the histogram distributions, and appear when the cursor is rolled over the distributions on the web page. In the case where all distributions match expectations, an "A-OK" symbol is created, as in Figure C.5a. The descriptions of individual plots below detail how these matches are made for each plot.

Distributions containing discrepancies show either minor or major alert symbols, along with the pages of the offending histograms (see Figures C.5b and C.5c). In the case where the simulator crashes or the histograms cannot be generated, a "?" symbol is displayed (Figure C.5d). At the end of each day, a summary of all major and minor alerts is sent to the Level 1 Muon mailing list.

The plot files generated by *l1muo_analyze* contain detailed information about all levels of the Level 1 Muon trigger, and comprise more than 100 individual plots. Of particular importance are the following:

– **Page 1** This page contains all octant-level scintillator, wire, and BOT triggers recorded by *tsim_l1muo*, much like the Trigger Examine tool used by Shift Captains. This page also displays triggers from each CTT-based p_T threshold formed by the Level 1 Muon system in each octant For the run range used in this analysis, four p_T thresholds (1.5 GeV, 3 GeV, 5 GeV, and 10 GeV) were used for triggering. Beginning with Run IIb in June, 2006, six thresholds were used (3 GeV, 3.7 GeV, 5 GeV, 5.7 GeV, 8 GeV, and 13 GeV). Figure C.6 shows the number of triggers fired as a function of octant number and p_T threshold for a sample physics run.

  All trigger distributions are plotted along with uncertainties equal to the square root of the number of entries in each histogram bin. These error bars are not to

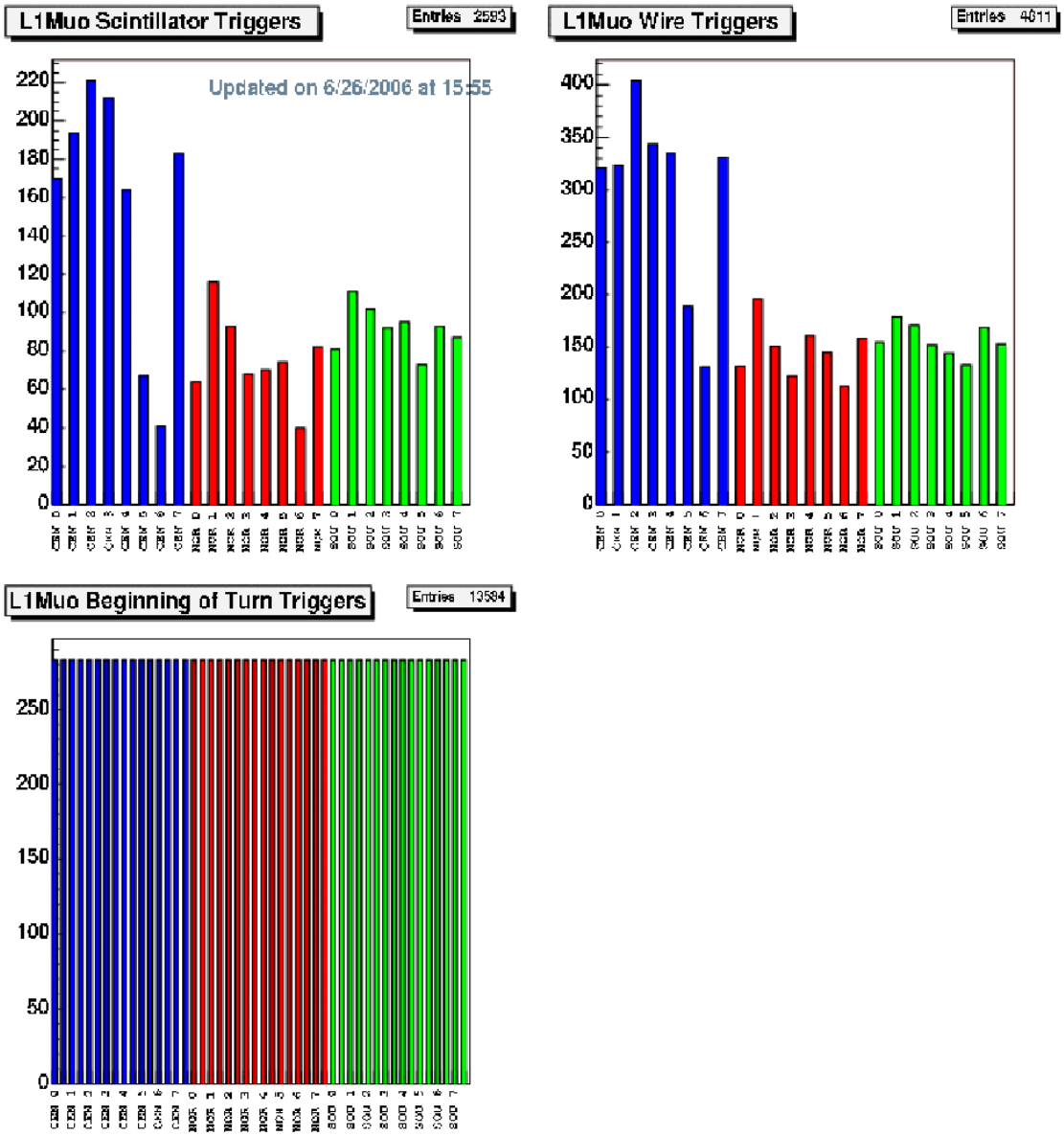

FIGURE C.4. Level 1 Muon scintillator, wire, and BOT triggers.

be taken as real estimates of uncertainties, but as a gauge of the total number of events analyzed. Sometimes special circumstances result in odd detector configurations with few data events collected; the error bars provide a visual cue for such arrangements and serve to remind the expert that remaining distributions may not match expectations.

Regardless of the status of the rest of the detector, so long as the muon systems and CTT are providing input to the Level 1 Muon trigger, all BOT values in all octants should have the same value. Any deviation in BOT from any octant causes a major alert to be issued.

– **Page 3** This plot shows fractional differences between hardware MTM triggers and triggers simulated directly from muon front end readout. This provides a complete check of the entire Level 1 Muon trigger chain. At present, only a subset of available triggers are fully simulated. The simulated triggers include: mu1ptxctxx, mu1ptxbtxx, mu1ptxatxx, mu1ptxallx, mu1ptxatlx, and mu2ptxatxx.

  As Figure C.7 illustrates, the simulation code for these triggers does not exactly match the algorithms used by the Level 1 Muon hardware. These differences are due primarily to an early bug in the counting scheme of the forward tight scintillator dimuon trigger, and to the loosening of trigger requiremens for the central loose wire trigger in central octants 5 and 6. These changes were made in the hardware algorithms, but, as of October 2006, have not been fully implemented within the simulator. Differences of up to a few percent are thus expected on this plot. Larger differences indicate a problem in either front end or Level 1 Muon hardware, and differences greater than 3.5% result in a major alert.

– **Page 6** This page shows differences from hardware MTM triggers and triggers simulated from the Level 1 Muon octant triggers. This provides a simulation of

(a) (b) (c) (d)

FIGURE C.5. Status figures for (a) good distributions, (b) minor alerts, (c) major alerts, and (d) unknown distributions.

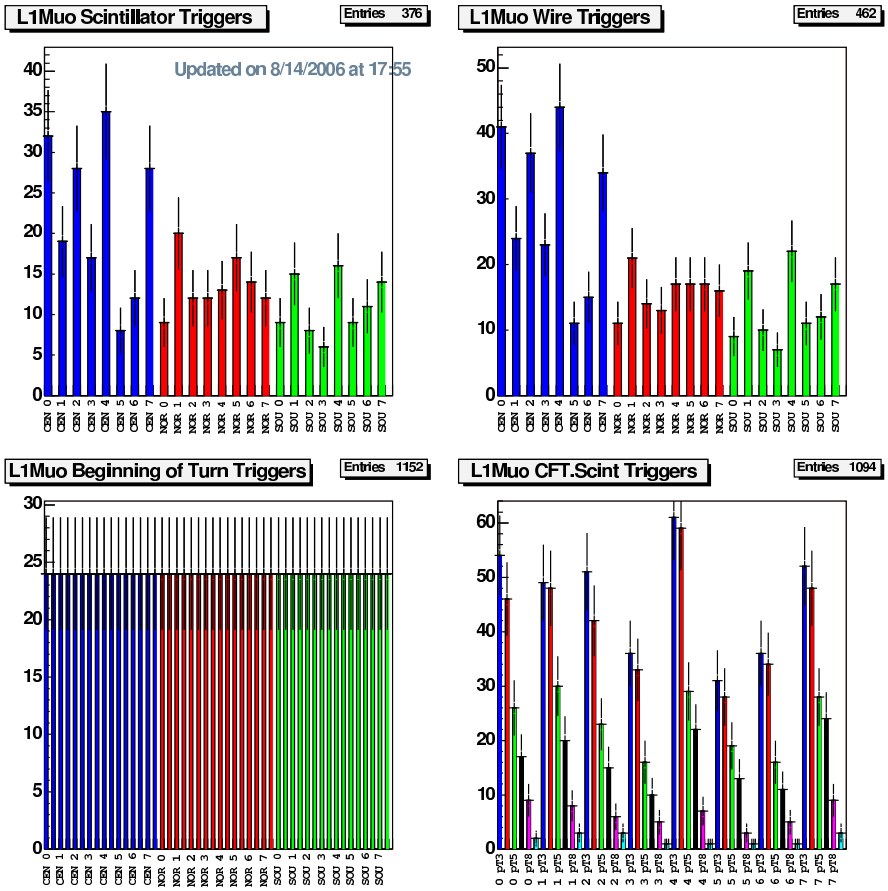

FIGURE C.6. Level 1 Muon *l1muo_analyze* plots. The plots in the upper right, upper left, and lower left mimic those produced by the Trigger Examine tool. The lower left plot shows triggers for each of the p_T thresholds in each octant of the Level 1 Muon trigger.

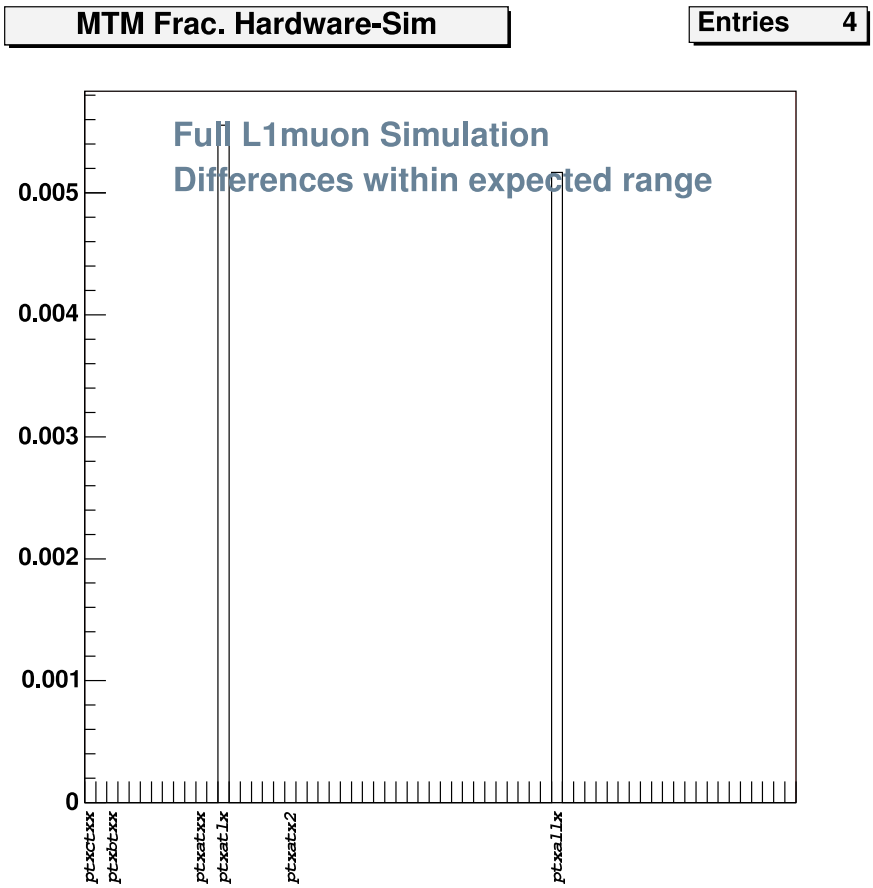

FIGURE C.7. Fractional differences between hardware MTM Triggers and triggers simulated from front end readout.

the MTCM-MTM chain. All triggers used in current trigger list are simulated in this plot. At present, there is complete agreement between hardware and simulation on all triggers (Figure C.8). Hardware trigger terms that are not part of the global physics trigger list are used for diagnostic purposes, and are plotted in gray. Because these terms may change over time, no comparison is made between them and simulated triggers. Any difference between simulated and hardware triggers causes a major alert to be issued.

– **Page 24** This page shows differences between the Level 1 Muon outputs of the TTK(1,10) track trigger and a simulated trigger formed from outputs from the Central Fiber Tracker (CFT). In principle, both systems receive the same track information, so both copies of this trigger should be identical, as in Figure C.9. Occasional differences between the two sometimes appear, at the rate of ≈ 1 per hour. Larger differences cause a major alert to be raised.

– **Pages 26-28** These plots perform consistency checks on all the pT-based Level 1 Muon triggers in the central, north, and south regions. Since each CTT-based trigger is threshold-based, the firing of any high-p_T trigger should also cause all lower-threshold triggers to fire as well. These plots test that this is indeed the case. Threshold triggers are plotted according to whether or not they correctly fire all lower-p_T triggers.

  Under normal circumstances, the histogram containing incorrect triggers should be empty, as in Figure C.10. Figure C.11 shows that firmware bugs or hardware issues occasionally can lead to entries in this histogram. This particular plot shows the results from a firmware bug in which 13-GeV triggers were not correctly propagated to the 6-GeV triggers. The firmware bug has since been fixed, but further problems occasionally arise due to hardware failures. When such problems create incorrect histogram distributions, either minor or major alerts are issued, depending on the severity of the problems.

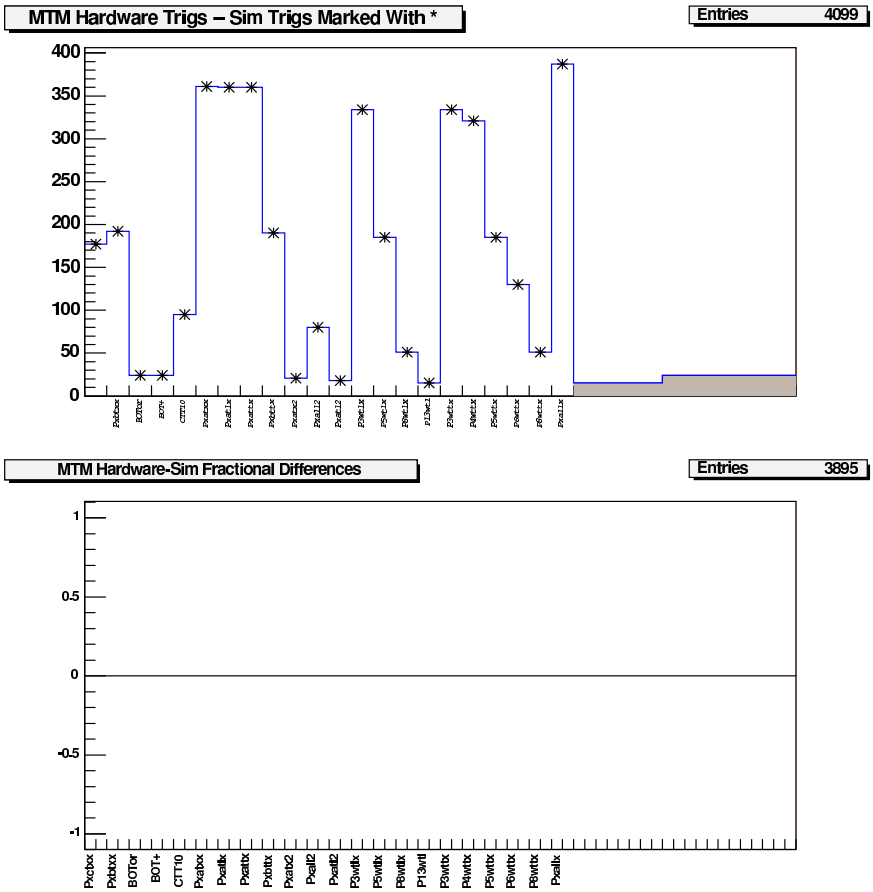

FIGURE C.8. Comparison between hardware MTM Triggers and triggers simulated from Level 1 Muon octant counters.

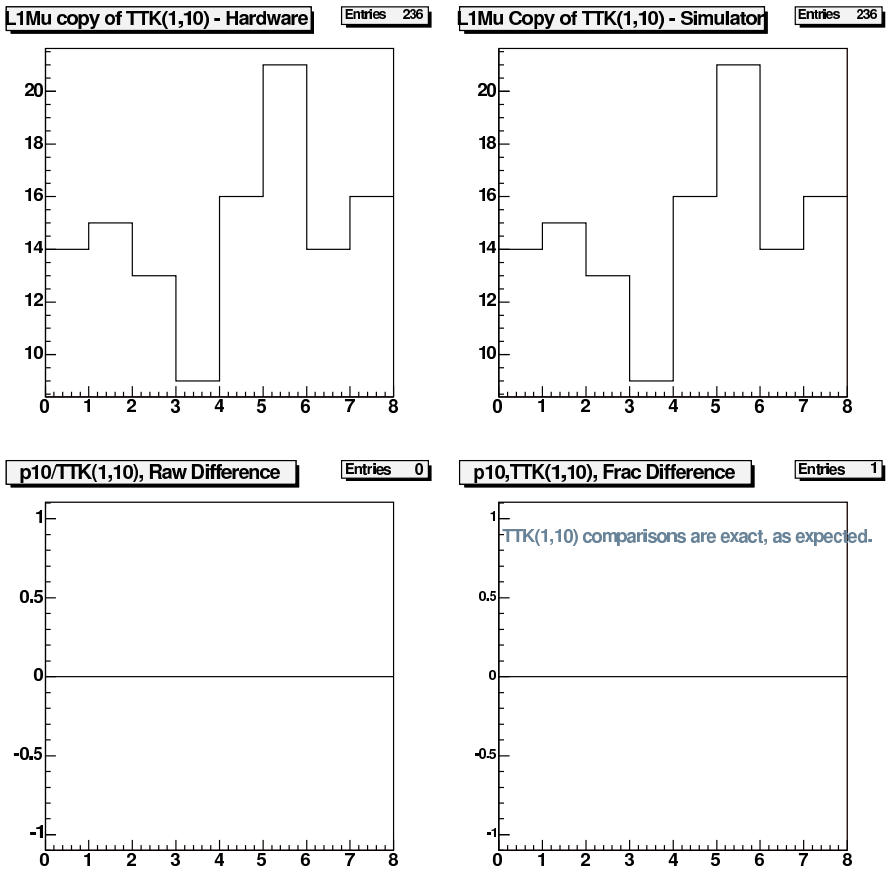

FIGURE C.9. Differences between the simulated CTT TTK(1,10) trigger and the Level 1 Muon hardware TTK(1,10) trigger.

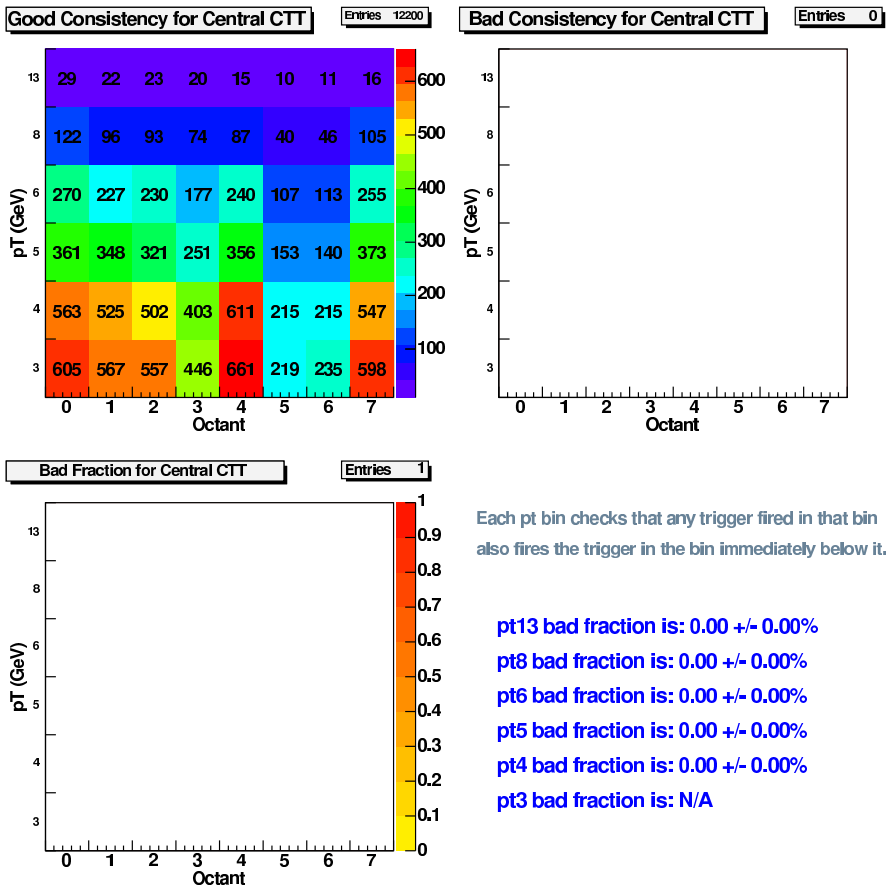

FIGURE C.10. Result of consistency check on CTT-based triggers under normal running conditions.

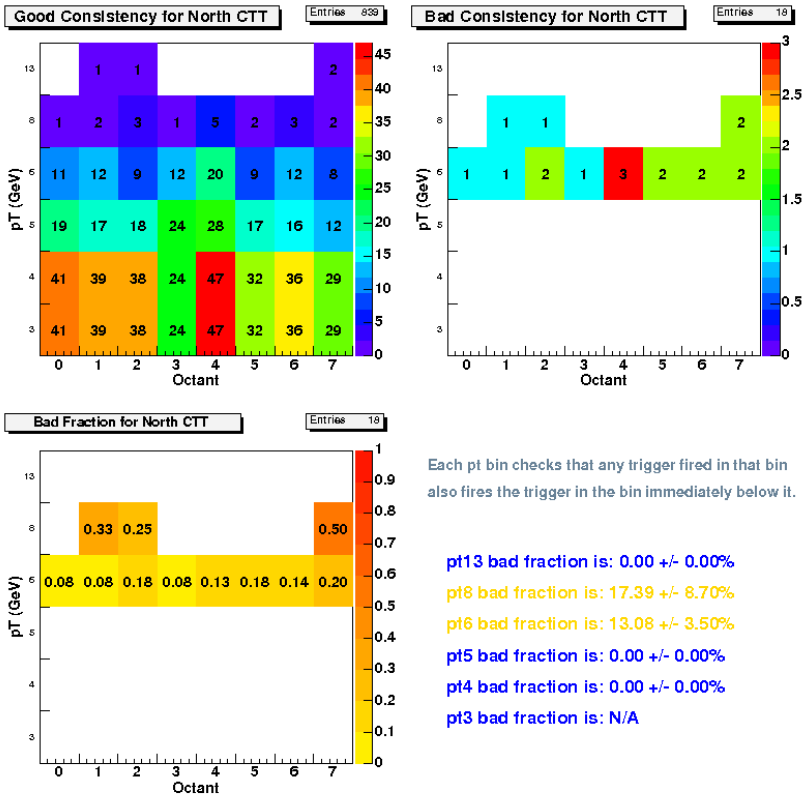

FIGURE C.11. Results of consistency check with bad Level 1 Muon firmware.

- **Pages 36-38** These three pages show hardware-simulator differences in the mu1ptxalxx, mu1ptxatxx, and mu1ptxaxlx triggers, respectively, as a function of region and octant (Figure C.12). These plots allow experts to quickly pinpoint the location of a failing trigger card. A common source of failure occurs when a trigger board daughter card lifts from its connecting pins, causing hardware triggers to fail to fire.

  The mu1ptxalxx hardware trigger is the simplest to simulate, as it fires on a single layer (generally A-layer) scintillator hit. This is thus the most well-understood of the simulated triggers. Any excess of simulated over hardware triggers in this channel is cause for special concern, and generates a minor alert. The mu1ptxatxx and mu1ptxaxlx require more sophisticated trigger conditions, and are known not to be perfectly simulated. Simulator excesses in these triggers do not create alerts, but are still plotted for the expert to view (see Figure C.13).

- **Rate Plotter** This tool makes plots of rate versus luminosity for all Level 1 Muon triggers, using luminosity recorded in the Beams Division Notification web page [71]. Rates are gathered once per hour via a daq_monitor instance created by the *start_AOTmon* tool in the */projects/l1muo/l1mu_AOTmon* directory. This update frequency is increased to once every ten minutes for luminosities greater than $100E30\ cm^{-2}s^{-1}$ in order to better understand trigger behavior at high luminosity. The *ratefiles* subdirectory stores all recorded ratelists.

  The *weekscript.sh* script in */projects/l1muo/ratecheck/newrate* generates plots of rate versus luminosity from the recorded ratelists. This script is run once per hour at 41 minutes past the hour, and its output is linked to the Level 1 muon home page. Sample plots for the *mu1ptxatxx*, *mu1ptxatlx*, and *mu1ptxattx* triggers are shown in Figure C.14.

  The generated plots are particularly useful for identifying runs in which a hot muon

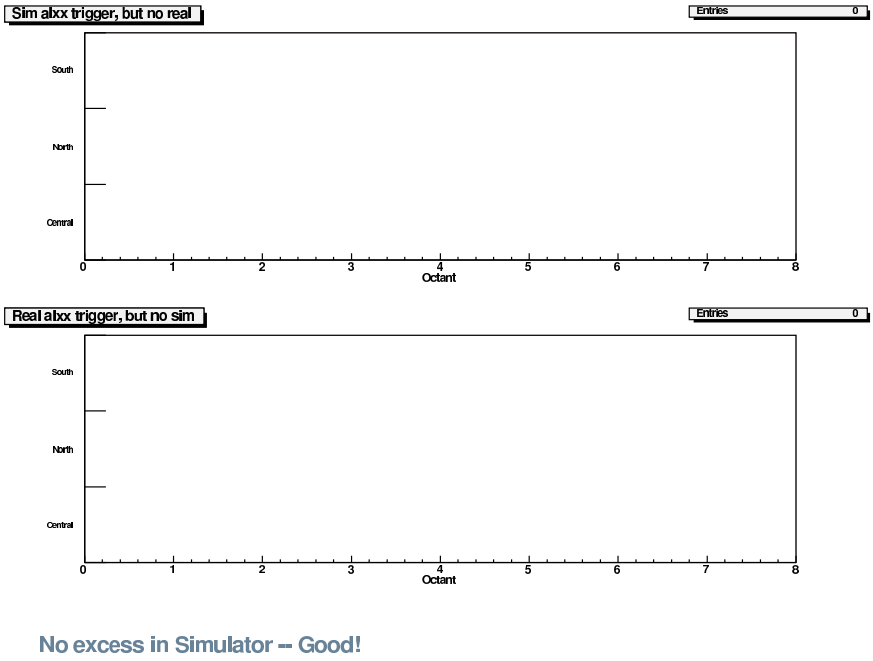

FIGURE C.12. Simulator and hardware excesses for the *mu1ptxalxx* trigger.

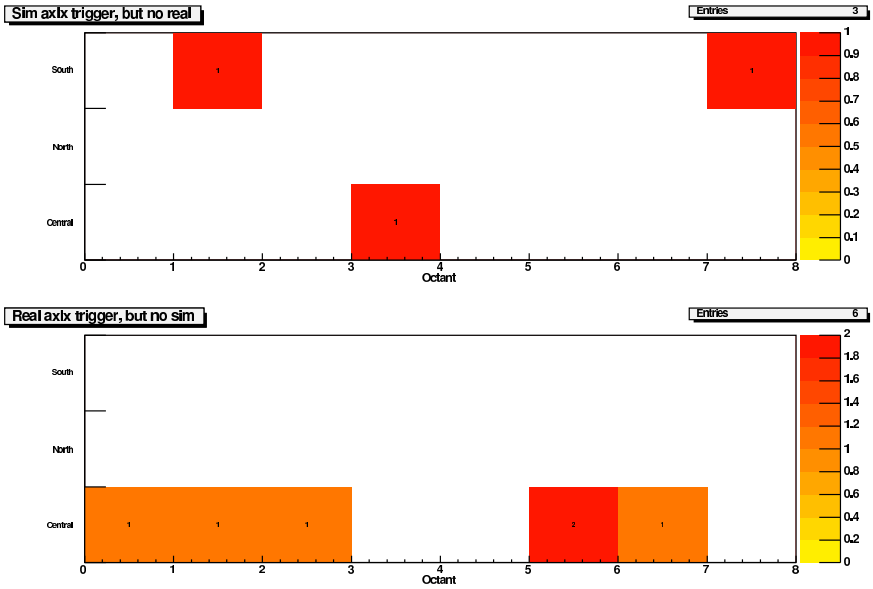

Excess in Simulator -- Could indicate loose flavor board!

FIGURE C.13. Simulator and hardware excesses for the *mu1ptxaxlx* trigger.

input results in a higher-than-expected trigger rate. Files with known bad rates due to trigger problems, incorrect luminosity reporting, or other issues may be excluded from the plots by adding their names to the file *badlist_cron.py* in the *newrate* directory.

- **Checklist Plotter** This tool plots the mu1ptxctxx and mu1ptxbtxx rates as recorded by the CalMuon shifter in the run checklist. Plots are updated every four hours, starting at 00:11, and are displayed on the l1muo web page. With the advent of the Rate Plotter described above, this tool has evolved from a check on the Level 1 Muon rates to a check on shifter awareness and alertness.

- **Power Supply Archiver** This tool records the currents, voltages, temperatures, and status bits of all Level 1 Muon supplies. It is updated daily, and its results are available on the Level 1 Muon web page. In the event of a power supply failure, this tool allows experts to precisely identify the cause and time of the failure. It is viewed by Level 1 Muon experts and by members of the DØ electrical support group.

- **Efficiency Monitor** Code for monitoring trigger efficiency resides on the clued0 computer cluster rather than online, in the directory */rooms/gila6/jtemple/analysis_example*. Efficiencies are updated weekly, with clued0 scripts at *jtemple/cronjobs*. These scripts search for data reconstructed during the previous week.

  Unbiased muons are selected from this data by choosing events in which either an electron or jet trigger fired. Trigger efficiencies for Run IIb triggers are measured by plotting the fraction of tight muons with a Level 1 muon trigger in the same octant as the muon. This fraction is plotted versus p_T. Because muon trigger roads were optimized on 4-GeV muons, the average trigger efficiency is found by fitting a straight line to the efficiency distribution above 4 GeV. Binomial errors are used on the efficiency points, to prohibit the unphysical condition of efficiencies greater than unity.

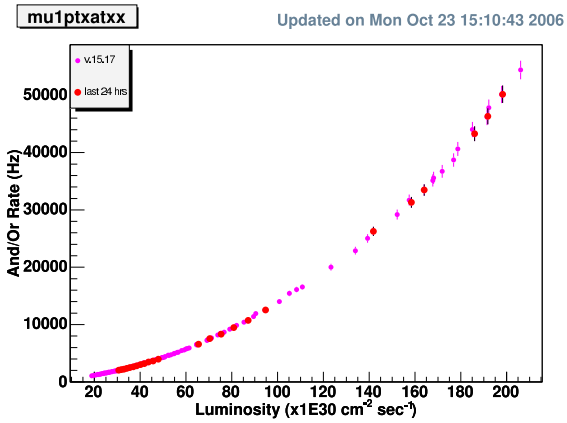

(a) mu1ptxatxx

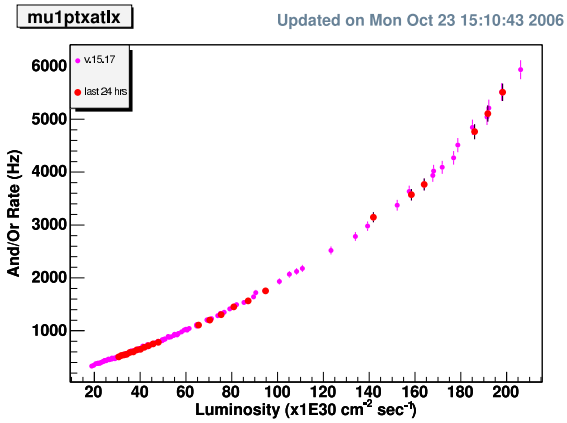

(b) mu1ptxatlx

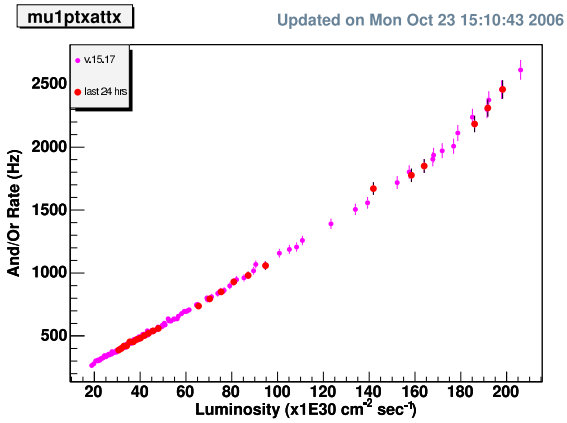

(c) mu1ptxattx

FIGURE C.14. Plots of trigger rates versus luminosity for the *mu1ptxatxx*, *mu1ptxatlx*, and *mu1ptxattx* Level 1 Muon triggers.

This method for estimating efficiency differs slightly from what was done in Run IIa. During that time, an explicit 4 GeV cut was placed on reconstructed muons. The muon detector hit requirements on reconstructed muons were adjusted so that the selected muon quality was somewhere between medium and tight. Efficiencies were measured simply by calculating the overall fraction of events in which a particular trigger fired. Binomial error bars were not employed, so the uncertainties on the efficiency could have non-physical values. Figure C.15 illustrates the difference between Run IIa and Run IIb calculations of the mu1ptxatxx trigger efficiency. For either method of calculation, the mu1ptxatxx trigger is found to be $> 95\%$ efficient on tight muons with p_T larger than 4 GeV.

Efficiency distributions are also generated as functions of η and ϕ. Dips in efficiencies on these plots can indicate hardware or firmware problems on individual trigger cards. Figure C.16 shows an efficiency dip near $\phi = 0$, caused by a failing trigger card in central octant 0. A second dip occurs near $\phi = 4.5$, where incomplete muon counter coverage limits the effectiveness of the tight scintillator trigger. This second dip is expected to be present, and does not necessarily indicate a problem with the Level 1 Muon trigger.

Efficiencies are monitored on a weekly basis, and are plotted at :
`http://www-clued0.fnal.gov/~jtemple/effic.html`.
These plots show the evolution of the *mu1ptxatxx*, *mu1ptxatlx*, and *mu1ptxattx* triggers over time, as in Figure C.17. Breaks in the distribution indicate changes in versions of the reconstruction code and long-term interruptions of data-taking. In this particular figure, large uncertainties appear at the start of Run IIb as the efficiency code was revised and optimized.

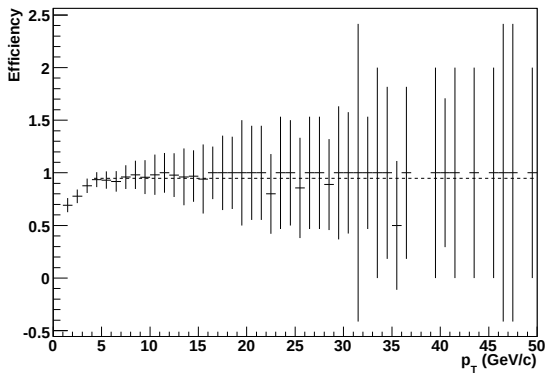

(a) Run IIa

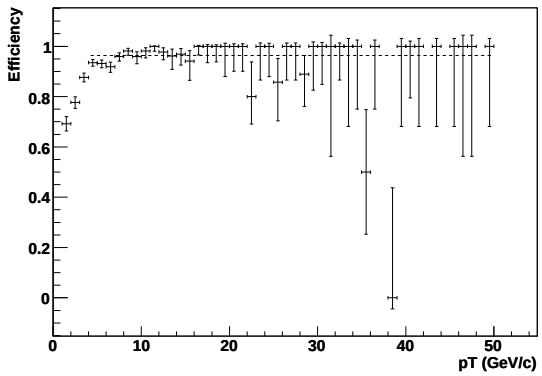

(b) Run IIb

FIGURE C.15. *mu1ptxatxx* efficiency calculations using (a) Run IIa and (b) Run IIb algorithms.

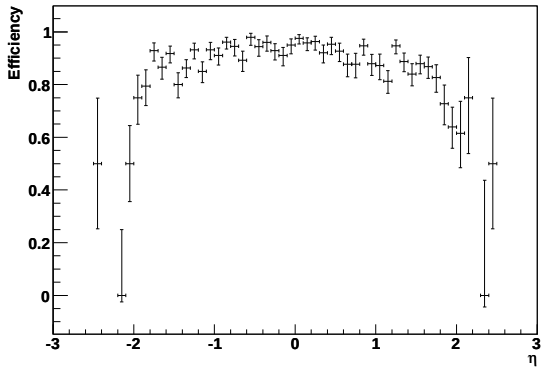

(a)

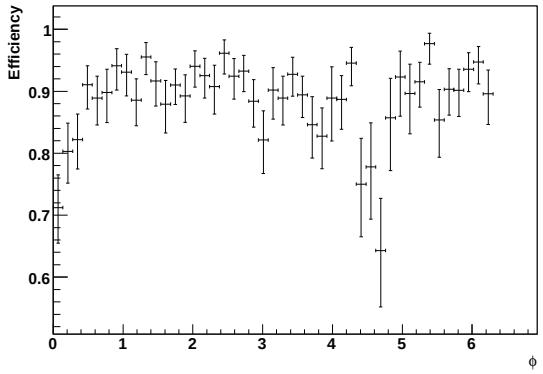

(b)

FIGURE C.16. mu1ptxatxx efficiency (a) versus η and (b) versus ϕ.

C.2.3 Diagnostic/Control Tools

A number of programs have been developed to supplement the automated and shifter-oriented tools outlined above. These allow experts to easily identify and disable problematic inputs and to quickly change MTM trigger terms for the purposes of special runs or trigger commissioning.

The Level 1 Muon Register Monitor GUI is perhaps the most useful of all Level 1 monitoring tools. It is contained in the same */projects/l1muo/REGmonitor/CrateMonitor* code as the Power Supply Monitor GUI described in section C.2.1. The Register Monitor checks all inputs to the central, north, and south trigger crates (labeled “MTCC”, “MTCN”, and “MTCS”, respectively) as well as the MTM trigger crate. It displays the contents of numerous status registers for each trigger card. The displays are color-coded: green for a normal state, yellow for a state of concern, and red for a problematic state (see Figure C.18).

The Register Monitor monitors Mask, Lock, Parity, FIFO-Full (FF Full), and Latched Error registers on each octant-level trigger card. A problem with any of these registers points to a problem in the Level 1 Muon system. The purpose of each of these registers is described below:

- **Mask** – This shows which inputs are enabled to the Level 1 Muon system. In normal running, all available inputs should be enabled. Occasionally, problems with front ends require that they are disabled at Level 1 Muon. Any such disabled inputs reduced the efficiency of the Level 1 Muon triggers.

- **Lock** – This indicates that the input front end is connected to the Level 1 Muon system. Bad lock usually indicates that a cable is unplugged or that a front end has lost power.

- **FF Full** – This indicates that a FIFO from at least one front end input is completely

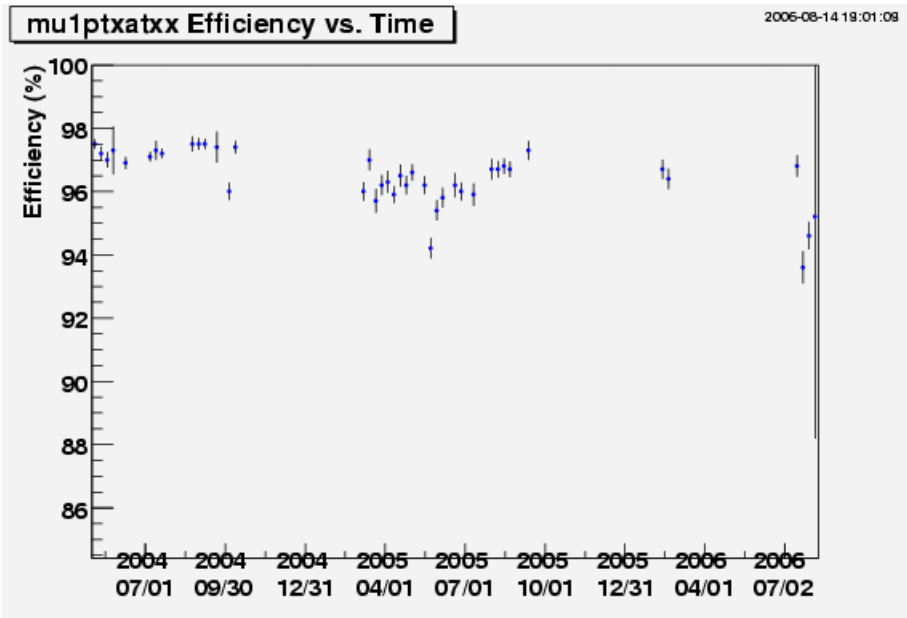

FIGURE C.17. Efficiency versus time for the mu1ptxatxx trigger.

FIGURE C.18. Status of all register monitors in the MTCS crate. The green color indicates that all registers are reading back their normal values.

full, and unable to accept more data. Generally, this occurs when one input stops sending data. The Level 1 Muon trigger cards do not process an event until all their unmasked input FIFOs contain data. If one input fails to send data, the remaining input FIFOs will fill up as they wait to begin processing.

- **Parity** – Parity serves as a comparison of the data sent by a front end with the data received by Level 1 Muon. Bad parity generally indicates that a cable is poorly terminated. Bad parity values can also occur when the input front ends are not in their normal running state.

- **Latch Error** – This register stores latched versions of the Lock and FF Full registers. It also contains a latched "FIFO Empty" status bit, which is raised if an input FIFO goes empty before all of its expected data is read by Level 1 Muon. This may indicate a problem with an input cable or with the data being sent by a front end.

  Whenever an sclinit is issued, lock is momentarily lost as front ends are reset. The MTC10 cards also raise FF Full during an sclinit. This is an expected response to the sclinit signal, and does not indicate a problem with Level 1 Muon.

If a problem input is found, that input must be disabled to Level 1 Muon. This may be done by directly writing to the mask register of the appropriate trigger card, or through the use of the *l1muo_inputs.py* GUI. This GUI is located in */projects/l1muo/vme_gui*, and provides simple "point-and-click" functionality for enabling and disabling inputs. The full use of this GUI is described in [72]; a sample page showing the interface for disabling a CTT input is shown in Figure C.19. This allows the Level 1 Muon inputs to remotely direct the enabling and disabling of inputs by CalMuon shifters.

The MTM trigger logic forms 256 muon-based triggers. Only 32 of these triggers are read out by the trigger framework at any one time. Exactly which triggers are read out may be determined by running the *l1muo_inputs.py* GUI in expert mode (by attaching a -x suffix to the command line when starting the GUI). The triggers may also be set by using

FIGURE C.19. GUI used to enable/disable CTT inputs to Level 1 Muon.

the *ComicsNotebook.py* GUI in */projects/l1muo/vme_gui*. Figure C.20 shows the main page of this GUI. Triggers may be set according to their trigger number (0-255). A separate GUI page provides mapping between trigger numbers and their more commonly-used trigger names, as in Figure C.21. This GUI allows each MTM trigger to be set individually, so that one trigger term can be changed without affecting data taking. When this is done, care must be taken to ensure that the changed trigger is not part of the trigger list in use by the run!

C.3 Data Quality

The programs described above combine to provide robust monitoring of the Level 1 Muon system. They allow for quick diagnoses of any problems within the system. Discovered problems are reported to the DØ Data Quality Coordinators. Runs in which Level 1 Muon is determined to be malfunctioning are removed from consideration for muon-based physics analyses.

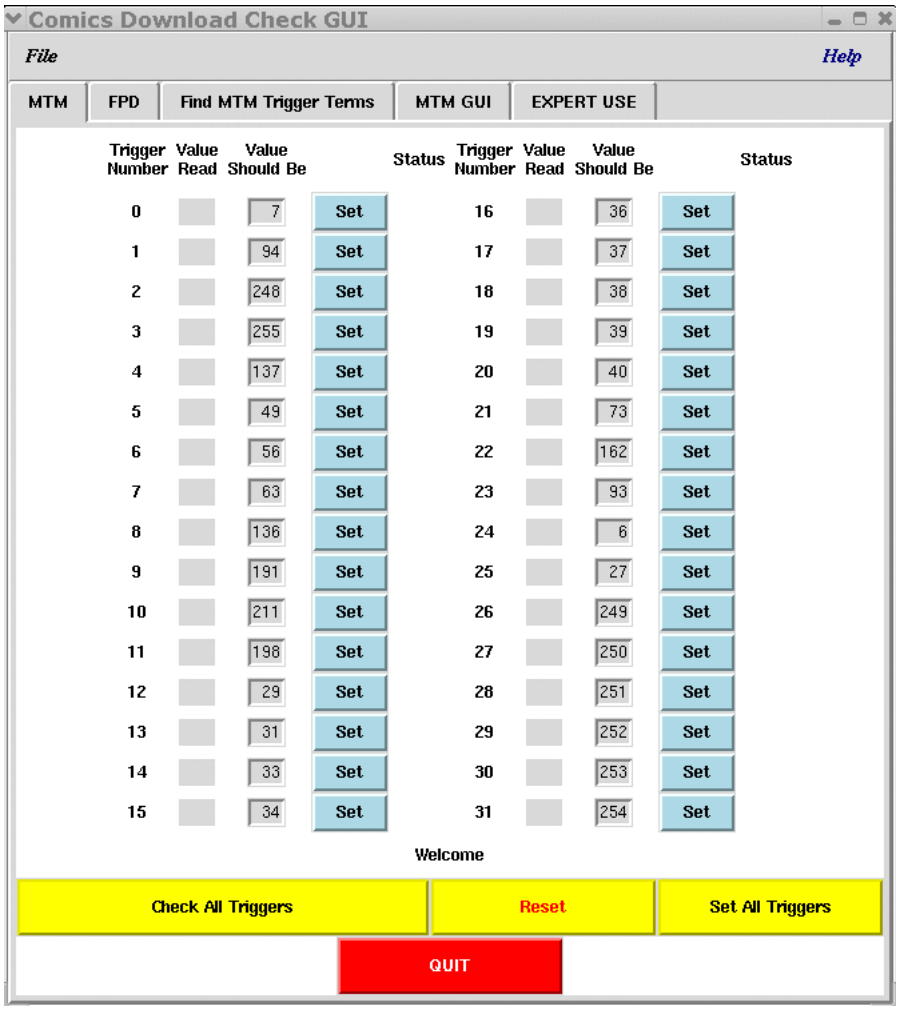

FIGURE C.20. GUI used to set Level 1 Muon MTM triggers.

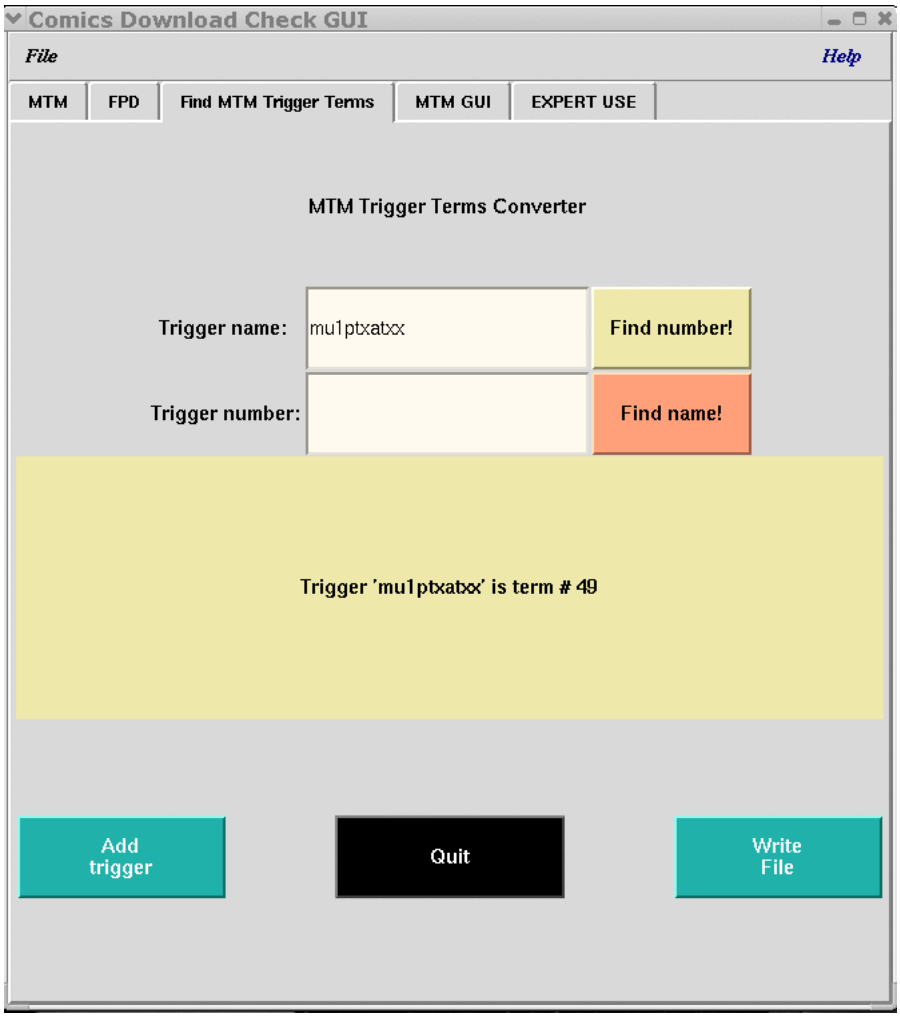

FIGURE C.21. Map between trigger names and MTM trigger numbers.

REFERENCES

[1] M. Banner *et al.* [UA2 Collaboration], Phys. Lett. B **122**, 476 (1983).

[2] G. Arnison *et al.* [UA1 Collaboration], Phys. Lett. B **126**, 398 (1983).

[3] K. Kodama *et al.* [DONUT Collaboration], Phys. Lett. B **504**, 218 (2001).

[4] F. Abe *et al.* [CDF Collaboration], Phys. Rev. Lett. **74**, 2626 (1995).

[5] S. Abachi *et al.* [D0 Collaboration], Phys. Rev. Lett. **74**, 2632 (1995).

[6] G. 't Hooft and M. J. G. Veltman, Nucl. Phys. B **44**, 189 (1972).

[7] D.J. Gross and F. Wilczek, Phys. Rev. Letters **30** 1343 (1793); H.D. Politzer, Phys. Rev. Letters **30** 1346 (1973).

[8] P. E. L. Rakow, Nucl. Phys. Proc. Suppl. **140**, 34 (2005).

[9] S. Eidelman *et al.* [Particle Data Group], Phys. Lett. B **592**, 1 (2004).

[10] V. M. Abazov *et al.* [CDF Collaboration], Phys. Rev. D **70**, 092008 (2004).

[11] Numerous Higgs searches are underway, both at the Tevatron CDF and DØ experiments and at the LEP e^+e- collider. A summary of these searches is given in <http://pdg.lbl.gov/2006/listings/s055.pdf>.

[12] N. Kidonakis and R. Vogt, Int. J. Mod. Phys. A **20**, 3171 (2005).

[13] D. Acosta *et al.* [CDF Collaboration], Phys. Rev. Lett. **95**, 102002 (2005).

[14] R. Godang [BaBar Collaboration], AIP Conf. Proc. **842**, 720 (2006).

[15] M. Beneke *et al.*, Proc. Workshop on Standard Model Physics (and more) at the LHC, LHC, CERN-2000-004".

[16] N. Isgur and M. B. Wise, Phys. Lett. B **232**, 113 (1989).

[17] B. Evanger and B.Worthel, Fermilab Beams Division Internal Note **1023**, (2004).

[18] V. M. Abazov *et al.* [D0 Collaboration], Nucl. Instrum. Meth. A **565**, 463 (2006).

[19] D. McGinnis, Fermilab Beams Division Internal Note **1941** (2005).

[20] S. Abachi, *et al.*, Nucl. Instrum. Methods Phys. Rev. A **338**, 185 (1994).

[21] Jackson, J.D., *Classical Electrodynamics* (John Wiley and Sons, New York, 1999).

[22] V. M. Abazov *et al.* [DØ Collaboration], Nucl. Instrum. Meth. A **552**, 372 (2005).

[23] J. T. Linnemann, Int. J. Mod. Phys. A **16S1C**, 1166 (2001).

[24] R. D. Angstadt *et al.*, IEEE Trans. Nucl. Sci. **51**, 445 (2004).

[25] T. Edwards *et al.*, DØ Note 4496 (2004).

[26] M. L. Mangano, M. Moretti, F. Piccinini, R. Pittau and A. D. Polosa, JHEP **0307**, 001 (2003).

[27] H. L. Lai *et al.*, Phys. Rev. D **51**, 4763 (1995).

[28] T. Sjostrand, L. Lonnblad and S. Mrenna, "PYTHIA 6.2: Physics and manual," arXiv:hep-ph/0108264 (2001).

[29] Y. Fiskay and J. Womersley, DØ Note 3191 (1997).

[30] R. Brun *et al.*, "GEANT, Detector Description and Simulation Tool, V. 3.21," CERN Program Library, 1994 (unpublished).

[31] S. Eno and M. Verzocchi, DØ Note 4097 (2003).

[32] *D0Sim.* Fermi National Accelerator Laboratory. 27 October 2006 <http://www-d0.fnal.gov/computing/MonteCarlo/simulation/d0sim.html>.

[33] *Run II Reconstruction Program Status - Version p14.* Fermi National Accelerator Laboratory. 27 October 2006 <http://www-d0.fnal.gov/computing/algorithms/status/p14.html>.

[34] P. V. C. Hough, International Conference on High Energy Accelerators and Instrumentation, CERN, 554 (1959).

[35] H. Greenlee, DØ Note 4303 (2004).

[36] G. Hesketh, DØ Note 4079 (2003).

[37] A. Garcia-Bellido *et al.*, DØ Note 4320 (2004).

[38] L. Duflot, DØ Note 3749 (2000).

[39] E. Busato and B. Andrieu, DØ Note 4457 (2004).

[40] *DZero Preliminary Jet Energy Scale.* Fermi National Accelerator Laboratory. 31 October 2006 <http://www-d0.fnal.gov/phys_id/jes/public/plots_v7.1>.

[41] J. Kozminski *et al.*, DØ Note 4449 (2004).

[42] Top Physics Working Group, DØ Note 4419 (2004).

[43] C. Clément *et al.*, DØ Note 4350 (2004).

[44] J. Zhu, DØ Note 4323 (2004).

[45] C. Clément *et al.*, DØ Note 4662 (2004).

[46] F. Fielder, A. Magerkurth, and P. Schieferdecker, DØ Note 4717 (2005).

[47] M. Klute, L. Phaf, and D. Whiteson, DØ Note 4122 (2003).

[48] Rene Brun and Fons Rademakers, Proceedings AIHENP'96 Workshop, Lausanne, Sep. 1996, Nucl. Inst. & Meth. in Phys. Res. A 389 (1997) 81-86. See also <http://root.cern.ch/>.

[49] M. Besançon, F. Déliot, and V. Sharyy, DØ Note 4877 (2005).

[50] S. Anderson *et. al.*, DØNote 4827 (2005).

[51] M. Agelou *et al.*, DØNote 4512 (2004).

[52] *New Page 1*. Fermi National Accelerator Laboratory. 27 October 2006 <http://www-d0.fnal.gov/D0Code/source/top_dq/doc/usage.htm>.

[53] R. Hall, J. D. Hobbs, and H. Zhu, DØ Note 2591 (1996).

[54] B. Abbott *et al.* [DØ Collaboration], Phys. Rev. D **60**, 052001 (1999).

[55] J. Kozminski, Ph.D. thesis, Michigan State University, 2005.

[56] W.-M. Yao et al., J. Phys. G **33**, 32:1 (2006).

[57] James, F., Program Library **D506**. CERN, 1994.

[58] L. Holmström, S. Sain, H. Miettinen, Comp. Phys. Comm. **88**, 195 (1995).

[59] M. Mulders and M. Weber, DØ Note 4705 (2005).

[60] A. D. Martin, R. G. Roberts, W. J. Stirling and R. S. Thorne, Eur. Phys. J. C **4**, 463 (1998).

[61] L. Christofek, DØ Note 4712 (2005).

[62] V. M. Abazov *et. al.* [DØ Collaboration], Phys. Rev. Lett. (submitted for publication).

[63] D. Boline and U. Heintz, DØ Note 5032 (2006).

[64] B. Kehoe *et. al.*, DØ Note 5010 (2006).

[65] J. Cammin, private communication.

[66] P. Renkel *et. al.*, DØ Note 5171 (2006).

[67] S. Anderson *et. al.*, DØ Note 4983 (2006).

[68] F. Beaudette and J. F. Grivaz, DØ Note 3976 (2002).

[69] *Significant Event System.* Fermi National Accelerator Laboratory. 27 October 2006 <http://d0server1.fnal.gov/users/savage/www/ses/ses.html>.

[70] *daqAI.* University of Washington. 27 October 2006 <http://d0.epe.phys.washington.edu/Projects/daqAI>.

[71] *Accelerator Division Notification.* Fermi National Accelerator Laboratory. 27 October 2006 <http://www-bd.fnal.gov/notifyservlet>.

[72] *Masking off inputs to L1 Muon.* Fermi National Accelerator Laboratory. 27 October 2006 <http://d0server1.fnal.gov/projects/L1_Muon/Documentation/html/L1Muon_input_doc2.htm>.